AB

A measurement of the τ lifetime using the DELPHI silicon microstrip vertex detector

Thesis submitted in accordance with the requirements
of the University of Liverpool
for the degree of Doctor in Philosophy by
Anthony Robert Campion

Oliver Lodge Laboratory
University of Liverpool

August 1991

Abstract

An analysis of data from the DELPHI detector on the LEP collider at CERN has resulted in a new measurement of the τ lifetime. $\tau^+\tau^-$ pairs were produced from the decay of on-shell Z^0 particles at rest in the laboratory frame ($\sqrt{s} \approx 91$GeV), and the impact parameter method was used to determine the mean lifetime of a sample of τ particles decaying to give one charged track and neutrals. The measured lifetime was 321±36±18fs, (STAT) (SYS) and is consistent with previously measured values of the lifetime.

The measurement made extensive use of the DELPHI silicon microstrip vertex detector, the first solid state tracking detector of its kind to be installed around a colliding beam. The detector is described and discussed in detail, and a simulation program used in the lifetime analysis is presented.

Acknowledgements

During my time as a research student I have been lucky enough to know and work with a great many people working on the DELPHI experiment. I now take this opportunity of thanking all those who have helped me at various stages over the last three years. There are some people without whose influence this thesis would have taken a very different line. In particular I would like to mention the following ...

Firstly, I thank Mike Tyndel and Hans Dijkstra, whose enthusiasm and encouragement kept me going at a time when it would have been easy to leave the work of this thesis unfinished.

Thanks to Duncan Reid, and to Barry King, for sharing common problems of programming and of politics, and for much helpful advice throughout my time with the Liverpool group. Thanks to Duncan for many(!) words of wisdom on the analysis of Chapter 6, and for having the patience to proof read vast chunks of this thesis.

Thanks to Simon Gawne, Paul Maley and Pete Sanders, and to Jim Bennett, for friendship and occasional flashes of inspiration. Similarly, thanks to Mark Dinsdale for his part in getting the KWIKSIM program running.

Thanks to Paul Booth for leadership from the front, and for creating a uniquely stimulating working environment. Thanks to Neil Jackson for helpful discussions concerning the methods of maximum likelihood fitting.

Thanks to David Edwards for reading this entire thesis more than once during its preparation, and for his constructive comments and encouragement.

Finally, thanks to Mum, Dad, J&S for 24 years of support, to Sonja for keeping me sane, and to the people of the City of Bristol for light relief and pocket money.

The author's contribution

I joined the DELPHI project in October 1988, about six months before the detector was due to be installed and instrumented around the LEP beampipe in its experimental hall. I spent my first year as a member of the outer detector group, and moved to Geneva to take installation and cabling shifts in the DELPHI pit. No work from my first year is documented here.

At the start of my second year, I transferred to the microvertex group, and began the experimental work described in Chapter 4 of this thesis. It was at this time that I learnt about the design of the microvertex detector, documented here as Chapter 3. The apparatus used was already set up when I joined the group : I ran tests on the detector modules, transferred data to the IBM and wrote an analysis program to collate information and diagnose detector faults where possible. The program wrote out a calibration file for use with track reconstruction software, detailing regions of the detector modules within DELPHI functioning abnormally.

Towards the end of my second year I began to look at data from DELPHI, studying the principles of $\tau^+\tau^-$ event selection, with a mind to a τ lifetime measurement. I soon became more interested in the latter aspect of the work, and the event selection of Chapter 5 was carried out by Duncan Reid and Martin McCubbin.

Subsequently, I have written the software for the τ lifetime measurement by the impact parameter method, and have carried out the measurement from start to finish. I organised the writing of, and was the main author of, the microvertex simulation program used in the analysis. The work of Chapter 6 is my own, and has now been submitted for publication by the DELPHI collaboration[1].

Contents

Chapter 1. Introduction

Over the last 20 years, theoretical and experimental high energy physicists have become confident in their respective abilities to predict and to observe certain fundamental phenomena. These phenomena concern the behaviour of matter at its most basic level, the interactions of the smallest building blocks of substance we envisage. In all branches of physics, a subject is deemed to be understood when a mathematical model of an experiment predicts results which agree with observed effects in nature. In high energy physics, the so called standard model[2-4] represents our best understanding of elementary interactions; it bears up well under current experimental tests of the theory.

This thesis describes the experimental measurement of a physical observable. The observable is related, in the theory, to the mean time a particular particle (the τ lepton) lives before decaying. In measuring the τ lifetime we are testing the standard mathematical understanding of the phenomenon. The experimental result will have implications on current theoretical interpretation of high energy particle physics.

In this first Chapter of the thesis, the elementary ideas of particle physics are introduced, and the motivation behind a τ lifetime measurement is explained in the context of the standard model. The environment in which a lifetime measurement can be made is then discussed, and experimental techniques used in making the measurement are introduced. Subsequent Chapters describe the equipment used in collecting data, and the criteria on which the selection of a suitable data sample is based. A detailed analysis of the data finally results in a successful measurement of the lifetime of the τ lepton.

	Leptons	Quarks	
	seen individually	postulated as doublets	seen in groups
Three generations	$\begin{pmatrix}\nu_e\\ e\end{pmatrix}$	$\begin{pmatrix}u\\ d\end{pmatrix}$	Mesons $q\bar{q}$ (where q=u,d,c,s,b)
	$\begin{pmatrix}\nu_\mu\\ \mu\end{pmatrix}$	$\begin{pmatrix}c\\ s\end{pmatrix}$	
	$\begin{pmatrix}\nu_\tau\\ \tau\end{pmatrix}$	$\begin{pmatrix}t\\ b\end{pmatrix}$	Baryons qqq (various combinations)

Fig 1.1; Elementary particles.

Interaction	Mediator	Particles influenced	Relative strength at 10^{-19}m
Electromagnetic	γ (photon)	charged particles	10^{-2}
Weak	$W^{\pm}, Z^0$	all particles	10^{-5}
Strong	g (gluon)	quarks	1
Gravitational	graviton	all particles	10^{-39}

Fig 1.2; Fundamental interactions.

1.1 Motivation for a τ lifetime measurement

Elementary particles are believed to divide by nature into two mutually exclusive groups, quarks and leptons (Fig 1.1). The interactions between the particles can be understood in terms of four distinct classes (Fig 1.2). The standard model unifies the traditional weak and electromagnetic interactions of Fig 1.2 in terms of a single theory of electroweak interactions. It is (electro)weak theory which describes the physics of lepton decay, and which will be important here.

In the framework of the standard model, both the τ and μ leptons can decay via a weak process to give an electron, a neutrino and an antineutrino (Fig 1.3). The coupling between the (ν_τ, τ) current and the W, related to the probability per unit time of the process $\tau \rightarrow W\nu_\tau$ occurring, is conventionally denoted g_τ. Similarly, the couplings between the (ν_μ, μ) and (ν_e, e) currents and the W are

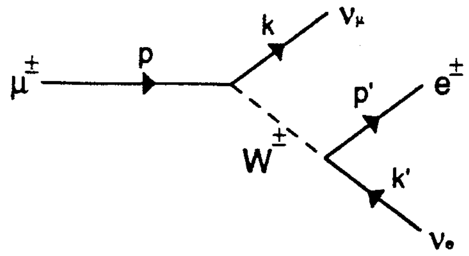

Fig 1.3; Tree level Feynman diagrams for 1.3a (above) μ decay, and for **1.3b (below)** τ decay to $e\nu\bar{\nu}$.

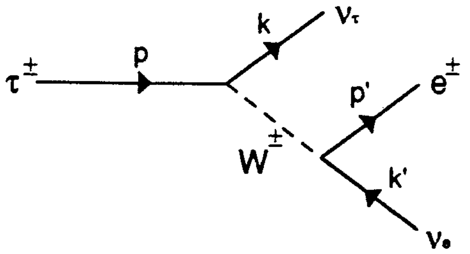

denoted g_μ and g_e respectively. Current theoretical and experimental understanding of weak interactions is that $g_\tau=g_\mu=g_e$: this is the principle of lepton universality.

The only decay mode open to the μ is that depicted by Fig 1.3a. The probability per unit time of μ decay is therefore calculable, and an expression for g_μ in terms of the μ lifetime T_μ and mass M_μ can be derived.

By contrast, many decay modes are open to the τ (Fig 1.4). Some of these involve hadronisation, and there is no analytic expression to relate the τ lifetime T_τ to the couplings of the various processes involved. However, if the fraction of τ decays which result in the final state of Fig 1.3b (the branching ratio B_e) is known, then g_τ can be calculated from B_e and T_τ. Experimental values for

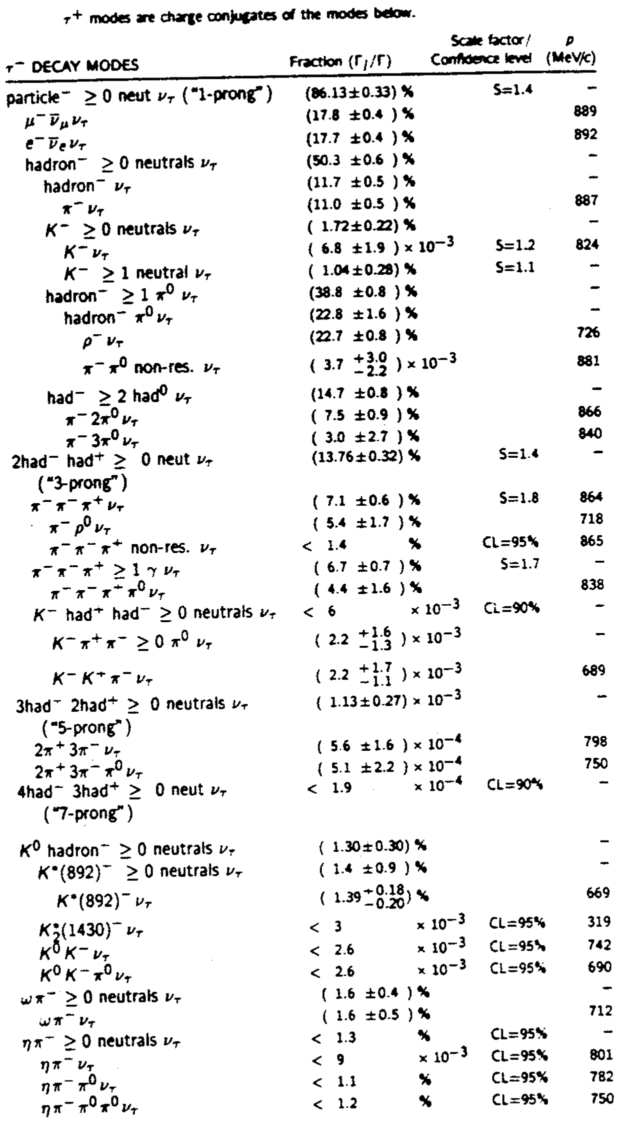

τ^+ modes are charge conjugates of the modes below.

τ^- DECAY MODES	Fraction (Γ_i/Γ)	Scale factor/ Confidence level	p (MeV/c)
particle$^-$ ≥ 0 neut ν_τ ("1-prong")	(86.13 ± 0.33) %	S=1.4	–
$\mu^- \bar{\nu}_\mu \nu_\tau$	(17.8 ± 0.4) %		889
$e^- \bar{\nu}_e \nu_\tau$	(17.7 ± 0.4) %		892
hadron$^-$ ≥ 0 neutrals ν_τ	(50.3 ± 0.6) %		–
hadron$^-$ ν_τ	(11.7 ± 0.5) %		–
$\pi^- \nu_\tau$	(11.0 ± 0.5) %		887
K^- ≥ 0 neutrals ν_τ	(1.72 ± 0.22) %		–
$K^- \nu_\tau$	$(6.8 \pm 1.9) \times 10^{-3}$	S=1.2	824
K^- ≥ 1 neutral ν_τ	(1.04 ± 0.28) %	S=1.1	–
hadron$^-$ $\geq 1\ \pi^0\ \nu_\tau$	(38.8 ± 0.8) %		–
hadron$^-$ $\pi^0 \nu_\tau$	(22.8 ± 1.6) %		–
$\rho^- \nu_\tau$	(22.7 ± 0.8) %		726
$\pi^- \pi^0$ non-res. ν_τ	$(3.7\ ^{+3.0}_{-2.2}) \times 10^{-3}$		881
had$^-$ ≥ 2 had^0 ν_τ	(14.7 ± 0.8) %		–
$\pi^- 2\pi^0 \nu_\tau$	(7.5 ± 0.9) %		866
$\pi^- 3\pi^0 \nu_\tau$	(3.0 ± 2.7) %		840
2had$^-$ had$^+$ $\geq$ 0 neut ν_τ ("3-prong")	(13.76 ± 0.32) %	S=1.4	–
$\pi^- \pi^- \pi^+ \nu_\tau$	(7.1 ± 0.6) %	S=1.8	864
$\pi^- \rho^0 \nu_\tau$	(5.4 ± 1.7) %		718
$\pi^- \pi^- \pi^+$ non-res. ν_τ	< 1.4 %	CL=95%	865
$\pi^- \pi^- \pi^+ \geq 1\ \gamma\ \nu_\tau$	(6.7 ± 0.7) %	S=1.7	–
$\pi^- \pi^- \pi^+ \pi^0 \nu_\tau$	(4.4 ± 1.6) %		838
K^- had$^+$ had$^-$ ≥ 0 neutrals ν_τ	$< 6 \times 10^{-3}$	CL=90%	–
$K^- \pi^+ \pi^- \geq 0\ \pi^0\ \nu_\tau$	$(2.2\ ^{+1.6}_{-1.3}) \times 10^{-3}$		–
$K^- K^+ \pi^- \nu_\tau$	$(2.2\ ^{+1.7}_{-1.1}) \times 10^{-3}$		689
3had$^-$ 2had$^+$ $\geq$ 0 neutrals ν_τ ("5-prong")	$(1.13 \pm 0.27) \times 10^{-3}$		–
$2\pi^+ 3\pi^- \nu_\tau$	$(5.6 \pm 1.6) \times 10^{-4}$		798
$2\pi^+ 3\pi^- \pi^0 \nu_\tau$	$(5.1 \pm 2.2) \times 10^{-4}$		750
4had$^-$ 3had$^+$ $\geq$ 0 neut ν_τ ("7-prong")	$< 1.9 \times 10^{-4}$	CL=90%	–
K^0 hadron$^-$ ≥ 0 neutrals ν_τ	(1.30 ± 0.30) %		–
$K^*(892)^-$ ≥ 0 neutrals ν_τ	(1.4 ± 0.9) %		–
$K^*(892)^- \nu_\tau$	$(1.39\ ^{+0.18}_{-0.20})$ %		669
$K_2^*(1430)^- \nu_\tau$	$< 3 \times 10^{-3}$	CL=95%	319
$K^0 K^- \nu_\tau$	$< 2.6 \times 10^{-3}$	CL=95%	742
$K^0 K^- \pi^0 \nu_\tau$	$< 2.6 \times 10^{-3}$	CL=95%	690
$\omega \pi^- \geq 0$ neutrals ν_τ	(1.6 ± 0.4) %		–
$\omega \pi^- \nu_\tau$	(1.6 ± 0.5) %		712
$\eta \pi^- \geq 0$ neutrals ν_τ	< 1.3 %	CL=95%	–
$\eta \pi^- \nu_\tau$	$< 9 \times 10^{-3}$	CL=95%	801
$\eta \pi^- \pi^0 \nu_\tau$	< 1.1 %	CL=95%	782
$\eta \pi^- \pi^0 \pi^0 \nu_\tau$	< 1.2 %	CL=95%	750

Fig 1.4a; Decay modes of the τ lepton.

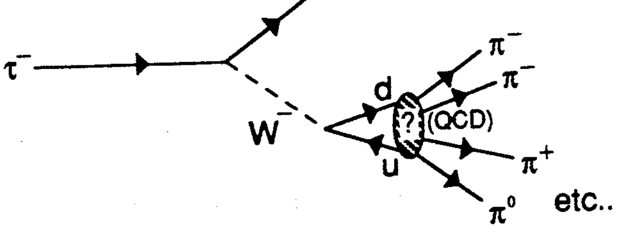

Fig 1.4b. Some τ decays involve QCD hadronisation processes, and are not calculable.

T_τ, T_μ, B_e and the lepton masses allow a comparison of g_μ and g_τ, and consequently provide a test of lepton universality.

There now follows an outline of the calculation for g_μ in terms of T_μ. Because of the similarity of the Feynman diagrams shown in Fig 1.3, the calculation can also be applied to the case of τ decay, given at all times the following correspondences;

$$\begin{gathered} g_\mu \longleftrightarrow g_\tau \\ T_\mu \longleftrightarrow \frac{T_\tau}{B_e} \\ M_\mu \longleftrightarrow M_\tau \end{gathered} \tag{1.1}$$

where M_τ denotes the mass of the τ. Finally, in section 1.1.2, the derived results will be used to express the ratio g_μ/g_τ in terms of measurable quantities.

1.1.1 The physics of μ decay

The Feynman diagram for μ decay was shown in Fig 1.3. According to the Feynman rules for the calculation of invariant amplitudes A,

$$-iA = \bar{u}_{\nu_\mu}(k)\left[\frac{-ig_\mu}{2\sqrt{2}}\gamma_\zeta(1-\gamma^5)\right]u_\mu(p) \times \frac{i}{M_W^2 - q^2} \times \bar{u}_e(p')\left[\frac{-ig_e}{2\sqrt{2}}\gamma^\zeta(1-\gamma^5)\right]v_{\nu_e}(k') \tag{1.2}$$

where M_W is the mass of the W, q^2 is the 4-momentum carried by the W in the interaction, and k, p, k′ and p′ are the 4-momenta of the particles as defined in Fig 1.3. Kinematically, q^2 can vary from 0 to M_μ^2, and so it is always true that $q^2 \ll M_W^2$. Equation (1.2) then leads to;

$$|A|^2 = \left(\frac{g_\mu g_e}{8M_W^2}\right)^2 [\bar{u}_{\nu_\mu}(k)\gamma_\zeta(1-\gamma^5)u_\mu(p)][\bar{u}_\mu(p)(1+\gamma^5)\gamma_\xi u_{\nu_\mu}(k)] \times \\ [\bar{u}_e(p')\gamma^\zeta(1-\gamma^5)v_{\nu_e}(k')][\bar{v}_{\nu_e}(k')(1+\gamma^5)\gamma^\xi u_e(p')] \tag{1.3}$$

Trace theorems can be used to simplify equation (1.3), with the result that

$$\overline{|A|^2} = 2\left(\frac{g_\mu g_e}{M_W^2}\right)^2 (k \cdot p')(k' \cdot p) \tag{1.4}$$

where $\overline{|A|^2}$ has now been averaged over incoming and summed over outgoing particle spin states. The amplitude for μ decay is related by Fermi's golden rule to the elemental decay rate $d\Gamma$;

$$d\Gamma = \frac{1}{2p^0} \overline{|A|^2} dQ \tag{1.5}$$

where the invariant 3-body phase space element dQ is given by;

$$dQ = \frac{d^3p'}{(2\pi)^3 2p'^0} \frac{d^3k}{(2\pi)^3 2k^0} \frac{d^3k'}{(2\pi)^3 2k'^0} (2\pi)^4 \delta^{(4)}(p - p' - k - k') \tag{1.6}$$

On integration over d^3k, and expressed in the rest frame of the μ, equation (1.6) reduces to;

$$dQ = \frac{1}{(2\pi)^5} \frac{d^3p'}{2p'^0} \frac{d^3k'}{2k'^0} \delta(M_\mu^2 - 2M_\mu p'^0 - 2M_\mu k'^0 + 2p'^0 k'^0 (1 - \cos\psi)) \tag{1.7}$$

where ψ is the opening angle between the decay products e and $\bar{\nu}_e$, massless neutrinos have been assumed and the mass of the electron $M_e \approx 0.005 M_\mu$ has been neglected. Combining equations (1.4), (1.5) and (1.7), and using that in the rest frame;

$$(k \cdot p')(k' \cdot p) = \frac{1}{2}(M_\mu^2 - 2M_\mu k'^0) M_\mu k'^0 \tag{1.8}$$

the μ decay rate is given;

$$
\begin{aligned}
d\Gamma &= \frac{1}{2M_\mu} \times 2\left(\frac{g_\mu g_e}{M_W^2}\right)^2 \frac{1}{2}(M_\mu^2 - 2M_\mu k'^0)M_\mu k'^0 \times \\
&\qquad \frac{1}{(2\pi)^5}\frac{d^3p'}{2p'^0}\frac{d^3k'}{2k'^0}\,\delta(M_\mu^2 - 2M_\mu p'^0 - 2M_\mu k'^0 + 2p'^0k'^0(1-\cos\psi)) \qquad (1.9)\\
&= \frac{1}{64\pi^3}\left(\frac{g_\mu g_e}{M_W^2}\right)^2 p'^{0\,2}dp'^0\,k'^{0\,2}dk'^0\,d(\cos\psi)
\end{aligned}
$$

where in the second line, the phase space volume $d^3p'd^3k'$ has been replaced by $4\pi p'^{0\,2}dp'^0\;2\pi k'^{0\,2}dk'^0\;d(\cos\psi)$. The delta function places limits on energies p'^0 and k'^0, due to the fact that $\cos\psi$ is bounded by ±1, so that (1.9) can now be integrated to give the full μ decay rate Γ;

$$
\begin{aligned}
\Gamma &= \frac{M_\mu}{64\pi^3}\left(\frac{g_\mu g_e}{M_W^2}\right)^2 \int_0^{\frac{1}{2}M_\mu} dp'^0 \int_{\frac{1}{2}M_\mu - p'^0}^{\frac{1}{2}M_\mu} dk'^0\,k'^0(M_\mu - 2k'^0)\\
&= \frac{M_\mu^5}{6144\pi^3}\left(\frac{g_\mu g_e}{M_W^2}\right)^2
\end{aligned}
\qquad (1.10)
$$

(where the step of integrating over ψ has been skipped, and is demonstrated elsewhere[5]). Finally, using that;

$$
\Gamma \equiv \frac{1}{T_\mu} \qquad (1.11)
$$

and rearranging, the result is derived;

$$
T_\mu = \frac{6144\pi^3}{M_\mu^5}\left(\frac{M_W^2}{g_\mu g_e}\right)^2 \qquad (1.12)
$$

Fig 1.3 shows the lowest order, most important processes by which the μ and τ can decay to give $e\nu\bar{\nu}$. Fig 1.5 shows examples of higher order processes, where photon exchange (Fig 1.5a) and final state radiation (Fig 1.5b) modify the effective invariant amplitude for lepton decay. Correction

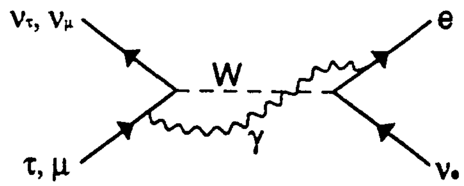

Fig 1.5; Higher level Feynman diagrams for μ and τ decay to $e\nu\bar{\nu}$ (c.f. Fig 1.3).

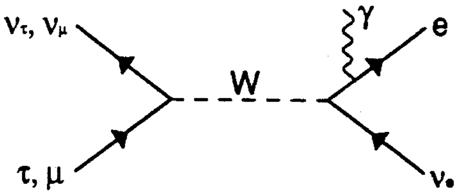

factors can be introduced into equation (1.12) to account for the consequent alteration in the predicted value for Γ. A more rigorous derivation[6] yields the result;

$$T_\mu = \frac{6144\pi^3}{M_\mu^5}\left(\frac{M_W^2}{g_\mu g_e}\right)^2 \frac{1}{F\left(\frac{M_e^2}{M_\mu^2}\right)\left[1+\frac{3M_\mu^2}{5M_W^2}\right]\left[1+\frac{\alpha(M_\mu^2)}{2\pi}\left(\frac{25}{4}-\pi^2\right)\right]} \tag{1.13}$$

where $F(x) = 1 - 8x + 8x^3 - x^4 - 12x^2\ln(x)$ modifies the phase space to allow the heaviest decaying lepton to have finite mass, the first term in square brackets allows non-zero q^2 in the propagator and the second for <u>Q</u>uantum <u>E</u>lectro<u>D</u>ynamical radiative effects, with $\alpha(M_\mu^2)$ defined as the running

QED coupling constant at the $q^2 = M_\mu^2$ scale. Weak radiative effects do not feature because of the mass of the mediating bosons.

The QED radiative correction factor affects the predicted value for T_μ by less than 0.5% : the same can be said of the value for T_τ resulting from equation (1.12) and the correspondences (1.1). Similarly, the approximations of zero mass for neutrinos and for the electron result in no more than a 0.3% limitation on precision (taking from ref [7] the 95% confidence level figure of $M_{\nu_\tau} < 35\,\mathrm{Mev}/c^2$ for the case of τ decay). Quadratically summed theoretical errors of 0.6% introduced by using (1.12) will not be significant compared to either statistical or systematic errors of measurement.

1.1.2 Testing the standard model

Equation (1.12) gave an expression for the μ lifetime T_μ in terms of the coupling constants g_μ and g_e. Using the correspondences (1.1), a similar expression for T_τ can be written;

$$\frac{T_\tau}{B_e} = \frac{6144\pi^3}{M_\tau^5}\left(\frac{M_W^2}{g_\tau g_e}\right)^2 \tag{1.14}$$

Dividing equations (1.12) and (1.14) gives the ratio between the coupling constants g_τ and g_μ;

$$\left(\frac{g_\tau}{g_\mu}\right)^2 = \left(\frac{M_\mu}{M_\tau}\right)^5 \frac{T_\mu}{T_\tau} B_e \tag{1.15}$$

The τ lifetime measurement of this thesis, together with world average values for M_τ, M_μ, T_μ and B_e, will give a value for the ratio between the weak coupling constants for the τ and μ leptons. In this way, lepton universality is tested directly by the experimental work which now follows.

1.2 Practicalities of a τ lifetime measurement

The very fact that the τ lepton has a finite (short) lifetime infers that it can not be observed in the natural environment around us. The τ data analysed in this lifetime measurement were taken at the DELPHI detector on the LEP particle accelerator ring at CERN, the European Organisation for Nuclear Research[1], in Geneva. LEP was operating at the Z^0 pole (Fig 1.6), and $\tau^+\tau^-$ pairs resulted from Z^0 decay. A description of the LEP machine now follows : section 1.2.2 then introduces possible methods for measuring the τ lifetime.

1.2.1 LEP

The Large Electron Positron collider[8] was purpose built at CERN to enable tests on the standard model to be conducted. As early as 1976, studies were being made to assess the feasibility of running a high energy e^+e^- machine to that end. Approved in 1981, LEP took over seven years to build, and first beam collisions were recorded in Autumn 1989.

LEP is in a circular tunnel ≈100m underground and 27km in ~~diameter~~ CIRCUMFERENCE. Four bunches of electrons and four bunches of positrons (anti-electrons) circulate in a beampipe under high vacuum. The beams of bunches can be made to collide at variable centre of mass energies close to 100GeV at the centres of eight 100m long straight sections in the beampipe, if required. Experimental detectors are situated at four of these 'intersection points' : DELPHI is at point 8 (Fig 1.7a).

The electrons and positrons accelerated in LEP originate in LEP Injector Linear accelerators on the main CERN site at Meyrin, and are stored in the Electron/Positron Accumulator (Fig 1.7b). Earlier CERN machines, the Proton Synchrotron and Super Proton Synchrotron have been slightly modified so that they can in turn accelerate the bunched beams to 3.5GeV and 20GeV respectively, before final injection into LEP.

---

[1] Centre Européene pour la Recherche Nucléaire

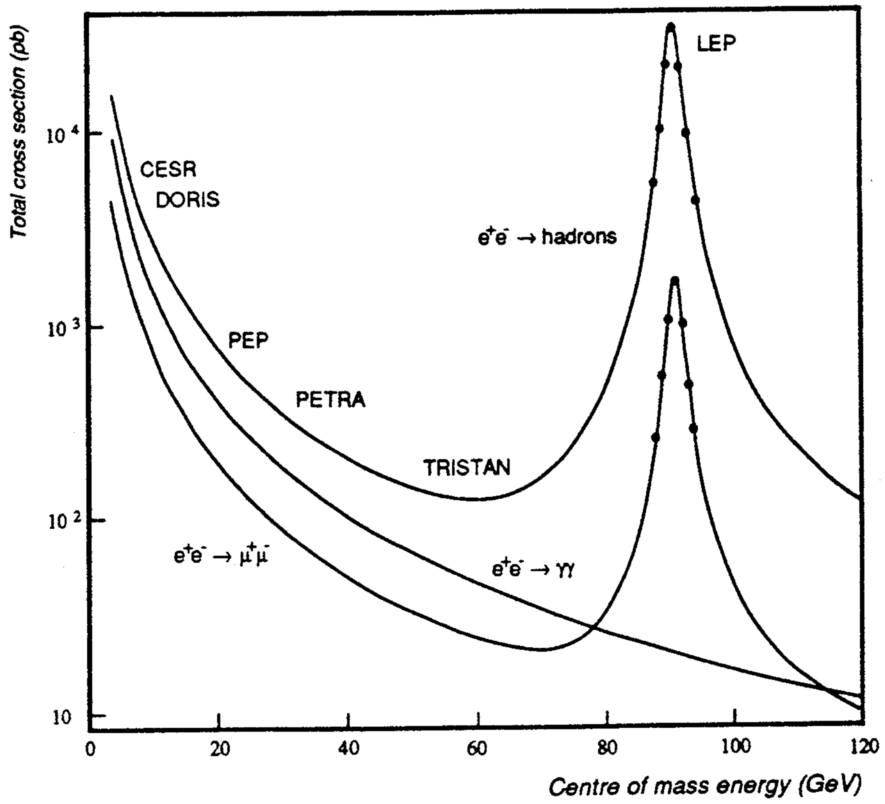

Fig 1.6; Cross section for e^+e^- production processes as indicated, showing the DELPHI data points on the Z^0 pole. The LEP machine was built to verify the form of these curves, and to examine all aspects of Z^0 physics.

Acceleration in LEP is due to a series of RF oscillating cavities around the LEP ring. Dipole magnets establish the orbit of the circulating bunches, and quadrupoles and sextupoles are used to correct the orbit if need be. [redacted]

One fill of the LEP ring may last a few (<10) hours, before beam intensities have been lost and re-injection of the beams is necessary.

It is a facet of the accelerator design that the circulating beams are physically much broader than they are high. The cross sectional area occupied by a beam focussed at the interaction point is typically 500μm in the horizontal plane by only 40μm in the vertical plane. The size and shape of

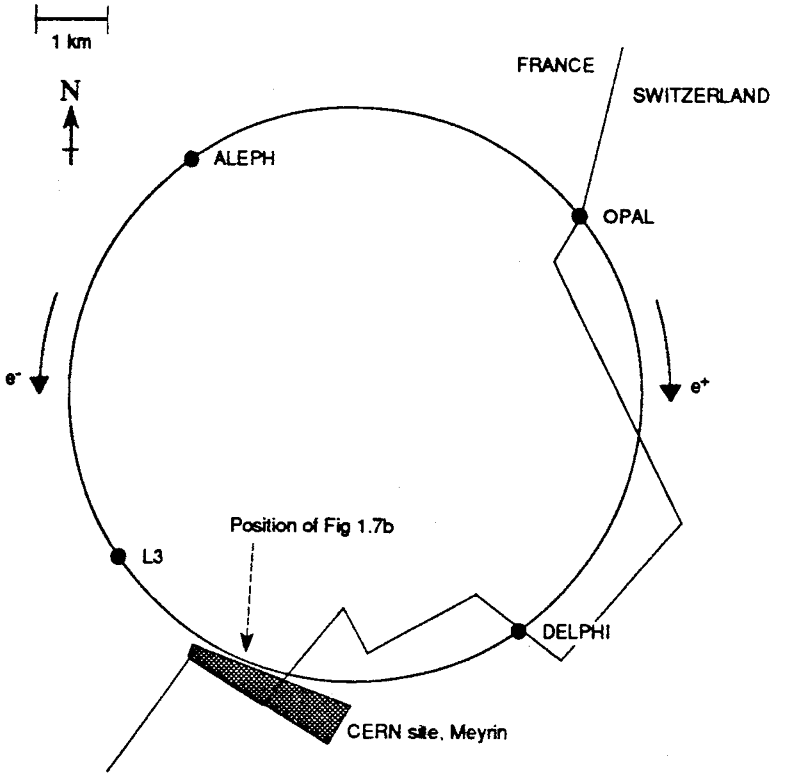

Fig 1.7a; Positions of the four experiments on the LEP ring, showing also the Franco-Swiss border and the position of the CERN site at Meyrin. See also inside back cover for aerial view of CERN.

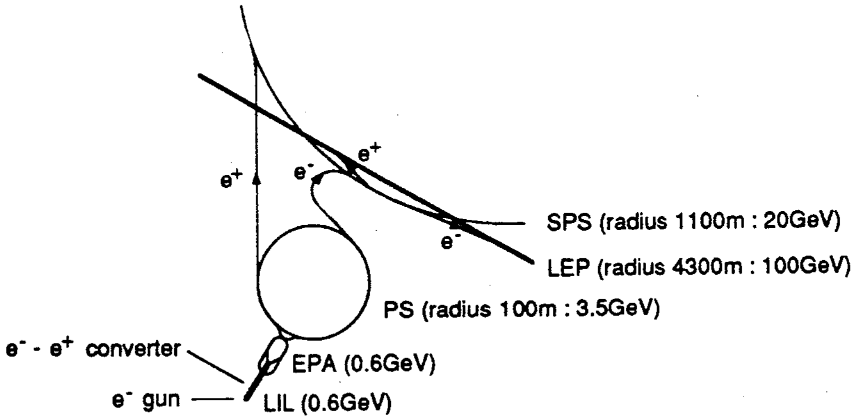

Fig 1.7b; The LEP injector chain.

the beam interaction region will be important where the τ lifetime measurement is concerned, and will be discussed in some detail in Chapter 6.

1.2.2 Methods for the τ lifetime

Traditionally, two methods have been used to determine the lifetime of the τ. One involves a direct measurement of the distances individual τs travel from the point of production, in the plane transverse to the incident beam. This measurement is based on the principle of secondary vertex reconstruction (Fig 1.8). Another method uses the fact that a shortlived particle contributes to the impact parameter a secondary track makes to the point of production (Fig 1.9). A sign convention for impact parameter can be introduced, such that the mean measured impact parameter for charged tracks from τ decay is directly proportional to the lifetime of the decaying τ particle. Maximum likelihood techniques can be used to find the lifetime value which best fits distributions observed in the real data.

Both lifetime methods require knowledge of the point at which the $\tau^+\tau^-$ were produced. This is usually assumed to be the centre of the incident beam, and a limitation on the precision with which the lifetime measurement can be made is clearly introduced here. The position and size of the beam are estimated by fitting primary vertices to hadronic events. The beam is measured over some suitable period of time, such that it does not wander excessively, and yet event statistics are still high.

The two methods for the τ lifetime provide, ultimately, comparably accurate and precise results. At DELPHI, both have been employed[1]. A measurement of the τ lifetime by impact parameter method is detailed in this thesis. No description of the measurement by secondary vertex reconstruction, carried out independently, is included here.

The τ lifetime measurements are both heavily reliant on the DELPHI silicon strip microvertex detector. The microvertex is designed to provide two tracking coordinates per track with a precision in $r\phi$ of 5μm, and as such has a strong influence on track extrapolation resolution near to the

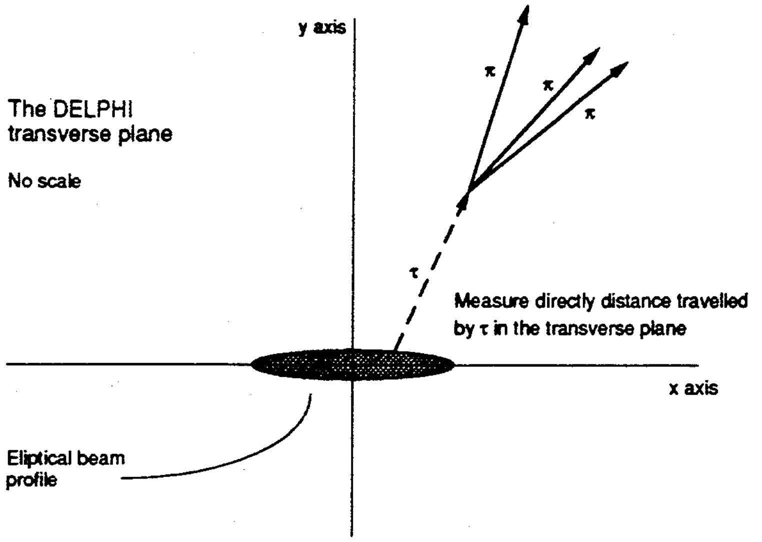

Fig 1.8. Secondary vertex reconstruction of a 3-prong system allows measurement of the distance of flight of the τ in the rφ plane.

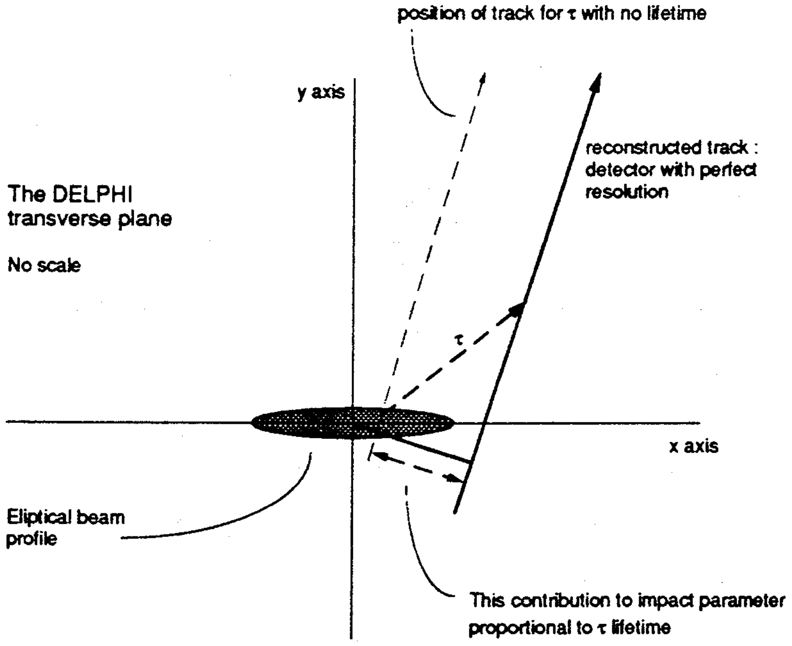

Fig 1.9. The finite τ lifetime increases the impact parameter made by a track from τ decay to the assumed point of production.

primary vertex. Chapter 3 is dedicated to a description of the microvertex detector. Its performance is demonstrated in Chapter 4.

Chapter 2. The DELPHI experiment

DELPHI is a DEtector for Lepton, Photon and Hadron Identification. Electron and positron beams collide at its centre, and the particles produced in any resulting interaction travel outwards through the various subdetector modules. The interactions occur at rest in the laboratory frame, and so the design of DELPHI is symmetric about the interaction region.

DELPHI is a general purpose detector, with emphasis on the provision of three dimensional information to accompany every tracking segment and energy deposition. Good particle identification was an important feature of the design specification, as was detector acceptance approaching 4π solid angle. In DELPHI, two endcap subdetector assemblies occupy the open extremities of a cylindrical barrel, the axis of which is coincident with the beam. The subdetectors of the barrel and those of the endcaps perform largely equivalent functions.

The component subdetectors within DELPHI are shown in the cutaway diagram of Plate 1 (see inside front cover) and the sectional drawings of Fig 2.1. Those components which are used in this τ lifetime measurement (principally the barrel tracking and calorimetry detectors) will be described in some detail in this Chapter. The τ lifetime measurement relies heavily on the silicon microvertex detector, which provides high precision tracking information in azimuthal angle close to the beamline. Chapter 3 is devoted to a description of the design of the microvertex detector. The function of subdetector components not central to this analysis will be outlined only in brief below : a more complete description of the DELPHI detector may be found in refs [9, 10].

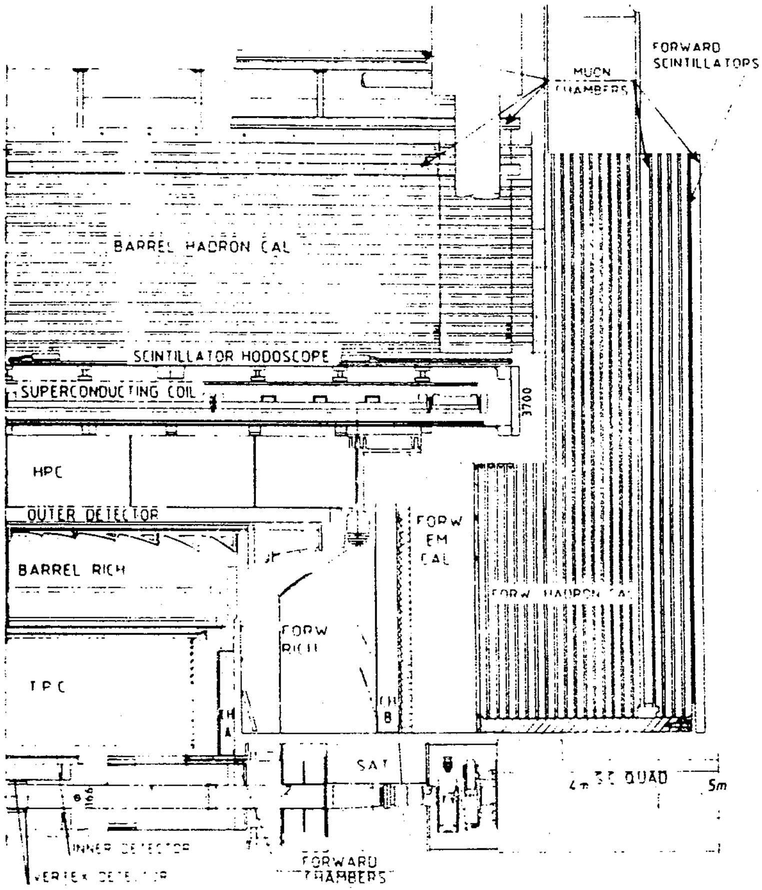

Fig 2.1a; Longitudinal view of the DELPHI detector.

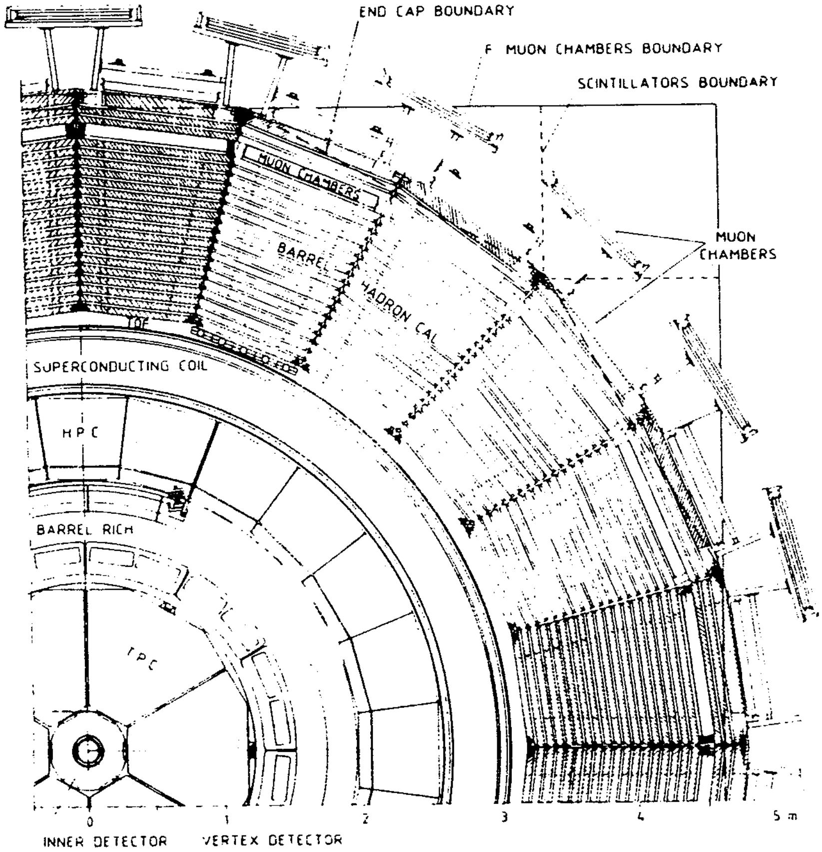

Fig 2.1b; Transverse view of the DELPHI detector.

2.1 General

2.1.1 The DELPHI coordinate system

Two coordinate systems will be used here to identify points in space within DELPHI. Endcap regions are described in terms of right handed cartesians, and the barrel in cylindrical polars, where the choice of coordinate system reflects the inherent symmetry of the respective subdetector assembly.

Fig 2.2 defines the orientation of the coordinate axes with respect to the beamline and the geometry of the LEP ring. The origin of the coordinate systems is at the interaction point, and the electron beam defines the positive z axis.

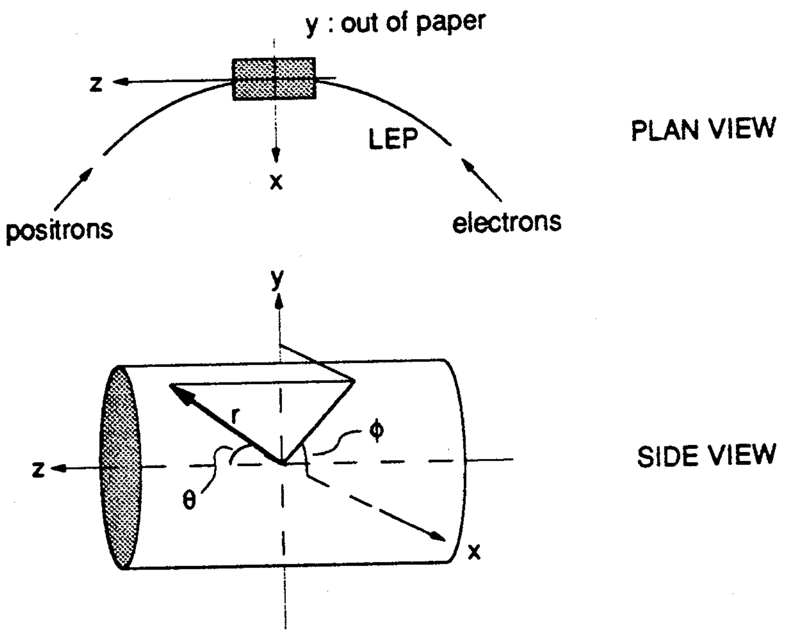

Fig 2.2; The DELPHI coordinate system.

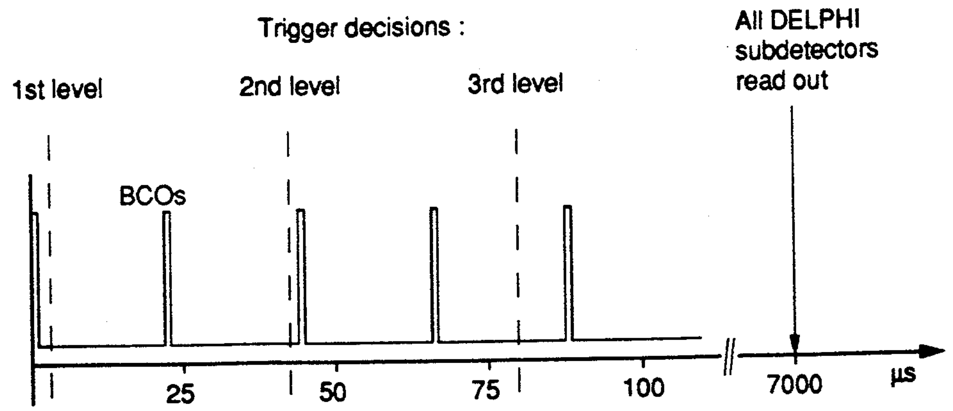

Fig 2.3; The DELPHI readout timescale.

2.1.2 DELPHI timing

Bunches of electrons and positrons cross within DELPHI every 22µs. At every beam cross over (BCO), an electromagnetic beam pickup starts a timing clock, and defines T=0, to which all DELPHI timings are referred. To read out the entire DELPHI detector takes 7ms, during which time the detector is insensitive to further event data. Not every BCO results in the creation of a Z^0 particle : in the interests of efficiency, fast online preliminary data analysis must decide whether or not to trigger the DELPHI readout system, at the cost of the following ≈300 BCOs.

The DELPHI triggering system is of hierarchical design. A first level decision is made as early as at T=3µs, rejecting those BCOs where it is clear an event has not taken place. A more careful second level trigger decision is made at T=40µs : after a first level positive trigger, DELPHI's dead time only extends beyond one following BCO. Third and fourth level triggers are envisaged for the future, at variable times T≈80µs and T≈400µs respectively.

Fig 2.3 shows schematically the timing of the DELPHI detector readout. More detail of the trigger is given later, in section 2.7.

2.1.3 The DELPHI superconducting solenoid

In general, particle momentum measurements rely on the determination of track curvature in a magnetic field;

$$P_t = 0.3BR \tag{2.1}$$

where P_t is particle transverse momentum in GeV/c, B is the magnetic field strength in Tesla and R the observed tracking radius in $r\phi$ projection in metres. Electron-positron collisions occur with DELPHI at centre of mass energies close to 100GeV : a strong magnetic field is required if the circles described by tracking particles are to have measurable radii (≈100m or less - see also section 2.2).

A magnetic field is produced within DELPHI parallel to the beamline by a superconducting solenoid of length 7.4m and inner diameter 5.2m. A single layer of superconductor at a temperature of 4.5K carries 5000A to generate 1.2T fieldstrength. The field is contained by an iron return yoke. The solenoid cryostat provides physical support for the barrel assembly of detectors.

For optimal operation of tracking chambers, it is important that the magnetic field be homogeneous throughout the detector. To maintain field homogeneity at the extremities of the detector, an independent compensating coil 35cm long in z is positioned at each end of the solenoid, and contributes towards a partial second superconducting layer. After optimisation of the compensating currents, the longitudinal field strength is uniform to better than 0.01% over the entire length of the detector. Measured in the time projection chamber (section 2.2.2), the radial field is less than 5×10^{-5} as strong as the longitudinal field.

2.1.4 The beampipe

Choice of beampipe material is important in determining the degree of multiple scattering particles from Z^0 decay undergo close to the primary vertex. The central 32cm section of the beampipe within DELPHI is of smooth aluminium, with a wall thickness of 1.2mm, corresponding to 0.3% of a radiation length.

The radius of the beampipe is important in determining the density of synchrotron radiation photons arriving at the centre of DELPHI. Such photons can cause problems by interacting with the beampipe wall inside the active detector region, producing spurious charged tracks in the detector unconnected with Z^0 decay. The inner pipe radius of 79.2mm was chosen so that geometrically, only photons backscattered twice could reach the centre of DELPHI.

2.2 Barrel tracking chambers

The barrel tracking detectors cover fully the polar angle between $\theta=41°$ and $\theta=139°$. Tracking is based around the time projection chamber, with the inner and outer detectors included to improve momentum resolution. In particular, the outer detector compensates for the small size of the time projection chamber, limited in radial depth to make space for the barrel Cherenkov detector (section 2.4.2).

In the τ lifetime analysis of Chapter 6, tracking detectors will be used primarily to determine the momenta of charged tracks. The transverse momentum P_t of a charged particle travelling through the DELPHI magnetic field is calculated from its tracking radius R as seen in $r\phi$ projection (equation (2.1)). The radius R is in turn obtained from the length c of the chord AC joining the ends of the track segment being measured, and the so called sagitta distance h (Fig 2.4). By Pythagoras' rule in triangle OAB,

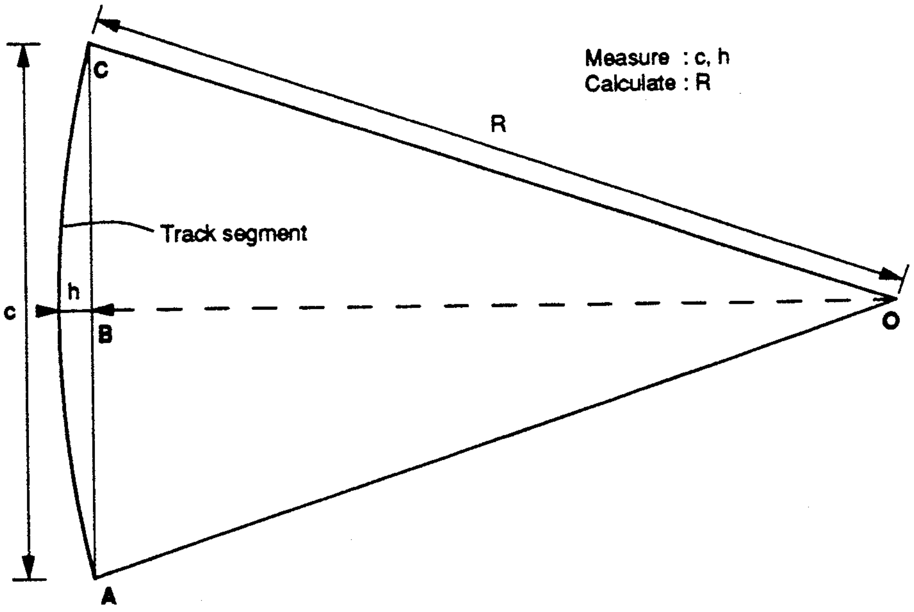

Fig 2.4; The measurement of momenta. The transverse momentum of a track is calculated from the radius of the circle the track makes in the transverse plane, in turn calculated from measured distances h and c (equations 2.1,2.2).

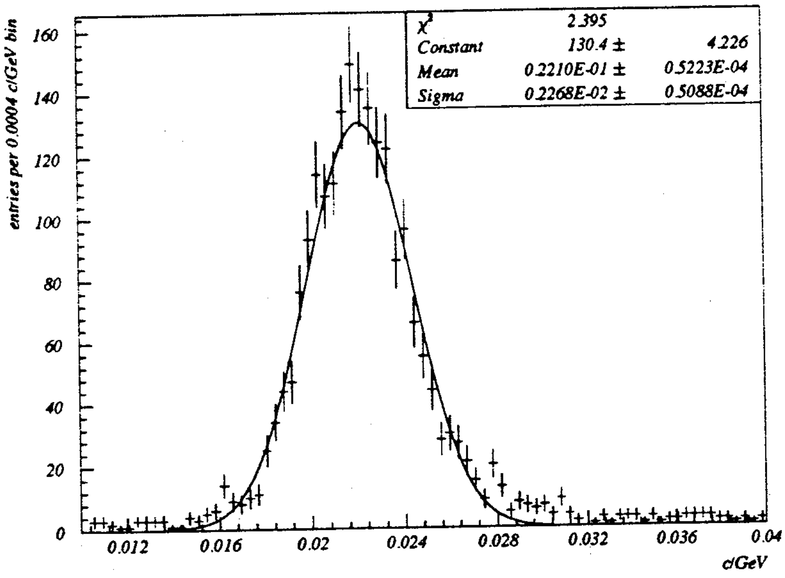

Fig 2.5; Distribution of $1/p_t$ for dimuons from Z^0 decay.

$$R = \frac{1}{8h}\left(c^2 + 4h^2\right)$$
$$\text{i.e.}\quad R \approx \frac{c^2}{8h} \qquad (2.2)$$

where the second approximation is valid as h is typically a few hundred μm and c one metre.

A consequence of the relative magnitudes of c and h is that it is the random measurement error on h which dominates in determining the errors on R and hence P_t. From equations (2.1) and (2.2), P_t is inversely proportional to h, and so uncertainties on $1/P_t$ are well described by a random error treatment. The Gaussian width σ_{1/P_t} of the $1/P_t$ distribution can be estimated from the inverse momentum distribution for tracks from dimuon Z^0 decay (Fig 2.5). Tracks from dimuon Z^0 decay are used because they are monoenergetic, and so the plotted distribution is not broadened by any physical distribution of momenta. From the figure, transverse momentum resolution for fast tracks σ_{1/P_t} is measured as $0.002(\mathrm{GeV/c})^{-1}$.

2.2.1 The inner detector (ID)

The inner detector is positioned between radii of 118mm and 280mm. It provides rϕ information on charged track segments to a precision of better that 100μm, with a two track separation of 1mm.

The ID is a detector of two parts. Innermost is a 24-sector drift chamber, in which charged particles ionise a CO_2-based gas mixture to produce free electrons. In each sector, a maximum of 24 rϕ coordinates per track can be calculated from electron drift times to 24 anode wires running parallel to the z axis. Outside the drift chamber there are 5 multiwire proportional chamber (MWPC) layers, each of 192 wires in the z-direction and 192 circular cathode strips (Fig 2.6). The MWPC layers provide information in rϕ and z, available within a fast readout time of 2μs, and used in the first level DELPHI readout trigger. Where particle tracking is concerned, the MWPC rϕ information serves to resolve left-right ambiguities in the data from the drift chamber.

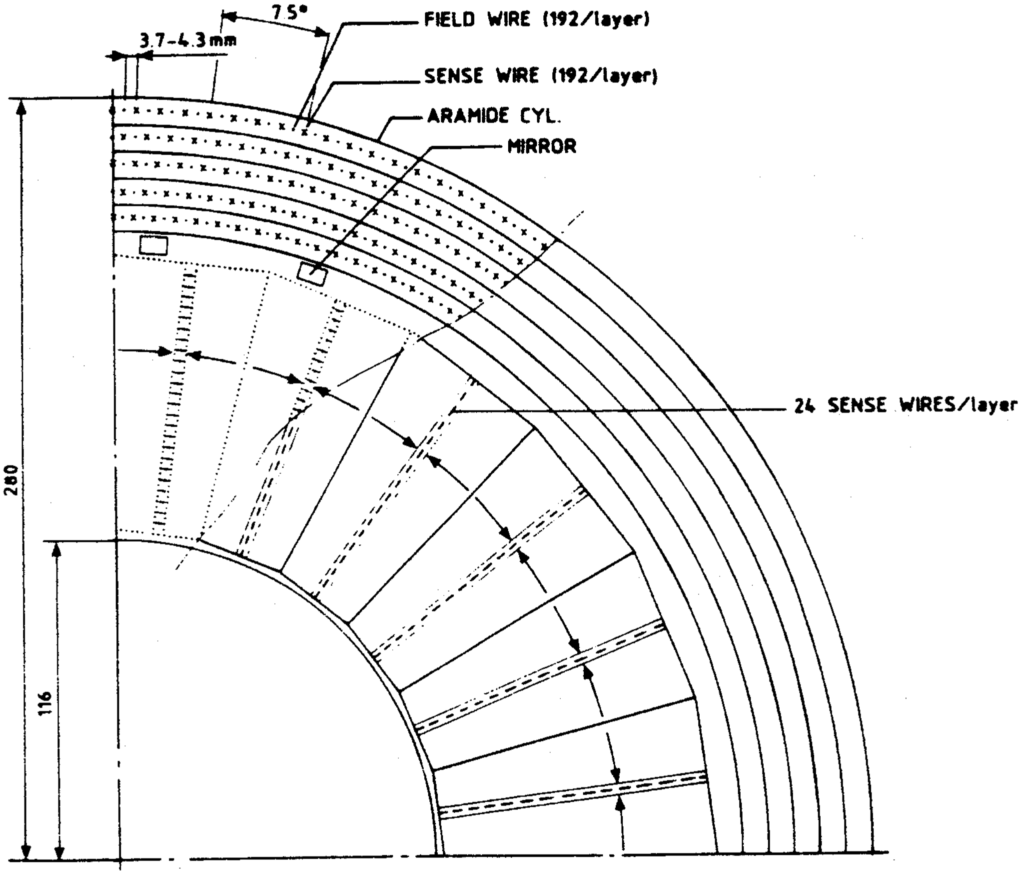

Fig 2.6; Transverse view of the inner detector.

2.2.2 The time projection chamber (TPC)

The TPC occupies the radial space in DELPHI between 40cm and 120 cm, and is central to the tracking pattern recognition. Three dimensional track segments of ≈1m in length can be measured with a two track separation of 1.5cm and resolution per space point (of which there may be up to 16) of ≈200μm in rϕ and <900μm in z. In addition, particle identification is possible, through a measurement of the amount of charge ionised per unit track length (dE/dx measurements). Design specifications were, however, for good tracking resolution at the expense of particle identification capability. The DELPHI Cherenkov detectors are dedicated to providing the latter information.

Physically, the TPC is divided into 2 halves in z, and is symmetric about the θ=90° plane. Each half is wired in 6 sectors in ϕ, making 12 readout divisions in all. The entire internal volume of the detector is occupied by an 80%-20% Ar-CH_4 mixture at a controlled pressure of 1 atmosphere. There is therefore little occurrence of multiple scattering or photon conversion in the TPC.

The function of the TPC is shown schematically in Fig 2.7a. An electric field of 150V/cm parallel to the z direction is set up between the central plane at high negative voltage and a set of field wires close to the TPC end planes. Alternating with the field wires are anode sense wires, on which the electric field converges (Fig 2.7b). Ionised electrons drift steadily through the main body of the detector, and avalanche onto the anode wire when they enter the region of increasing electric field strength. The gas gain results in detectable charge being deposited on the anode wire. Particle identification is in principle carried out by measuring the amount of charge deposited. Position information in rϕ is obtained from an array of cathode pads on the end planes, on which charge is induced by the anode wire signal. z position information is derived from drift time measurements in the electric field.

Having a long electron drift distance, the TPC is one of the more sensitive detectors to field aberrations in DELPHI. Two factors concerning electron drift dominate the performance of the TPC. Optimisation of the currents in the solenoid compensating coils (section 2.1.3) is necessary to maintain magnetic field strength and direction near the ends of the detector. Equally, electric field distortions can arise from the unavoidable build up of free charge that occurs within any tracking

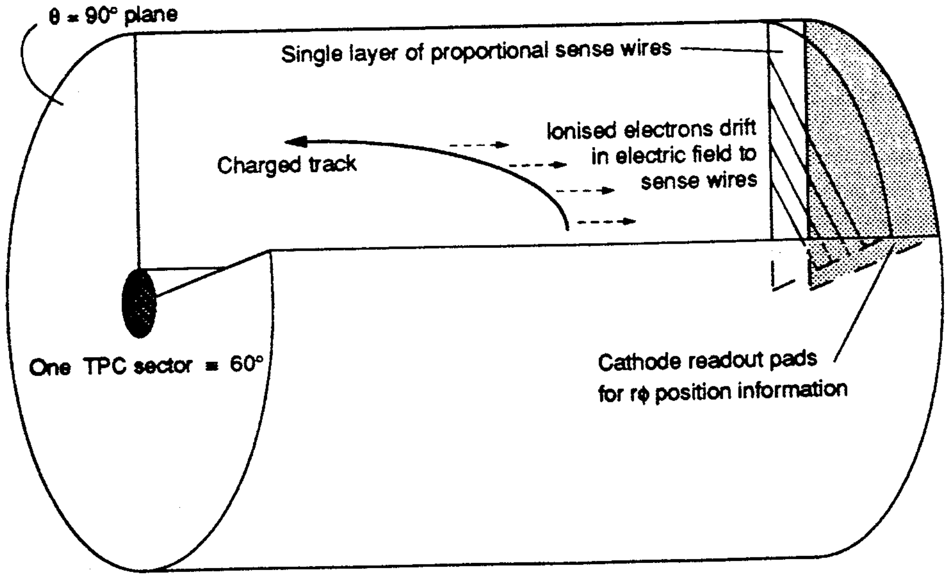

2.7a Charged particles ionise electrons which are detected at the end planes.

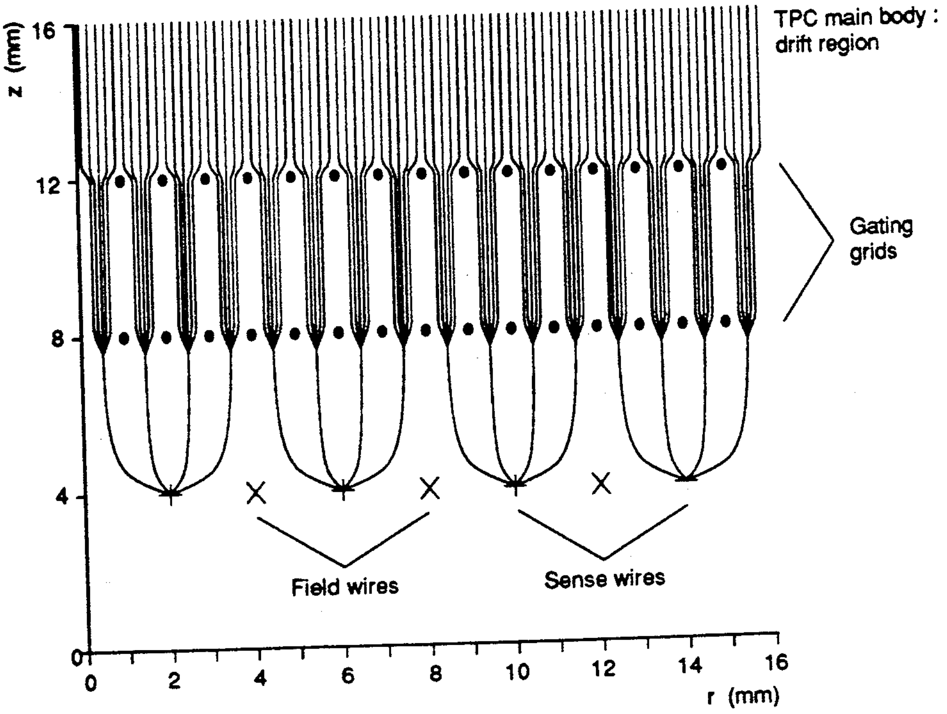

2.7b Electric field pattern within the TPC.

Fig 2.7; Operation of the time projection chamber.

detector of time projection chamber design. Positive ions generated in the avalanche region around the anode sense wires can migrate into the body of the detector, where they distort the electric drift field. The migration of positive ions can be prevented during the dead readout time of the DELPHI TPC by introducing a gating potential grid of wires (Fig 2.7b) between the sense wires and the centre of the drift chamber.

2.2.3 The outer detector (OD)

At a radius of 2m from the beamline, the OD[11] is a drift tube device providing 5 layers of precise $r\phi$ information per track. Its specific function is to improve on the momentum resolution of the TPC. It also serves to enable continued tracking of charged particles outside the barrel Cherenkov detector, and to assist in the association to tracks of energy deposits in the calorimeters.

Physically, the OD is constructed as 24 modules in ϕ. The 5 drift tube layers are staggered, and the 24 modules overlapping, so that there is 2π detector acceptance in azimuthal angle (Fig 2.8). Three drift tube layers are equipped to give fast z information for input to the first level trigger.

Each of the 145 aluminium tubes bonded into a module is of internal square cross section $(16.5\text{mm})^2$, and has wall thickness 0.5mm (0.12% of a radiation length)[12]. Anode sense wires at the centre of each tube are held at high tension with respect to the tube walls. The tubes are operated in limited streamer mode : charged particles ionise electrons in the Ar-isoC_4H_{10}-C_3H_7OH (51%-48%-1%) gas mixture, which themselves produce further ionisation via ultraviolet photon radiation as they drift towards the tube centre. Drift time calculations give precise distances of closest approach of a charged particle to the anode sense wires. The tube staggering allows unambiguous pattern recognition and the production of a unique track segment.

The OD $r\phi$ resolution has been measured at $\approx 100\mu m$ per drift tube, and the z resolution at ≈ 4.4cm.

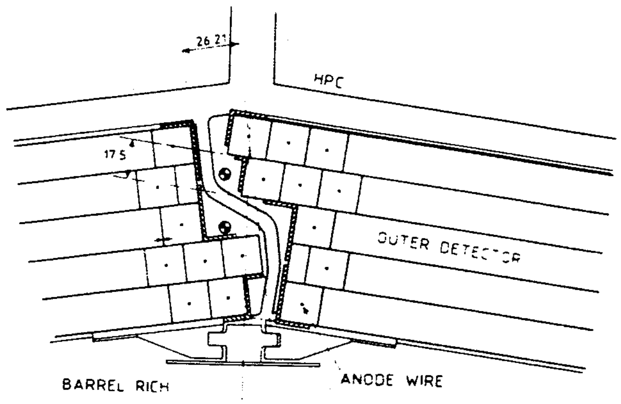

Fig 2.8; Operation of the outer detector. Overlapping modules give full azimuthal coverage.

2.3 Barrel calorimetry

2.3.1 The electromagnetic calorimeter (HPC)

Electromagnetic calorimeters measure the energy deposited by the passage of a charged particle through some dense material, often lead based. The amount of charge induced in the dense material and the three dimensional shape over which it is spread can be used to identify particle type. In particular, information from the DELPHI HPC will be used in the analysis of Chapter 5 to flag events where there are two final state electrons.

The HPC uses the High Density Projection Chamber technique[13] to record charge deposits, measuring three precise position coordinates, and the total energy deposited as ionisation. 144 modules (24 in $r\phi$ × 6 in z) of dimension 60cm×50cm×90cm contain a series of lead layers (18 radiation lengths of lead at θ=90°) 8mm apart from one another. Between the lead layers there is an Ar based gas mixture. Ionising particles cause electromagnetic showers in the lead layers : showering

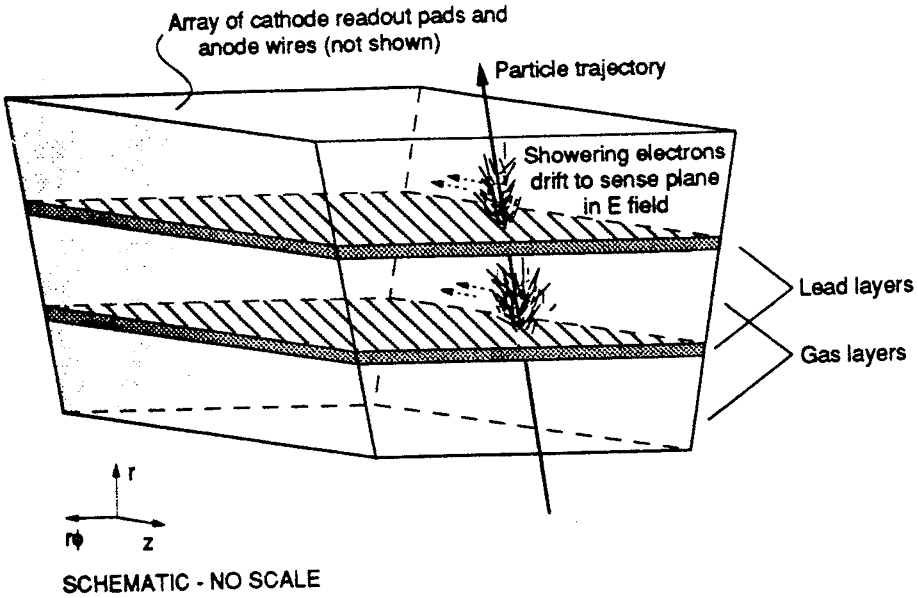

Fig 2.9; Operation of the electromagnetic calorimeter.

electrons which pass into the gaseous regions are drifted in the z direction in an electric field of ≈100V/cm. The electrons are counted at a single proportional wire plane at one end of each module within 12μs of BCO, as a measure of the energy deposit. Charge induced on an array of cathode pads behind the anode wires gives r and rϕ information, and drift times in the gas z information for the incident charged particle. The function of an HPC module is shown in Fig 2.9.

Like the TPC, the HPC is sensitive to the relative alignment between the magnetic and electric fields, due to the length of electron drift distance concerned. To ensure best possible relative alignment between the two, each of the 144 modules can mechanically be tilted in θ and in ϕ. Again, optimisation of the currents in the solenoid compensating coils is important (section 2.1.3).

2.3.2 The hadron calorimeter (HAD)

The HAD is a detector for measuring energy deposited by hadronically interacting particles. It is embedded in the return yoke of the superconducting solenoid, so that hadrons interacting strongly in the iron produce showers detectable in plastic streamer tubes. Leptonic particles tend not to interact in iron, and thus the two can be distinguished.

THE ONLY

WHICH COMMONLY PASS THROUGH
THE HPC ARE MUONS & THESE...

The HAD is not used in the physics analysis of this thesis, and is discussed no further here. A fuller description of the HAD may be found in ref [9].

2.4 Barrel miscellaneous

2.4.1 The barrel muon chambers (MUB)

The MUB comprises two layers of drift chambers positioned towards the outside of the iron magnetic field return yoke of DELPHI. The drift chambers positively identify muon tracks by recording the passage of charged particles as hits with two dimensional position information ($r\phi$ and z). Other particles do not traverse the yoke without interacting, and do not produce MUB hits.

The MUB is 24-modular in ϕ, and physically divided at $\theta=90°$ into two $\approx$4m long halves in z. In each 15° ϕ segment, an inner MUB module is situated 0.9m inside, and an outer module on, the iron of the return yoke. In addition, peripheral overlapping modules are included in the outer layer to give full azimuthal coverage (Fig 2.1b).

The MUB drift chambers are not designed in such a way as to give precise tracking information for muons. Even (minimum ionising) muons undergo considerable multiple scattering in the yoke, and precise position information for muons leaving the iron would therefore be of little interest. A drift chamber module consists of two layers of Al drift tubes, 20.8cm×2.6cm, with anode sense wires running parallel to the z direction. Muons produce ionisation in the Ar-CH_4-CO_2 85.5%-8.5%-6% gas mixture : coarse $r\phi$ information (resolution $\approx$2mm) is obtained from electron drift times, and z information (resolution 1.5cm) from signal pulse timing differences. The position information is used only in associating MUB hits to charged track extrapolations.

2.4.2 The ring imaging Cherenkov detector (RICH)

Included within the DELPHI barrel between radii of 123 and 197cm is the barrel RICH, a novel detector designed to identify hadronic particles over a wide range of momenta. The RICH compares particle momentum with speed as determined by the Cherenkov effect, so permitting calculation of particle mass. Currently only partially instrumented, it is not used in this analysis, and is described fully in ref [10].

Preliminary results from the RICH are encouraging[9]. It is to be hoped that the detector may start to contribute to physics analysis during 1991.

2.4.3 Time of flight counters (TOF)

172 TOF scintillator counters are positioned within DELPHI between the superconducting solenoid and the magnetic field return yoke. They provide almost full barrel coverage for fast event triggering (photomultiplier readout within 2μs) and cosmic track identification by timing measurements. The TOF can assess the arrival time of a particle in the scintillator material with a resolution of 1.2ns : cosmic rays take typically 20ns to cross the diameter of DELPHI.

The detection efficiency of the TOF for minimum ionising particles has been measured at 99.9%.

2.5 Endcap detectors

The endcap subdetector assemblies of DELPHI were not in a fully operational state at the time the physics analysis of this thesis was performed. No endcap detector is used in the analysis : brief mention of endcap layout is presented here by way of accompaniment to the schematic and sectional drawings of Fig 2.1. Detail of the endcap detector modules can be found in refs [9, 10].

In general, every barrel subdetector has its equivalent in the endcap assemblies. The forward RICH is based on similar principles of operation to its barrel counterpart, although it is currently only partially installed. The forward hadron calorimeter is of similar design to the HAD, and works well. The construction of the forward electromagnetic calorimeter FEMC, however, differs from that of the HPC. FEMC design is derived from the shower counter concept : electron showers in lead glass blocks produce light signals detectable at photomultiplier tubes on the passage of a charged particle or the conversion of a photon.

Particle tracking and momentum determination in the forward region rely heavily on the forward chambers A and B, multiwire drift chamber detectors mounted on the ends of the TPC and on the iron of the endcap return yoke respectively. Forward muon chambers are mounted outside the endcap yoke, and forward scintillating hodoscopes, for muon detection and triggering (cf barrel TOF), are situated at the very extremities of DELPHI in z.

2.6 Luminosity monitors (SAT and VSAT)

The probability that a high energy particle interaction occurs in which a specified initial state reacts to give a specified final state can be described in terms of a cross-section σ;

$$\sigma = \frac{N}{L} \tag{2.3}$$

where N is the number of observed events in which the reaction took place, and L is the luminosity of the colliding beams. In order to measure a cross-section, the machine luminosity must be known : the DELPHI Small Angle Tagger (SAT) and Very Small Angle Tagger (VSAT) are designed to give precise luminosity measurements by counting the number of final state dielectron events where electrons have exchanged photons rather than interacting via a Z^0 boson.

Luminosity measurements do not feature in the calculation of the τ lifetime, and no detail of SAT or VSAT operation is included here.

Trigger	**Notes**
TOF back-to-back	TOF divided into 8 quadrants; opposing quadrants fire
TOF singles × OD singles	TOF and OD both divided into 8 quadrants; both subtriggers fire (not necessarily correlated in space)
ID singles × OD back to back	OD divided into 8 quadrants; ID trigger layers find track segment and opposing OD quadrants fire
ID singles × OD majority 2	ID trigger layers find track segment and 2 of the 24 OD modules fire

Fig 2.10; Track triggers used in the selection of $\tau^+\tau^-$ events.

2.7 Trigger

Section 2.1.2 introduced the idea of a trigger decision, where fast online data analysis logic either starts the DELPHI readout system, or vetos a BCO as one where no e^+e^- interaction has resulted in the production of a Z^0. Triggering logic is based on the principle that a Z^0 event is likely to have occurred if

- likely track patterns are observed in the tracking detectors (the 'track' trigger)
- substantial energy deposits are seen in the calorimeters (the 'electromagnetic energy' and 'hadron energy' triggers)
- back to back muons are observed in the muon chambers (the 'muon' trigger)

Of these, only the track trigger and the electromagnetic energy trigger have as yet been implemented in the DELPHI barrel region.

The track trigger relies heavily on data from the TOF, the OD and the ID. Triggers are either of the 'back to back' variety, where an event is read out if there appear to be track segments in detector sectors diametrically opposite one another in DELPHI, or of the 'singles' variety, where a hit in any one sector constitues a positive trigger signal.

Fig 2.10 tabulates the triggers important for the selection of the τ data sample of this lifetime analysis. Trigger efficiencies, unimportant where a lifetime measurement is concerned, are all between 95% and 100%. More detail of the DELPHI trigger system can be found in ref [14].

Chapter 3. The DELPHI microvertex detector - design

Shortlived particle lifetimes are obtained experimentally from observed decay distances. The precision with which decay distances can be measured is determined by the ability of a detector to reconstruct particle trajectories close to the point of primary particle decay. At LEP energies, τ leptons travel an average of only 2.4mm during their lifetime. They therefore do not escape the beampipe : secondary track reconstruction must here be based on measurements made at least 8cm from the interaction point. The microvertex detector (VD) is a precise tracking device close to the beampipe, intended to facilitate short distance physics at DELPHI.

Vertex detectors have been used at a number of experiments for tracking purposes. Many have been of drift tube design[15-17], although recently trends have been towards the use of solid state detectors[18-20], for a number of reasons. Paramount in the design of a vertex detector is that its constituent material should represent a low number of radiation lengths, so that a minimum of multiple scattering occurs before tracking chambers more distant from the beamline. A silicon wafer 300μm thick represents only 0.5% of a radiation length. A vertex tracker should ideally occupy little space around the beam. The potentially high density of readout channels on a silicon wafer, and the low number of cables needed to service a solid state detector, make for a compact silicon vertex detector setup. With the development of sophisticated planar technology for the processing of high purity wafers of large surface area $\approx$(up to 10cm)^2, it has become feasible to produce silicon detector structures at reasonable cost levels.

This Chapter discusses the design and construction of a silicon microvertex detector for DELPHI. The performance of the detector in laboratory tests is discussed in Chapter 4.

3.1 Semiconductor particle detectors

The first steps towards the development of solid state particle detectors were taken during the 1930s, when Jaffe[21] noted that "the passage of electricity through [mica and quartz] crystals is distinctly affected by the passage of α-rays". By 1945, van Heerden[22] had developed a useful crystal detector, the electrical conductivity of which registered an increase on the passage of an ionising α particle.

It was not until 1951, however, that McKay published an experimental method in which a reverse biased semiconducting device was used to detect ionising radiation for the first time[23]. Incident α particles liberated electron-hole pairs in the depleted region of a reverse biased n-p diode in bulk germanium. The electron-hole pairs were quickly drifted away from the site of the ionisation in the depleting field, to register as a current pulse in external circuitry.

McKay's detection principle is that on which all modern semiconductor particle detectors rely. Fig 3.1 shows schematically the function of a typical solid state particle detector. The detector is essentially a semiconductor diode, polarised in the reverse bias 'no current flow' sense. The passage of a charged particle through the detector excites electrons, promoting them to states within the conduction band of the semiconductor material and leaving unoccupied hole states in the lower energy valence band. The newly liberated charge carriers drift away from one another in the electric field before recombination of the electron-hole pairs can take place. The flow of charge is measured as a current and the particle is detected.

In order to obtain precise position information from solid state detectors, it has recently become standard practice[19] to include many small p-type regions in a single n-type bulk crystal (Fig 3.2a). Many detectors are effectively combined into one in these so called microstrip detectors, and by inspecting separately the currents flowing in the various diode implants, a space coordinate as least as precise as the spacing of the p-type regions can be inferred. If charge integrators are used to calculate the total amount of charge Q_i that a particular particle causes to be deposited in the i^{th} diode, the centroid of deposited charge can give position information to an even greater precision. In the ideal case;

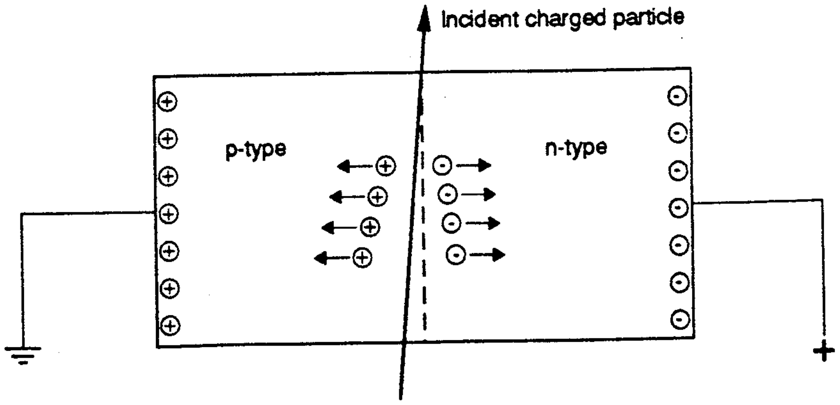

Fig 3.1; **Solid state particle detection.**

$$X = \frac{\sum_{i=1}^{N_{diodes}} Q_i x_i}{\sum_{i=1}^{N_{diodes}} Q_i} \qquad (3.1)$$

where x_i are the coordinates of the p-type regions in detector frame and X is the measured position coordinate (Fig 3.2a). Limitations to precision are then due to the ratios of signal pulse heights and detector noise (see section 4.2).

The density of readout channels which can be included in a microstrip detector has historically been limited by available space around the detector assembly and constraints of size on readout electronics and cabling. However, it has been found that if p-type regions which are not read out are included in the silicon between those which are, there is a further improvement in position resolution, beyond that which might otherwise be achieved at maximum detector granularity[24] (Fig 3.2b). Moreover, it has been shown that position resolution improves as the number of intermediate diodes included increases.

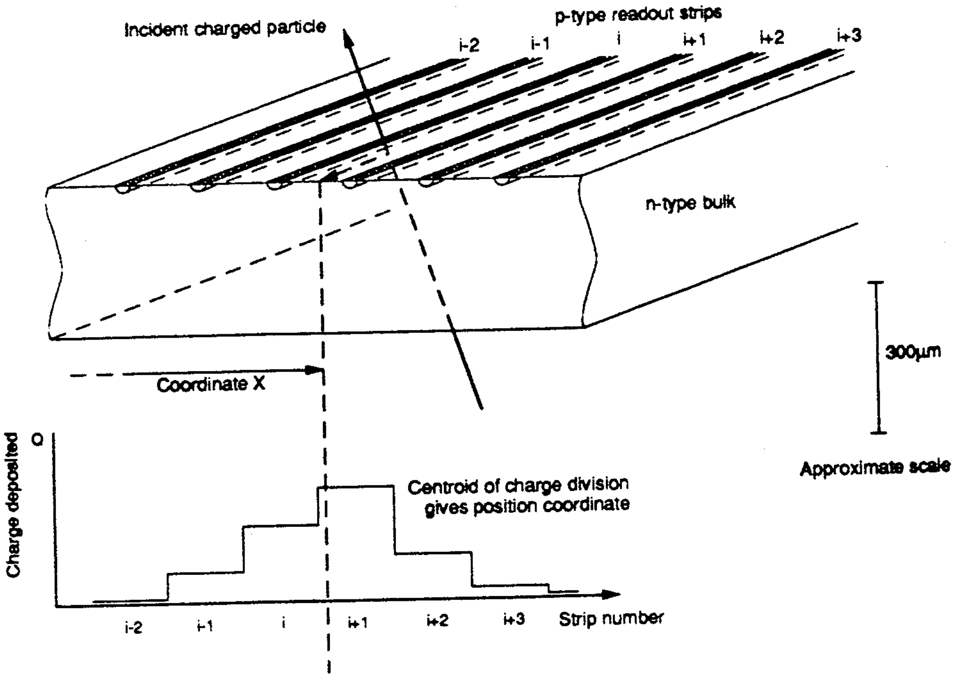

Fig 3.2a; Schematic drawing of a microstrip detector. Charge division gives position coordinate X (equation 3.1).

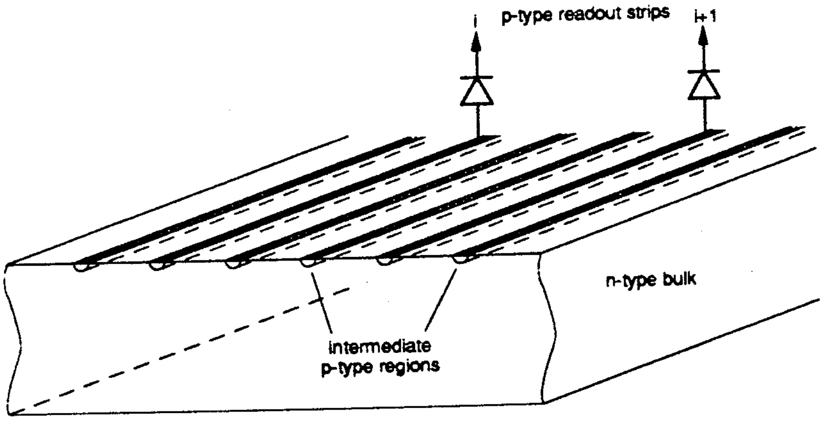

Fig 3.2b; Microstrip detector with intermediate diodes. In this example 1 in 3 p-type regions is read out.

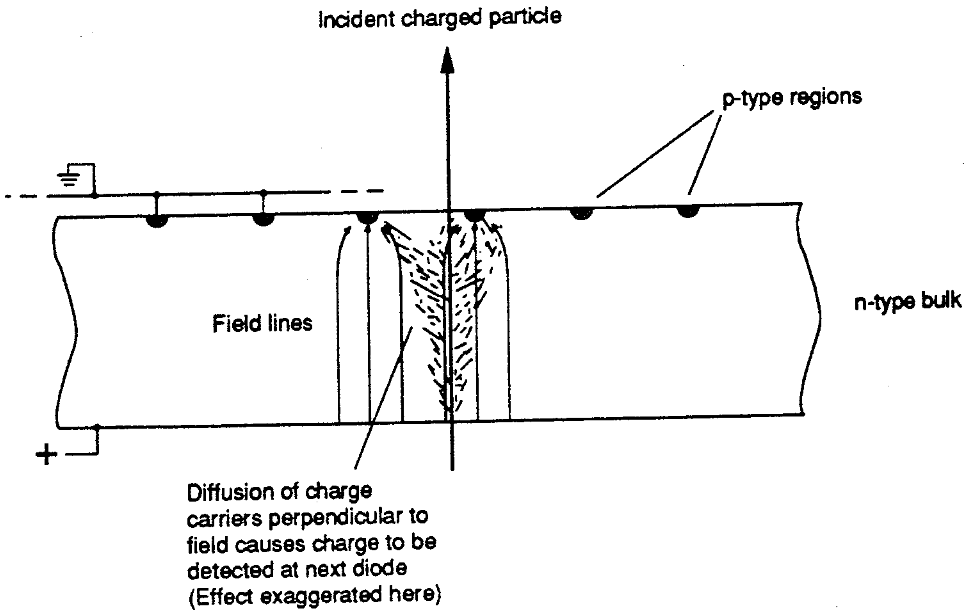

Fig 3.3; Charge carrier movement in a silicon detector.

To understand the effect of intermediate diodes on position resolution it is necessary to consider in more detail what happens to ionised charge on the passage of an incident charged particle (Fig 3.3) [19, 25]. Charge carriers are ionised in the depleted bulk throughout its depth, and subsequently drift along electric field lines towards (away from) the nearest p-type region. As they drift, diffusion perpendicular to the field direction causes some charge to migrate into the collection zone of a neighbouring diode. It is due to this mechanism that the principle of charge division can be applied.

In a silicon detector 300μm thick, carriers may migrate ≈10μm perpendicular to the drift field. Readout diodes are rarely spaced closer than 50μm from one another, and so even after diffusion most charge is collected at one diode. If a source of radiation were to be moved steadily across the detector perpendicular to the direction of the diode strips, charge would first be detected predominantly on one channel, and then move very quickly to its neighbour as the source passed the point half way between the two strips. Intermediate strips, coupled capacitatively to each other and to readout strips, have the effect of subdividing the detector bulk into a finer granularity of charge carrier collection zones, and consequently smooth out a sharp step function in readout signals into a more gradual division of charge.

When intermediate diodes are present, it is often sufficient to use a linear interpolation between two channels to determine position coordinate X. Equation (3.1) is then replaced by a simple charge division between neighbouring diodes;

$$X = x_i + D\frac{Q_i}{Q_i + Q_{i+1}} \tag{3.2}$$

where $D \equiv x_{i+1} - x_i$ is the diode implant spacing. Linear charge division such as this is used with the DELPHI VD (see also Chapter 4).

Typically, for a silicon detector 300μm thick, a readout diode spacing of 180μm and three or four intermediate diodes between readout diodes, detector resolution might be 5-10μm. However, for good two track separation in high energy hadronic events, it is necessary to have readout strips considerably closer (≈50μm)[26]. It then becomes unnecessary to include more than one or two intermediate diodes between readout diodes to attain the same resolution.

It should be noted in passing that the centroid of deposited charge, and hence the position coordinate measured, can in principle be displaced because of the kinetic energy of electrons ionised in the silicon by the passage of an incident particle. High energy δ-electrons can themselves result in secondary ionisation, and a significant shift (a few microns) in centroid position can result. The distribution in energy of the electrons, a Landau distribution, is however peaked at low values, so that in a silicon detector 300μm thick, there is only a 15% chance of the centroid being displaced by more than 1μm[27].

3.2 An overview of the DELPHI VD

The DELPHI silicon microvertex detector[28] was the first of its kind to be designed for use around a colliding beam machine. Previously, other experiments[29, 30] had used silicon microstrip detectors successfully in fixed target environments with point position resolutions of ≈5µm. The DELPHI VD design specification was therefore for a silicon detector giving $r\phi$ resolution per point of at most 5µm, over full azimuthal angle and between ≈90±45° in θ. Available space within DELPHI allowed for two concentric layers of silicon, necessary to allow good association between VD hits and hits in the inner tracking chamber.

Fig 3.4 shows a three dimensional view of the DELPHI VD. The VD is 24 modular in ϕ, and is symmetrical about the $\theta=90°$ plane. In each overlapping ϕ segment there are sensitive layers at average radii of 9cm and 11cm from the beamline and 12cm long in the z direction. Each layer constitutes four plaquettes of silicon supported by a carbon fibre backbone running parallel to the z axis.

The individual detector plaquettes are of phosphorous doped n-type silicon : boron doped p-type regions run parallel to the z axis, giving 512 readout channels in $r\phi$ per inner layer plaquette and 640 per outer layer plaquette, at 50µm pitch. Two plaquettes are read out in the positive z direction, and two in the negative z direction. The 1152 channels per $r\phi$ sector in a given z direction are read out serially, so that data from the entire detector are collated via only 2×24 twisted pair cables. Plaquette design and manufacture is described in section 3.3 below.

At either end of a four plaquette assembly is a printed ceramic hybrid circuit, on which front end charge integrating CMOS ICs described in section 3.4 are mounted. Together, four plaquettes and two hybrids are referred to as a module (Fig 3.5). Mechanical support for detector modules is via two semicircular aluminium endrings at either end, onto which the hybrids are screwed. The VD is thus split into two physically independent half cylinders at the y-z plane. The aluminium endrings are supported on two sliding rails per physical half shell on the walls of the inner tracking chamber, one at the bottom and one at the side of the detector as shown.

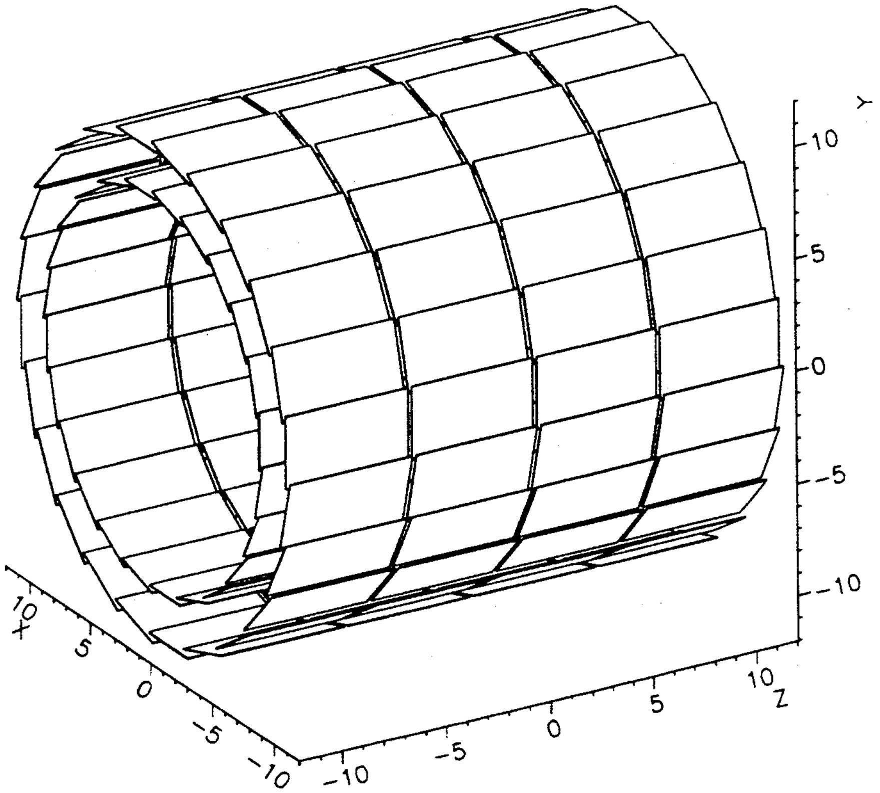

Fig 3.4; Three dimensional view of the VD, showing position of silicon plaquettes only. Axes are calibrated in cm.

The coefficient of thermal expansion of aluminium is $2.4\times10^{-3}\%$ per °C. Consequently a variation of 1°C in a block of aluminium of length 20cm results in $\approx 5\mu m$ expansion in that dimension. Thermal expansion and indeed any physical movement of the DELPHI VD can be monitored using lasers mounted on the inner walls of the inner tracking chamber, giving signals in the detector corresponding to known physical locations. To restrict thermal expansion to with $1\mu m$ it has been found experimentally that the detector should be kept at a stable operating temperature to within 0.2°C. Temperature regulation is via underpressure water flow through the aluminium endrings supporting the detector and nearby buffering electronics.

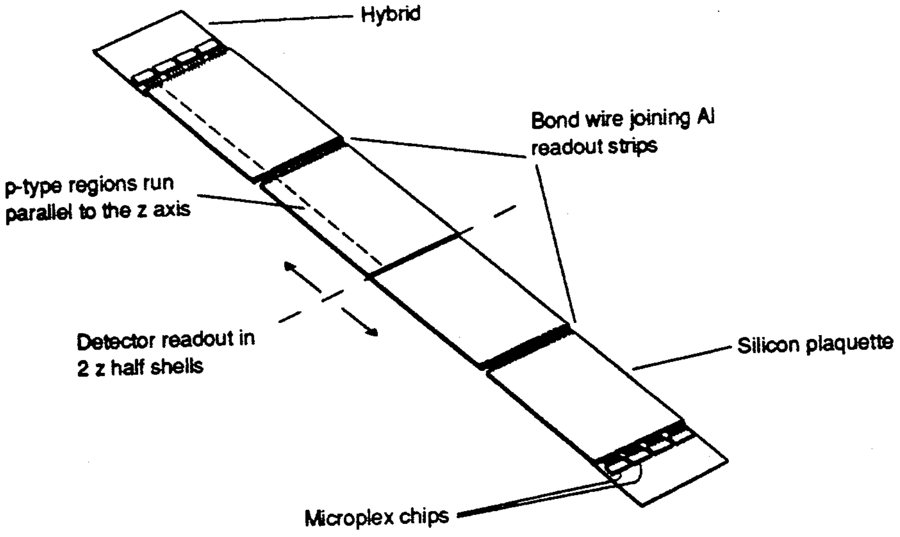

Fig 3.5; **An inner layer VD module.** Outer layer modules differ only in module width (number of readout channels - 5 CMOS Microplex chips rather than 4).

3.3 Design of a silicon plaquette

The silicon plaquettes of the DELPHI VD were made under contract by SI of Oslo, Norway. Full detail of their manufacture and detector quality assessment can be found in ref [31].

3.3.1 Technical description

Fig 3.6 shows schematically the internal layout of a silicon microstrip plaquette. P-type regions of width 10μm run parallel to the long axis of the plaquette with 25μm centre spacing. Every second of these is coupled to a readout preamplifier, so that the readout pitch of the detector is 50μm.

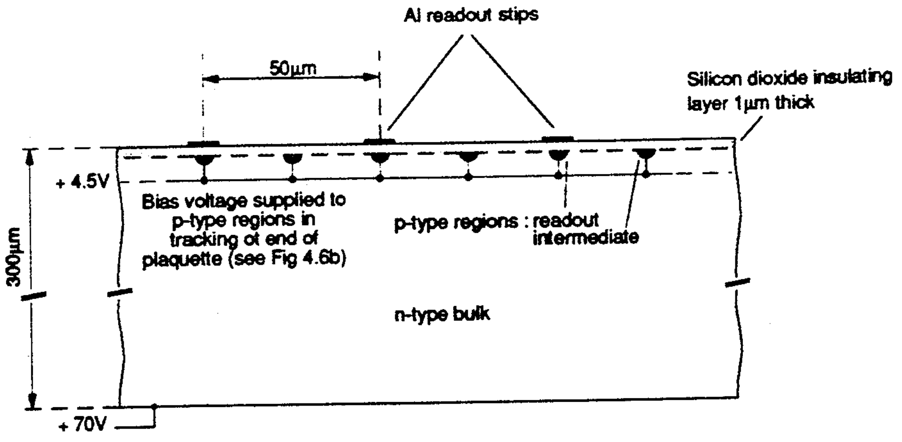

Fig 3.6a; Cross sectional view of a DELPHI VD silicon plaquette.

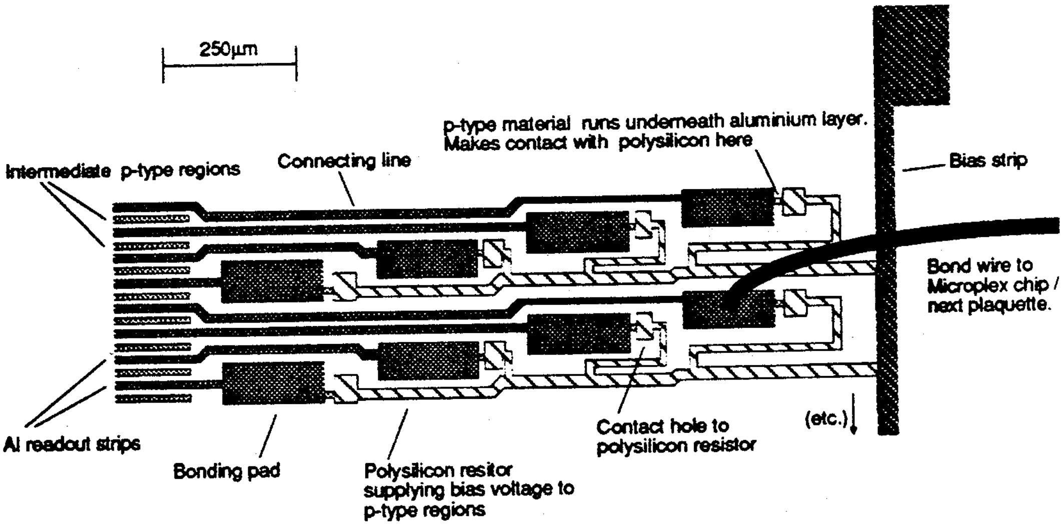

Fig 3.6b; Closeup of one end of a silicon plaquette. Showing tracks in the silicon and bond wire connections to Microplex chips / neighbouring plaquettes.

(SHOWN HERE - PROTOTYPE)

The p-type region to readout preamplifier coupling is of significantly different design from that of conventional microstrip detectors. Previously, charge deposits at diode strips have been measured as direct currents. By contrast, the diodes are here capacitatively coupled through 0.2μm silicon dioxide to aluminium readout strips on the upper surface of the detector. The capacitative coupling reduces leakage currents, and hence noise levels in the detector.

The aluminium strips are connected to CMOS electronics, and assume the input bias voltage of the front end amplifiers, 4.5V. The p-type strips are therefore also held at 4.5V to reduce to a minimum leakage currents through the silicon dioxide insulating layer. The connection to the diode strips is via 5MΩ polysilicon resistors incorporated within the plaquette, so that signal charge is not dissipated before it can be read out. In order to set up the depleting drift field in the silicon bulk, the aluminised plaquette backplanes are held at 70V.

The θ=90° plane divides the VD electrically (although not physically) into two halves. Plaquettes are read out in the direction of increasing $|z|$. Ideally, plaquettes would be twice as long in z to provide the required coverage. Manufacturing and cost limitations dictate that two smaller plaquettes must be connected together (daisy chained) to perform an equivalent function. The aluminium strips of neighbouring plaquettes in a given half-module are electrically connected by 10μm bond wire as shown (Fig 3.5). Similar bonding is used to connect the two plaquettes to the CMOS preamplifier chips.

3.3.2 Detector fabrication

The silicon plaquettes of the DELPHI VD were made using a standard planar process for detector fabrication[27, 32], where wafers are treated in batch for a many stage manufacturing process. Fig 3.7 shows the various stages of the processing, summarised in brief below.

Production starts with cleaned and polished high purity n-type silicon wafers of the required dimensions (3.7a). These are heated to a temperature of ≈1000°C in order to oxidise silicon to silicon dioxide in a surface layer ≈1μm thick (3.7b). The silicon dioxide is to be selectively etched away, where the p-type doping is to take place, and on the detector backplane. To this end, a protective

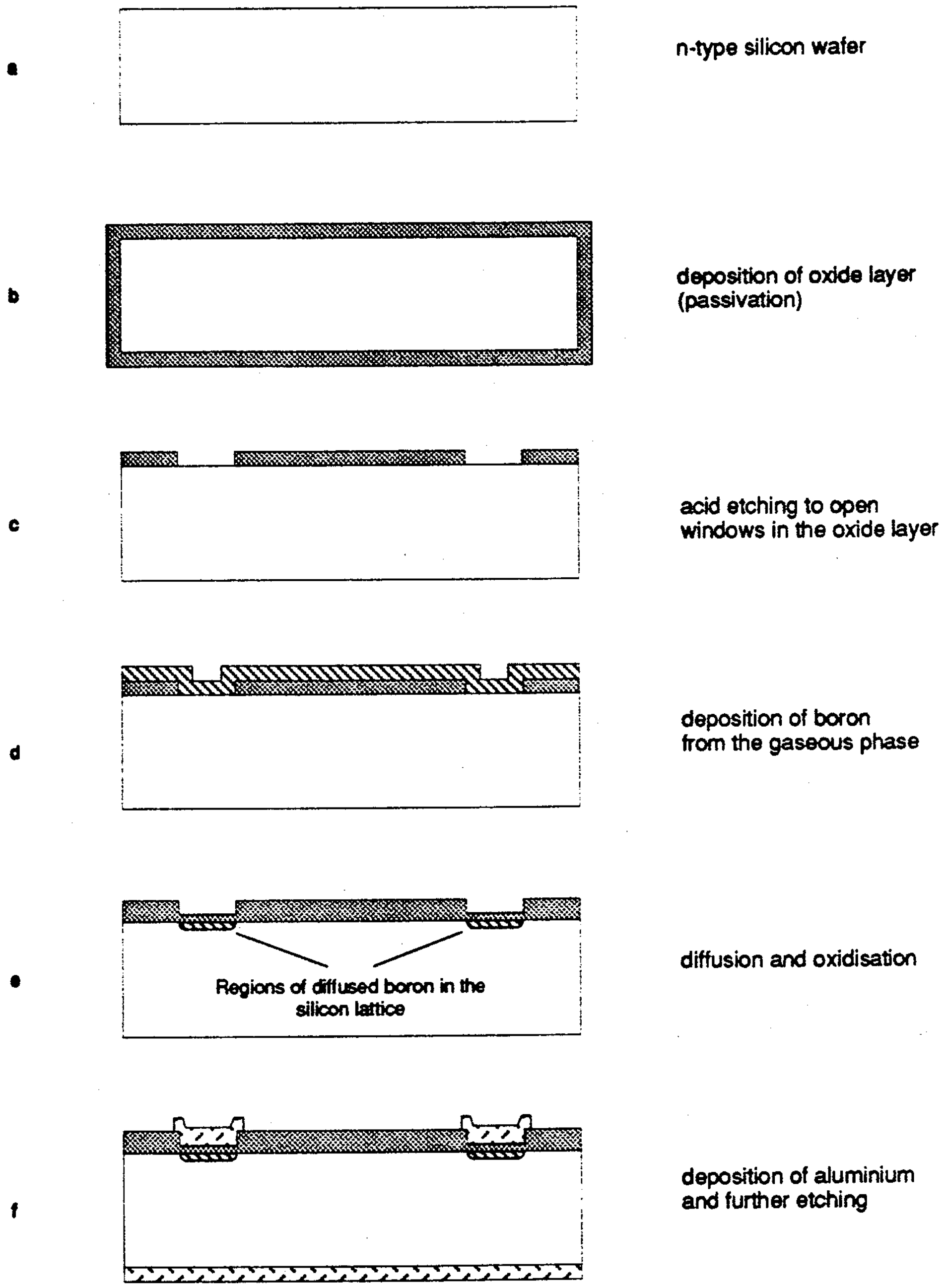

Fig 3.7; Fabrication of silicon plaquettes. See text for detail.

layer is temporarily laid down using a standard photolithographic technique[32], where the silicon dioxide is not to be etched on the front surface of the detector wafer. Acidic etching removes the silicon dioxide as required (3.7c).

The p-type regions in the detector are doped via a solid state diffusion technique. A layer of boron is deposited from the gas phase onto the front surface of the wafer (3.7d). The wafer is then held at ≈1000°C while atomic boron diffuses to a depth of not more than 1μm in the crystalline silicon lattice. The diffused boron is in higher concentration than the initial n-type dopant of the silicon bulk, so that the diffused regions will display heavily doped p-type semiconductor properties as required. Removal of excess boron and oxidisation result in many n-p junctions beneath an insulating layer of silicon dioxide (3.7e).

Aluminium metallised layers ≈1μm thick are deposited on both front and back planes of the wafers by direct evaporation. Further photolithography is used to remove most of the aluminium from the detector front face, leaving only enough to overlay the p-type regions and form the capacitative read out strips (3.7f). Polysilicon resistors and bias lines are inlaid into the wafer to connect with the p-type silicon regions in final photolithographic steps.

3.4 The VD data acquisition chain

Data from the microstrip VD are read out via very large scale integrated (VLSI) circuitry mounted on the hybrids at either end of a detector module. Preamplified signals are buffered at nearby repeater electronics for TTL transmission to Fastbus electronic racks ≈30m from the VD.

There are 4 (5) custom built CMOS Microplex chips[33] on each inner (outer) layer hybrid. Each chip contains 128 preamplifiers and circuitry to store output signals capacitatively for serial readout on an output bus. The 9 chips on 2 hybrids at the end of an $r\phi$ sector are read out on one bus, giving a multiplexing factor in the number of readout channels of 9×128=1156.

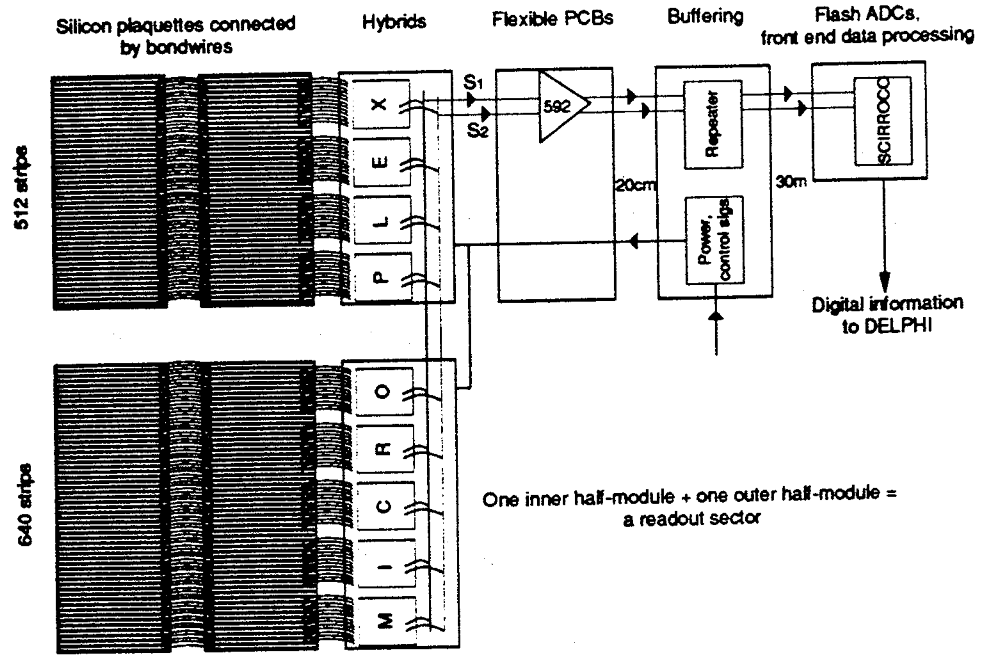

Fig 3.8; The DELPHI VD readout chain.

The 48 Microplex chip readout buses feed analogue signals to repeater electronics mounted around the beamline at a distance of only ≈50cm from the VD (Fig 3.8). The repeater electronics transmit differential twisted pair analogue information to SIROCCO cards[2] in Fastbus crates, where the signals are digitised and digital data preprocessing is carried out.

The hardware involved with the various stages of signal processing is now discussed in some detail.

---

[2] SIlicon strip Read Out Camac COntroller modules, originally developed in Camac but now updated to operate in a Fastbus environment.

3.4.1 The Microplex chips : readout timing

Fig 3.9 shows a closeup of a Microplex chip, and Fig 3.10 a circuit diagram for the readout method used to take data from the silicon plaquettes. The chip uses the double correlated data sampling technique, where signals just before and after the passage of a particle through the detector (effectively at BCO) are compared, to eliminate low frequency noise components.

The charge integrating amplifier is held reset until 3μs before BCO. 1μs later switches S_1 and S_2 are closed, allowing the voltage at the storage capacitors C_1 and C_2 to follow the output voltage of the amplifier (Fig 3.10b). S_1 and S_2 are opened 1μs before and 1μs after BCO respectively, so that any signal is recorded as the difference of the two stored voltages.

After S_2 is opened, either a trigger signal starts the VD readout, or the reset-S_1-S_2 cycle repeats. In the event of a positive trigger, clock pulses shift a bit along an output control register, selectively enabling each pair of capacitors onto the output bus in turn. When all 128 channels from the first chip in the readout sequence have been read out onto the bus the second chip is started : the nine chips at one end of a given $r\phi$ sector are read out as a continuous stream of data. The readout clocks run at 2.5MHz, and so the readout of the entire detector takes ≈460μs.

The inputs to the CMOS preamplifiers are capacitatively coupled (≈0.2pF) to calibration lines, along which pulses can be sent for test purposes. Four calibration lines service a whole detector half module : every fourth amplifier is connected to a given calibration line. The calibration lines will be used in tests in Chapter 4.

3.4.2 Repeater electronics

The repeater electronics serve to buffer signals to and from the detector. The multiplexed analogue data from the output bus of the microplex chips, and control signals and voltages to the detector, are passed via flexible cabling and a flexible printed circuit board to (from) impedance matching circuitry mounted round the beampipe on aluminium endrings.

Fig 3.9; Closeup of a Microplex chip, showing bond wire connections to silicon plaquette (right) and to hybrid tracking (left).

The flexible detector-repeater interconnections mechanically decouple the detector from the cabling running between the buffering electronics and the Fastbus racks containing the SIROCCO units. In addition, the analogue data signals are amplified at FAST IMPEDENCE MATCHING LINEAR DIFFERENTIAL VIDEO AMPLIFIERS (LM592, [45] [redacted] mounted on the flexible printed circuit boards.

3.4.3 SIROCCO units

SIROCCO units are built for Fastbus usage in two channel cards. Each SIROCCO channel contains a 10 bit flash ADC capable of sampling analogue information at rates of up to 5MHz (cf Microplex readout clock speeds of 2.5MHz). An event buffer can store up to four events at any given time before information is rejected and an event is lost.

A powerful digital signal processor on each SIROCCO channel carries out online preprocessing of the data, calculating the ADC pedestals and performing pedestal subtraction and zero suppression if

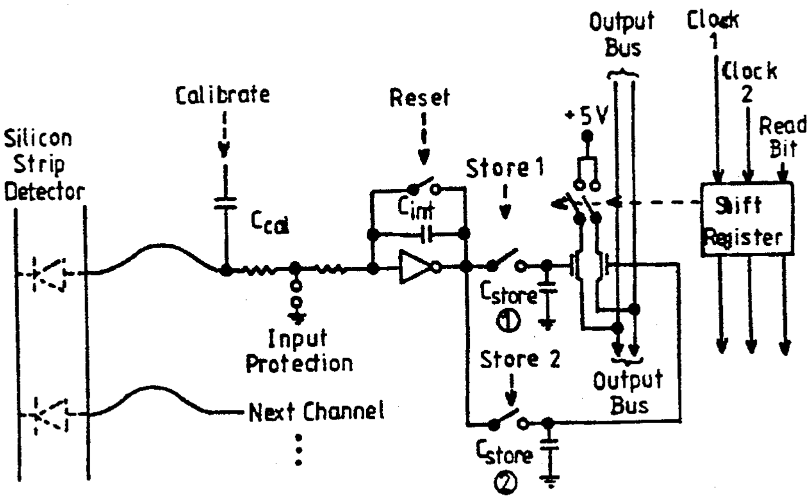

Fig 3.10a; Schematic circuit diagram for one channel in a Microplex chip.

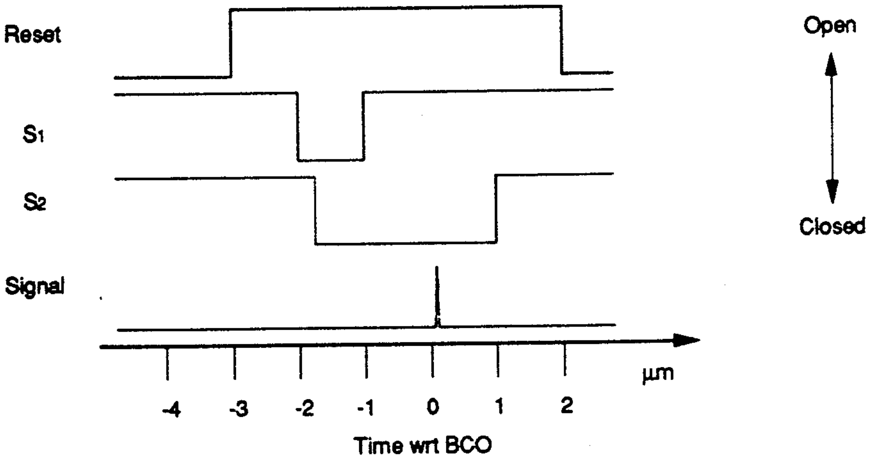

Fig 3.10b; Timing of control signals to Microplex chips.

so required. In addition, common mode noise, affecting all channels in a half-module alike, can be dealt with at this stage (section 4.2.1). Output stage buffering feeds event information to the DELPHI central data acquisition system in synchronisation with other equivalent subdetector Fastbus modules.

3.5 Surveying of the VD

For the VD to be useful in physics analysis, the positions of the detector plaquettes must be known relative to one another and to other DELPHI subdetectors. Initial surveying of plaquette positions was carried out before the VD was installed within DELPHI, using a touch probe precise to $\approx 10\mu m$. Subsequent alignment was carried out by minimising detector residuals to tracks from hadronic events and from dimuon decay of the Z^0. The $r\phi$ resolution obtained with the detector in situ is discussed further in Chapter 6.

Chapter 4. The DELPHI microvertex detector - performance

A full microvertex detector was installed in DELPHI for the first time in March 1990. The detector took data throughout the 6 month LEP running period of that year, performing in the experimental environment at close to design specification levels.

This Chapter contains detail of quality control tests performed in the laboratory before individual detector modules were installed in the VD. The tests were designed to pinpoint regions of the detector that did not function as they should, identifying the cause of the fault where possible. Test results were compiled in a detector performance database described in section 4.3, which could be accessed by offline track reconstruction software.

Characteristic behaviour of VD modules is demonstrated in sections 4.1 to 4.3, where experimental distributions from laboratory tests are given. A summary of general detector performance can be found in ref [34].

4.1 Laboratory testing

If the data supplied by a detector are to be reliable, it is in general necessary to know how well each and every channel in the detector is expected to perform. For instance, tracking coordinates supplied with some nominal spatial precision will distort the reconstruction of an event, if the detector region supplying the data is in reality performing less well than indicated. It is common practice to store information in a calibration database, where bits in words are set if a particular channel is for example dead, noisy or crosstalking to its neighbour.

In order to obtain channel by channel information on the performance of the DELPHI VD, test procedures were established as follows. Firstly, the calibration lines (Fig 3.10a) were used to supply calibration pulses to the front end amplifiers of individual channels in isolation. In another test, calibration pulses were supplied to the to the aluminised detector backplane, so that the electrical continuity of each channel in the whole detector assembly could be tested. Finally, laser light was directed onto the backplane to simulate the passage of an ionising particle. The test data obtained characterised every VD channel within DELPHI according to the behaviour of its diode and amplifier.

Tests were run on hybrids and modules at various stages of construction, so that some degree of quality control could be imposed on detector construction techniques. The detector assembly to be tested was mounted in a light tight box, and data were read out in the normal way into a SIROCCO card. A custom built CAMAC interface was used to read digitised information from the SIROCCO card into a Macintosh PC, and the data were subsequently transferred to the mainframe IBM for software manipulation.

The test procedures are now described in some detail.

4.1.1 The T4 test

The so called T4 test made use of the calibration facility of the multiplex chip whereby charge could be injected along control lines into the front end amplifier of every fourth channel of the detector simultaneously. Channels 1, 5, 9... (the first T4 group) were thus pulsed together, as were channels 2, 6, 10... (the second group), and so on to a total of four T4 groups. The first, second, third and fourth groups were pulsed in turn at the sensitive time in consecutive readout cycles, the S_1-S_2 window which would coincide with BCO in DELPHI (Fig 3.10b). In addition, data were taken during a fifth readout cycle, when no calibration pulses were injected into the system, so that pedestal values for the amplifiers could regularly be updated.

Initial testing of hybrids before connection to silicon plaquettes was carried out to check for correct function of amplifier circuitry. Further testing was carried out after a hybrid had been bonded to two plaquettes to form a half-module. The gain of each amplifier was checked : the distribution of amplified signal magnitudes, measured in arbitrary ADC counts, is shown on a logarithmic scale in

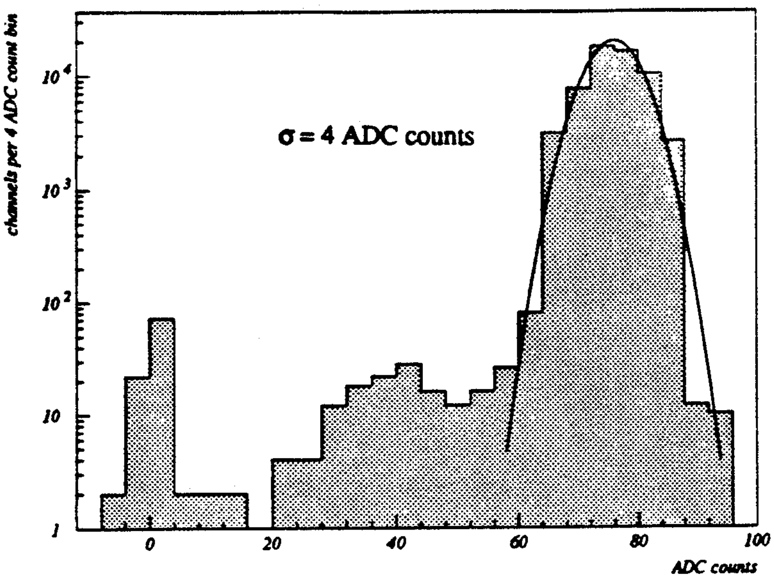

Fig 4.1; Distribution of Microplex amplifier gains in T4 test on a logarithmic scale. A Gaussian fit to the data is also shown.

Fig 4.1. Also shown is a Gaussian fit to the peak, representing the spread of signal amplitudes for the majority of detector channels.

The width of the Gaussian is ≈5% of the mean signal magnitude. Assuming linear charge division between neighbouring channels (equation (3.2)), this corresponds to a contribution to the detector resolution of of 2.5μm (section 4.2.1). It should however be noted that the 5% spread of the data includes a contribution from the spread of the injection capacitance in the calibration lines. 2.5μm represents an upper limit on resolution due to spread in preamplifier gain. Entries outside the peak are discussed in section 4.3.

In addition, T4 testing on half-modules identified any shorts between aluminium readout strips on the silicon plaquettes. If neighbouring readout strips were connected, a signal would have been seen on each of the shorted channels when the preamplifier of the other was pulsed (Fig 4.2). No such shorts were found.

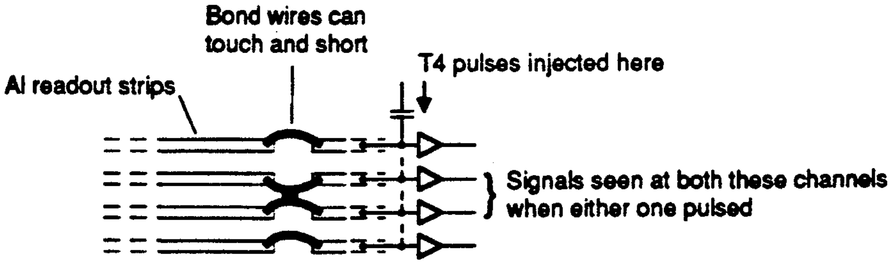

Fig 4.2. T4 testing locates shorted readout strips.

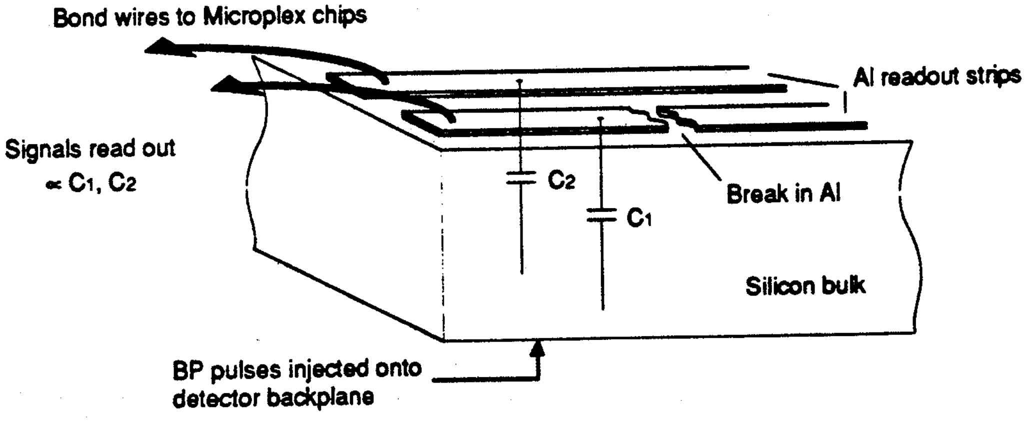

Fig 4.3. BP testing locates broken readout strips.

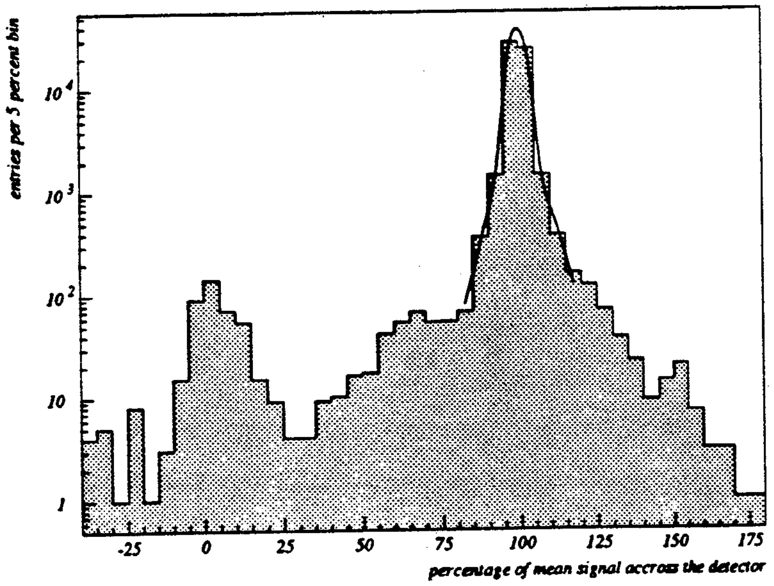

Fig 4.4; **Distribution of signals measured for readout channels in BP test as** percentage of mean signal in a detector.

4.1.2 The BP test

In the BackPlane test, calibration pulses were injected onto the aluminised backplane of silicon detector plaquettes connected to a hybrid. Capacitative coupling across the depletion layer of bulk silicon caused charge to be deposited on every diode of the detector.

The charge integrated by the preamplifier on the multiplex chip for a given channel depended on the diode to readout strip capacitance. In cases where an Al readout strip was broken, the capacitance to the area of aluminium strip on which charge could be detected would be reduced. A reduced signal would therefore be recorded for such channels in the BP test (Fig 4.3).

Fig 4.4 shows the distribution of signals measured in BP test for detector channels. The signals are shown as a percentage of the mean signal recorded across each detector, because varying backplane pulse heights were used in the tests to deposit charge on the detector. The distribution is discussed further in section 4.3.

4.1.3 The LR test

In the LaseR test, laser light was used to simulate the passage of a charged particle through the detector at a precisely known position. Comparison of measured and actual beam coordinates gave a measure of detector performance.

The module or half-module under test was clamped on a moveable table under the control of two micron precise stepper motors acting in orthogonal directions. An optic fibre was arranged so as to transmit laser radiation into one eyepiece of a stationary binocular microscope. Focus could then be achieved by eye through the other eyepiece. When focussed, the laser spot had a diameter of 10±5μm.

In the standard laser test, the laser spot was first positioned centrally between two Al readout strips. Data were taken over a number of readout cycles as the detector was moved perpendicular to the direction of the readout strips, according to some prespecified pattern. The pattern usually involved taking data for three readout cycles at each of five points between the readout strips (Fig 4.5a), but could be varied to give finer detail if required. For each readout cycle, the strips either side of the laser spot were identified as those giving the highest signal amplitudes, and a measure of the charge division between the two strips concerned could be made. Profiles were plotted, showing the distribution of charge between two strips as a function of position of incident particle track between those strips. Typical examples are shown in Fig 4.6, both for the normal case when data were taken at five points between two readout strips, and when more data have been taken for a detailed inspection of the profile. The procedure was repeated twice for each pair of readout strips in every plaquette, under software control (Fig 4.5b).

A useful analytical technique for examining the function of the detector was to reconstruct the positions in the detector of the intermediate p-type regions. Their positions could easily be derived from profiles of charge distribution introduced above. Intermediate diodes were known to be

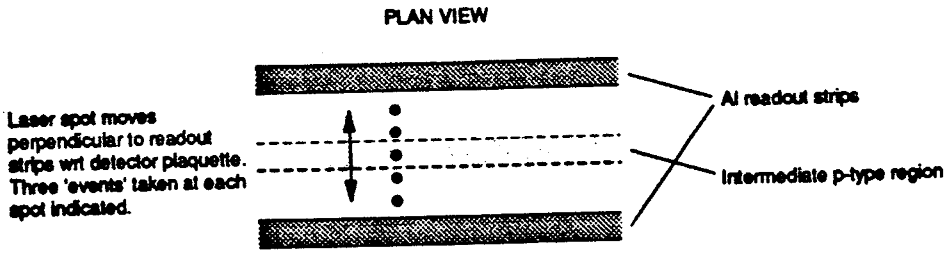

Fig 4.5a; Laser movement between two neighbouring readout strips in LR test.

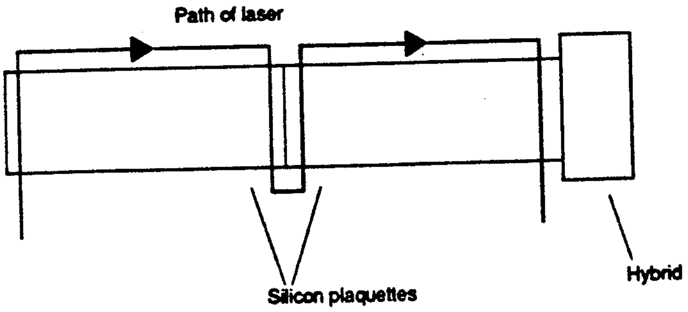

Fig 4.5b; Laser movement across detector structure in LR test.

midway between readout diodes, to within 1μm. It followed that when the charges deposited on two neighbouring strips were equal, the laser should be positioned directly above a p-type region.

A straight line was fitted to the experimental points of the charge division profile. The position of the intermediate diode was then given by the intersection of the fit with the half-maximum signal level (Fig 4.6a). The deviation Δ of the measured intermediate diode position from the known true positions was calculated.

Fig 4.7 shows the distribution of measured values of Δ. The RMS of the fit is 2μm, and less than the design detector resolution of 5μm. The apparent improvement on design specification is due to

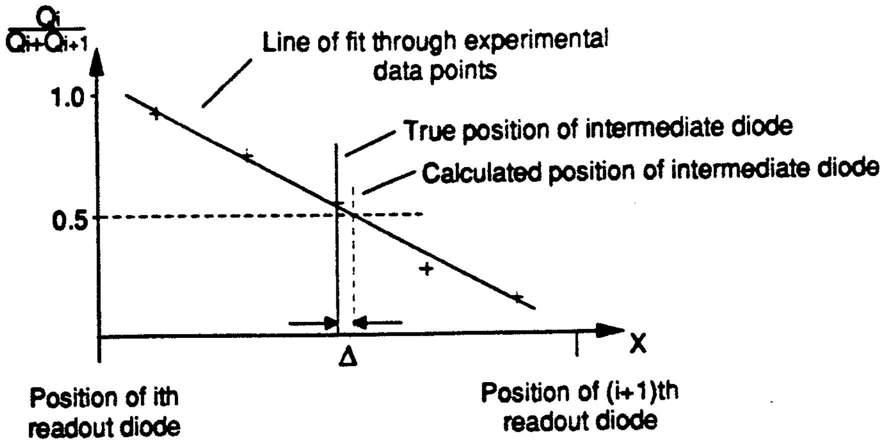

4.6a Typical profile measured in LR test, showing the calculation of Δ.

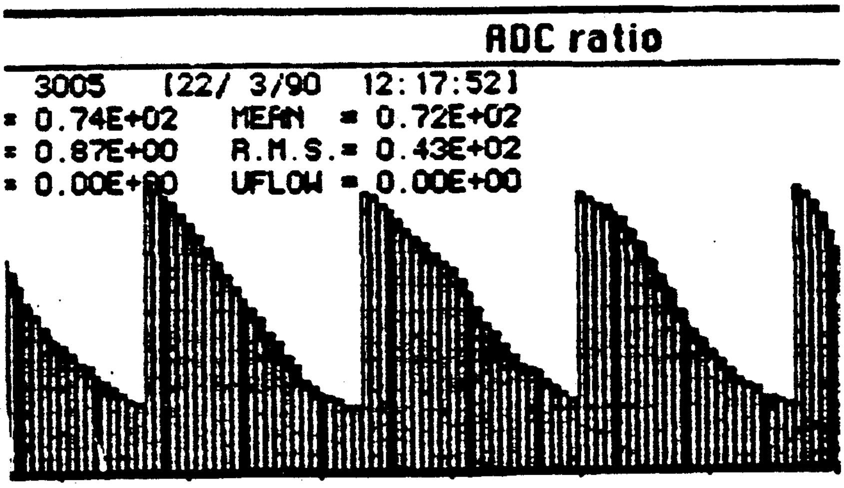

4.6b A detailed study of charge division between two readout strips.

Fig 4.6; Experimental charge division profiles.

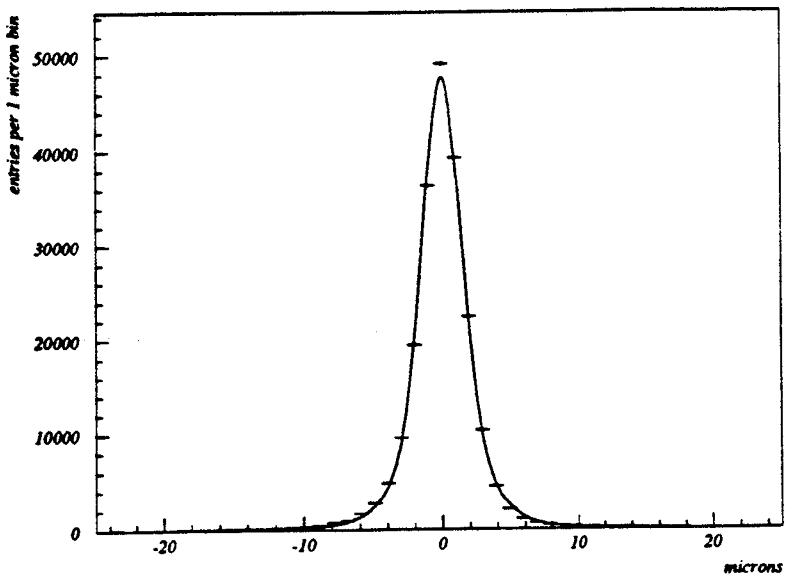

Fig 4.7; Distribution of Δ.

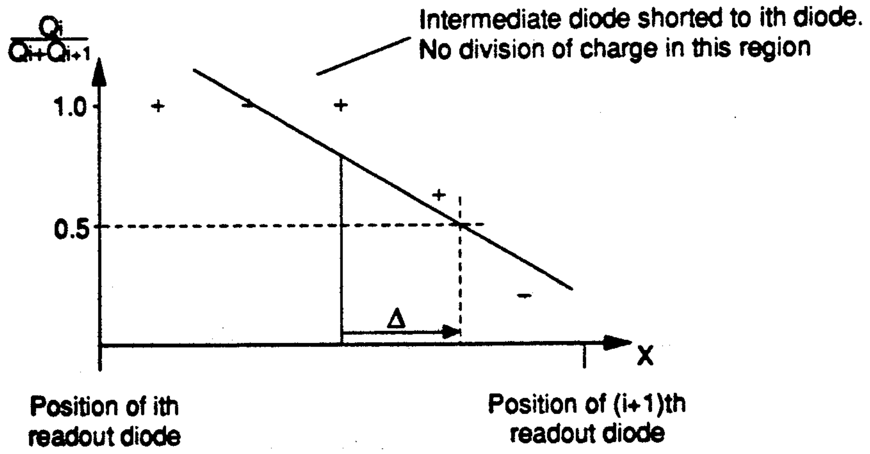

Fig 4.8; Example of a charge division profile for where a readout diode is shorted to an intermediate diode (c.f. Fig 4.6a).

the high ionising strength of the laser spot (signal to noise ratio of 50:1). Detector resolution is discussed in more detail in section 4.2 below.

Charge division studies can yield useful information about possible faults of construction in a detector module. For instance, if there is an electrical short within a silicon plaquette between the p-type region coupled to a readout strip and an intermediate p-type region, the short is reflected in the charge division profile between the surrounding readout strips (Fig 4.8). Anomalously high or low values of Δ should therefore give an indication that a p-type short may have occurred.

LR test results were used in the preparation of the calibration database. Detail of the diagnosis is postponed until section 4.3.

4.2 A model for VD resolution

The resolution of the VD is ultimately limited by the precision with which the integrated charges Q_i deposited on detector channels i are known. An expression for detector resolution δX in the approximation of linear charge division between neighbouring diodes can be obtained by differentiating equation (3.2);

$$\frac{\delta X}{D} = \frac{\delta Q_i}{[Q_i + Q_{i+1}]} \tag{4.1}$$

since the error on D is negligible, and the sum Q_i+Q_{i+1} is independent of where an incident particle passed through the detector, and for minimum ionising particles has the value 27 ADC counts[35].

A major contribution to the variation δQ_i in signal amplitude is noise in the detector, now discussed below. Others are the spread in front end preamplifier gains, discussed in section 4.1.1, and cross-talk between channels in the detector and during readout. There is a small contribution to resolution which must be added to the predictions of equation (4.1) to allow for the fact that charge

Source of limitation on resolution	Limitation (μm)
Spread of Microplex amplifier gains	<2.5
Noise remaining after CMS corrections	3.7
Crosstalk between channels	2.5
Deviation from linear charge division behaviour	small
Quadratic sum gives detector resolution	5.1

Fig 4.9; Contributions to VD resolution.

division profiles such as that shown in Fig 4.6b are not in practice straight lines (i.e. that linear charge division is an approximation). Contributions to detector resolution are tabulated in Fig 4.9.

4.2.1 Noise considerations

The analogue output from the VD arriving at the flash ADCs is subject to noise variation from two main sources. Common mode noise generated when electromagnetic pickup causes the voltages on all the readout strips in a plaquette to vary together, can largely be eliminated by software running in the SIROCCO microprocessor. Noise generated in the front end amplifiers can not be compensated for, and remains as the dominant component.

The double correlated sampling technique used to read charge deposits from the silicon plaquettes into the Microplex chips removes low frequency common mode noise from the data. Remaining common mode noise is dealt with by calculating the mean pedestal over time for each individual readout channel in a detector, and inspecting event by event the overall deviation across all the channels from the time average values. Common mode shift (CMS) corrections to the data, calculated as follows, then compensate for global pedestal shifts due to electromagnetic pickup.

If the time average pedestal values for strips i and pedestals P_i are μ_{Pi}, then the CMS to be added to the digitised information coming from a particular half-module for a particular readout cycle is;

$$CMS = \frac{1}{N}\sum_{i=1}^{N} P_i - \mu_{Pi} \tag{4.2}$$

Then P'_i

$$P'_i = P_i - CMS \tag{4.3}$$

is the CMS corrected signal.

Noise distributions before and after CMS corrections are shown in Fig 4.10. Noise remaining after CMS correction originates either in leakage currents in the silicon plaquettes, or in the front end amplifiers as a function of amplifier input capacitance. Signal noise is typically increased by a factor of two when two silicon plaquettes are electrically connected to hybrids.

The distributions of Fig 4.10 were measured using completed half-modules in the ambient state. Front end amplifiers were therefore connected to two silicon plaquettes, and the input capacitance was the same as it would be within DELPHI. The noise values shown in the distributions are representative of those that should be expected for the detector in the experimental environment.

The limitation on detector resolution due to noise can be estimated by substituting typical noise values from Fig 4.10 (≈2 ADC counts) into equation (4.1). Assuming a total deposited charge on two neighbouring strips of 27 ADC counts (the minimum ionising case), a position resolution contribution δX of 2/27 × 50μm, i.e. of 3.7μm, results. For incident particles which are not minimum ionising, and for the ionising laser described in section 4.1.3, signal to noise ratios are higher, and contributions to position resolution accordingly lower.

From equation (4.1), it is possible to set an upper limit on the noise variation that a particular detector channel exhibits, for that channel to be considered to be useful. The contribution to posi-

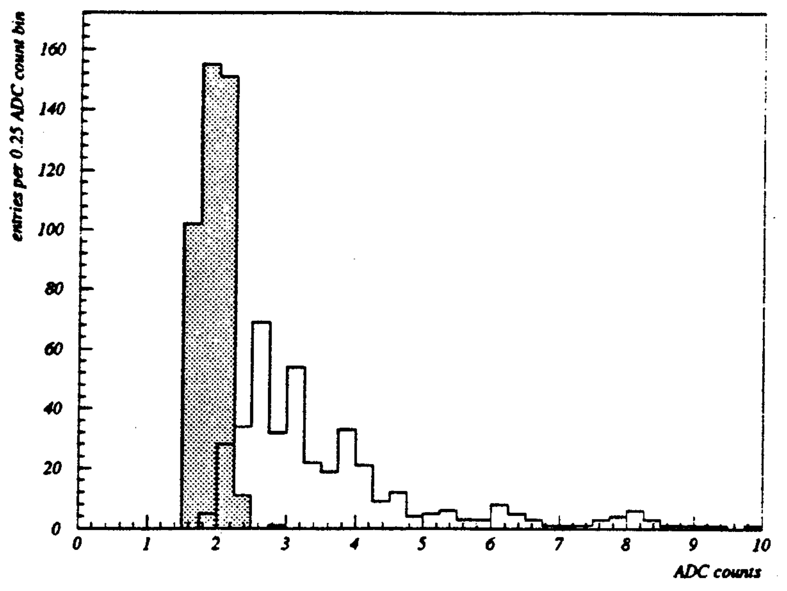

Fig 4.10; Distribution of noise measured in BP test in ADC counts. Hatched (unhatched) after (before) correction for common mode noise.

tion resolution due to noise will be 10μm when the signal to noise ratio drops as low as 5:1. For minimum ionising particles, a signal to noise ratio of 5:1 infers maximum allowed noise of 1/5 × 27 = 5.4 ADC counts. This convenient upper limit on acceptable noise values will become important in section 4.3 below.

4.3 A detector performance database

Calibration data for all subdetectors within DELPHI are stored in a hierarchical data management system. Each subdetector group is responsible for the upkeep of a predetermined set of data fields in a database, which fully describe the position, performance and status of their apparatus at any given time.

For each silicon plaquette in a microvertex detector full module, there is a field in the calibration file in which an error code can be specified for any non-standard channel within that plaquette.

Channels performing within tolerances of design specification are not entered into the database. The agreed error coding convention is

$$\text{code} = (\text{channel} \times 1000) + (\text{badness} \times 100) + \text{Int}(RG \times 50) \tag{4.5}$$

where the channel numbering convention is straightforward and stored elsewhere in the calibration file, the badness number is an identifier for the particular fault being noted in the integer range 0 to 9 and RG is the gain of the channel relative to the mean gain for a channel in that particular multiplex chip. In the unlikely event that $RG > 1.99$, the approximation is here made that $RG = 1.99$.

Badness numbers are allocated according to an order of priority : strips which display symptoms associated with two or more badness numbers are allocated the number corresponding to the fault which more seriously affects local detector resolution. A table of badness numbers and their associated faults is shown Fig 4.11. Details of the envisaged possible faults, and of the observed symptoms associated with them, are now given below in decreasing order of seriousness.

4.3.1 Punchthroughs

During the execution of the test procedures outlined above (section 4.1), it was discovered that in many detector modules, a number of readout strips had become electrically shorted through the insulating silicon dioxide layer to the p-type regions in the silicon directly beneath them. Detector channels displaying this fault became known as punchthrough channels. If during testing the bias voltage supplied to the p-type regions was varied (Fig 3.10a), the signal read out by punchthrough channels varied in direct proportion to the leakage current flowing in the shorted track.

If bias voltages and leakage currents were constant in time, then provided that the pedestal signals read out for punchthough channels were within the normal pedestal range, the detector channels concerned could be used to give position information as normal. However, if leakage currents increased with time or varied as a function of electromagnetic pickup then punchthrough channels could give unreliable or noisy data. It was considered important to note which channels in a

Fault on channel	'Badness number' code for channel in database
Punchthrough	0
No signal	1
Broken bond wires between plaquettes	2
Connected diode region	3,4
Signal magnitudes outside normal range	5
Noisy	6

Fig 4.11; Badness numbers and their associated faults.

module were punchthrough channels, so that the information could be stored in the calibration database.

Punched through channels are easily found by varying the p-type region bias voltage and observing which channels give varying signals, outside of any BP, T4 or LR testing. The channels are allocated badness number 0, and the value of Int(RG × 50) in equation (4.5) is set to 199, the RG value for a punched through channel clearly depending on the chosen operating bias voltage.

Fig 4.12 shows the distribution of number of punchthrough channels recorded in half-modules prior to installation in the DELPHI VD. A total of 894 punchthrough channels were identified. This corresponds to 1.5% of all VD channels.

4.3.2 Dead channels

A detector channel is deemed to be dead in the instance it gives signal amplitudes under test which are statistically inseparable from zero. Figs 4.1 and 4.4 showed the distributions of signal amplitudes for T4 and BP tests respectively. For the present purpose, dead channels are defined to be those which give either less than 5% of the mean amplitude per chip in T4 test, or less than 7.5% mean amplitude per chip in BP test. 0.3% of all VD channels met this criterion, and were allocated

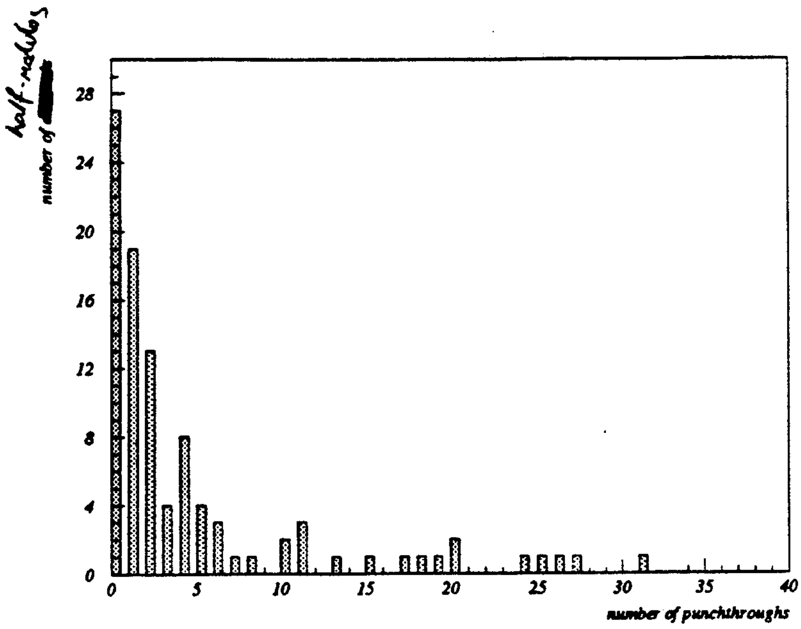

Fig 4.12; Number of punchthrough channels per half-module.

badness number 1. Fig 4.13 shows the distribution of number of dead channels per VD half-module.

4.3.3 Broken bond wires

A half-module is composed of two plaquettes of silicon, whose readout strips are connected with bond wire (section 3.3.1). If the bond wire is broken, the backplane to readout strip capacitance will be halved for the channel concerned, and approximately half height BP signals will be observed. In addition, a lack of signal from a particular channel in a LR test when the laser is directed at the plaquette farthest from the hybrid is indicative of a broken bond wire.

Values of Δ displaced by more that 3σ from the mean of the Δ distribution for the far plaquette, combined with BP signals within 15% of half the mean signal for a given Microplex chip, were

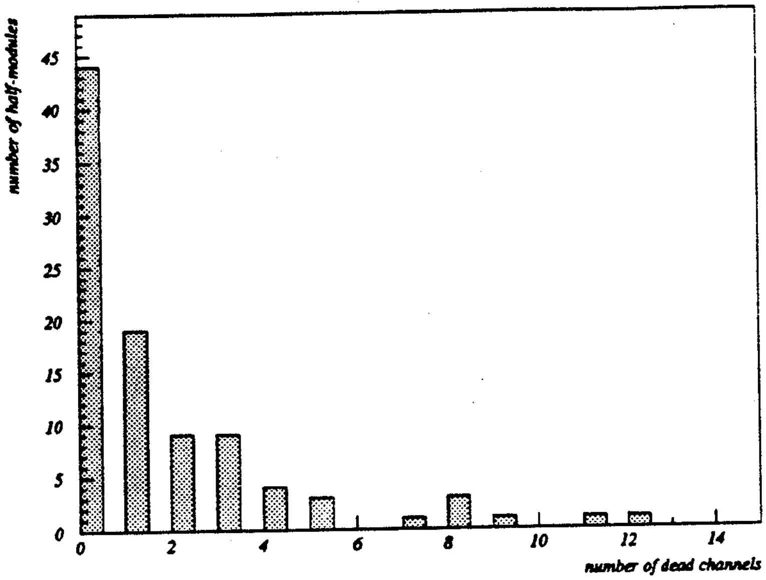

Fig 4.13; Number of dead channels per half-module.

taken to infer a possible broken bond wire. Less than 0.1% of all VD channels were diagnosed to have this problem, and were allocated badness number 2.

4.3.4 Connected diodes

Shorts between p-type regions in the silicon plaquettes can result in anomalous values for Δ (section 4.1.3). Δ values more than 3σ from the mean of the Δ distribution, in the absence of any correlated half height BP signal information, were taken to indicate such possible shorted diodes. Only 8 pairs of possible shorted diodes were found in test on all half-modules to be installed in DELPHI.

It is possible to infer from the sign of the anomalous Δ value for a given intermediate p-type region to which of its neighbouring readout p-type regions it is shorted (Fig 4.8). In the calibration database, the channel corresponding to the neighbouring readout strip which is not shorted is allocated badness number 3, and the shorted neighbouring readout strip is allocated badness number 4. In this way the region of the detector with reduced position resolution is precisely defined.

4.3.5 Other anomalous signal magnitudes

Channels which gave abnormal signal amplitudes in T4 or BP testing were allocated badness number 5. In this context, abnormal signals were defined to be those outside 15% and 30% of the mean per Microplex chip concerned, for T4 and BP testing respectively (see Figs 4.1 and 4.4).

Fig 4.14 shows the distribution of number of channels giving anomalous signals per half-module. 1% of channels of all VD channels fall into this category.

4.3.6 Noisy in lab test

Any remaining channels which registered noise values after correction for CMS of greater than 5.4 ADC counts were allocated badness number 6. 5.4 ADC counts represents the maximum allowed noise for position resolution to minimum ionising particles to be better than 10μm (section 4.2.1).

Fig 4.15 shows the distribution of number of noisy channels measured per half-module. 1.6% of all VD channels were flagged as noisy channels.

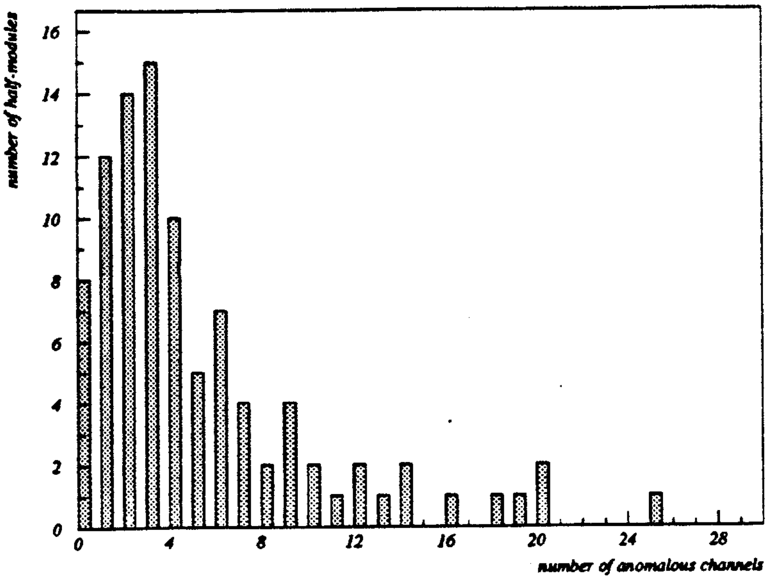

Fig 4.14; Number of channels per half-module giving signals outside the normal range in testing.

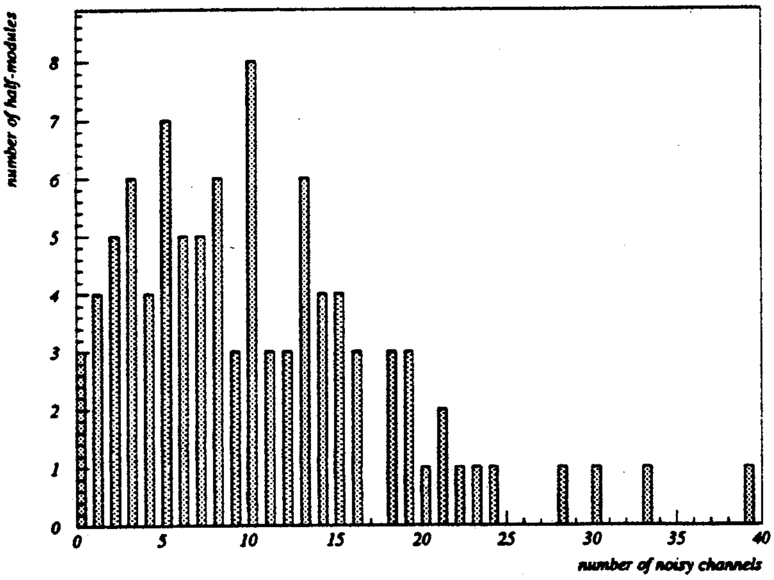

Fig 4.15; Number of noisy channels per half-module.

Chapter 5. The selection of a τ event sample

Before a measurement of the τ lifetime can be made, events in which τ leptons have participated must be isolated from those in which τs have not. The τ is shortlived, travelling on average a distance of only 2.4mm within DELPHI, and event selection must be based upon the observation of its charged decay products. The Standard Model makes predictions as to how the charged decay products of the τ are topologically and kinematically distributed. The principle of event selection is based upon finding ways in which the topological and kinematic distributions of τ decay products differ from those of particles from other event classes.

This chapter contains the detail of how a sample of $\tau^+\tau^-$ events has been selected from the data taken in the barrel region of DELPHI during 1990. At the time when the analysis began, DELPHI endcap regions were not fully operational, and they play no part in this analysis. Section 5.1 outlines general considerations, and discusses potential sources of background, where non-τ events may exhibit certain features similar to those of the τ signal. Section 5.2 introduces topological cuts used on the data, where for example a suitable choice of maximum permitted number of tracks in an event can be made, to differentiate between wanted and unwanted event classes. Section 5.3.1 contains information on how calorimetry has been used to minimise dielectron contamination in the event sample, and 5.3.2, details the use of the muon chambers in rejecting dimuon events. Finally, in 5.5 the τ data sample is critically examined, and the statistics of the τ events used in the lifetime measurement of Chapter 6 are presented.

5.1 General

The τ lepton has a variety of decay modes open to it (Fig 1.4). However, in the vast majority of cases, the decay products comprise neutrals with only one, or alternatively three, accompanying charged particles. Clearly, in the reaction

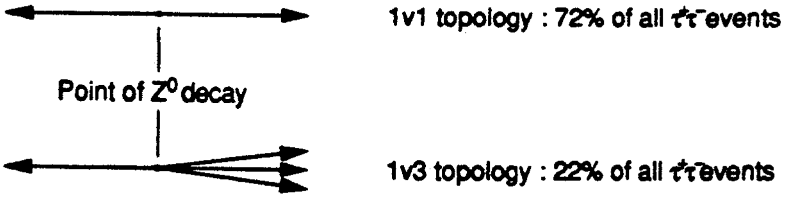

Fig 5.1; Topologies of $\tau^+\tau^-$ events.

$$Z^0 \rightarrow \tau^+\tau^- \rightarrow \text{anything} \tag{5.1}$$

the visible event signature will usually be charged tracks in a topology of 1v1 or 1v3, where the notation XvY describes a topology where there are X charged tracks in one hemisphere of the event, and Y changed tracks in the other (Fig 5.1). This is in strong contrast with quark-antiquark events

$$Z^0 \rightarrow q\bar{q} \rightarrow 2 \text{ or more jets of particles} \tag{5.2}$$

where topologies of large numbers of tracks are not uncommon. It is necessary only to require of an event that the number of tracks is low, in order to reject a large proportion of the potential $q\bar{q}$ background.

The lifetime of the muon is long ($\approx 10^{-6}$ sec) and the electron is stable, so that events of the type

$$\begin{aligned} Z^0 &\rightarrow \mu^+\mu^- \\ Z^0 &\rightarrow e^+e^- \end{aligned} \tag{5.3}$$

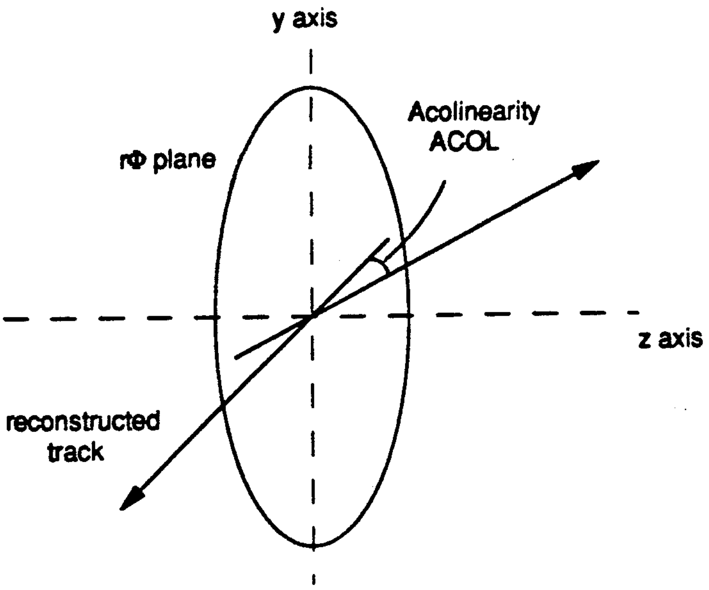

Fig 5.2; Definition of acollinearity.

provide in principle only the topology 1v1. The relative branching ratios of the Z^0 into $\tau^+\tau^-$, $\mu^+\mu^-$ and e^+e^- are, according to current results, equal : an event selection based solely upon the constraints considered so far would not distinguish between $\tau^+\tau^-$, $\mu^+\mu^-$ and e^+e^- events. In order to separate the three event classes, criteria must be found by which muons and electrons travelling through DELPHI at energies close to 45 GeV will be reliably identifiable.

Experience has shown that the acollinearity in $\mu^+\mu^-$ events is very low (Fig 5.2). Muons are minimum ionising at LEP energies, and generally pass without interacting through the iron return yoke of the superconducting electromagnet. They consequently give hits in the muon chambers MUB and MUF. Electron tracks can be identified by a large deposition in the electromagnetic calorimeter HPC is high.

$\tau^+\tau^-$ events are selected firstly by track counting, and secondly by rejecting specifically the remaining predominant dielectron and dimuon backgrounds. The following sections contain detailed information as to exactly how these general principles for the selection of τ events have been put into practice at DELPHI.

5.2 Selection by event topology

In order to classify an event according to its topology, certain definitions are needed. In assigning an XvY label to an event, care must be taken only to count charged tracks from τ decay, and not tracks for example from $\tau \rightarrow \pi^0 + (...) \rightarrow e^+e^- + (...)$. A 'good track' is therefore defined by a cut on its distance d_0 of closest approach to the origin in the $r\phi$ plane (its impact parameter - Fig 5.3), and its z coordinate z_0 at the point of closest approach. Fig 5.4 shows the distributions of d_0 and z_0, for all charged tracks from the initial data set, comprising all events containing up to 8 charged tracks in total. Also shown are equivalent distributions for simulated $Z^0 \rightarrow \tau^+\tau^-$ event data. Suitable requirements on d_0 and z_0 for a track to be deemed good are chosen;

$$\begin{gathered} d_0 < 1 \text{ cm} \\ |z_0| < 5 \text{ cm} \\ 43^\circ < \theta < 137^\circ \end{gathered} \tag{5.4}$$

(where the θ cut restricts the analysis to the DELPHI barrel region - see above). Fig 5.5 shows the momentum distribution for tracks in the real data isolated by cuts (5.4), and that for equivalent tracks in τ simulation data. Clearly more tracks with low momentum are present in the data than would be expected for τ events. The tracks are thought to come from beam gas interactions, where off-momentum beam particles have scattered in the beampipe wall into the inner tracking chambers. An additional momentum requirement is then imposed before a track is deemed good, namely that all good tracks should have momentum greater than 0.5 Gev, and that at least one per event should have momentum greater than 2.0 GeV. These cuts are found to reduce beam gas background considerably, whilst lowering only slightly efficiency for τ event selection. The number of tracks per

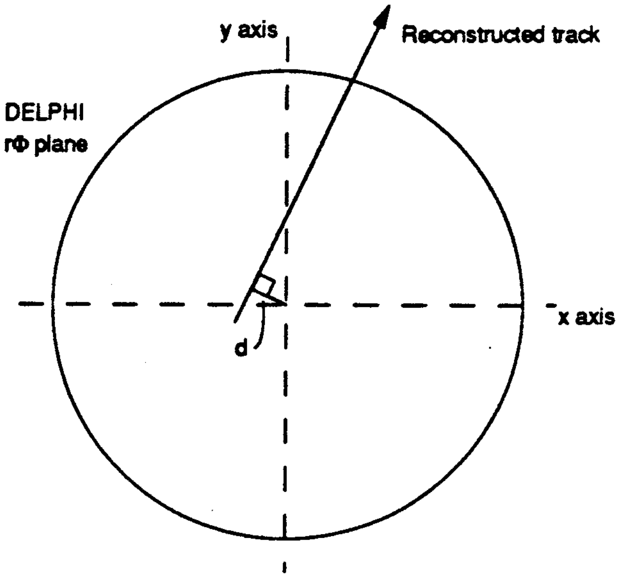

Fig 5.3; Definition of impact parameter.

event passing cuts (5.4) and meeting these momentum requirements is denoted NGDTR. An event is only accepted as a $\tau^+\tau^-$ candidate for further study if

$$2 \leq \text{NGDTR} \leq 6 \tag{5.5}$$

It is useful in the separation of $\tau^+\tau^-$ events from $q\bar{q}$ events to consider the maximum isolation angle in the event, ISOL. ISOL is the angle in space between the most isolated good track in the event and its nearest good track neighbour. Fig 5.6 shows the distribution of ISOL for real data events, for τ simulated data and for $q\bar{q}$ simulated data. As expected, τ events usually fall into a 1vN category (N = 1,2 .. 5), having one good track separated from the rest by a large space angle. $q\bar{q}$ events are unlikely to contain one good track well separated from the rest. A cut on maximum isolation angle is imposed;

$$\text{ISOL} \geq 160° \tag{5.6}$$

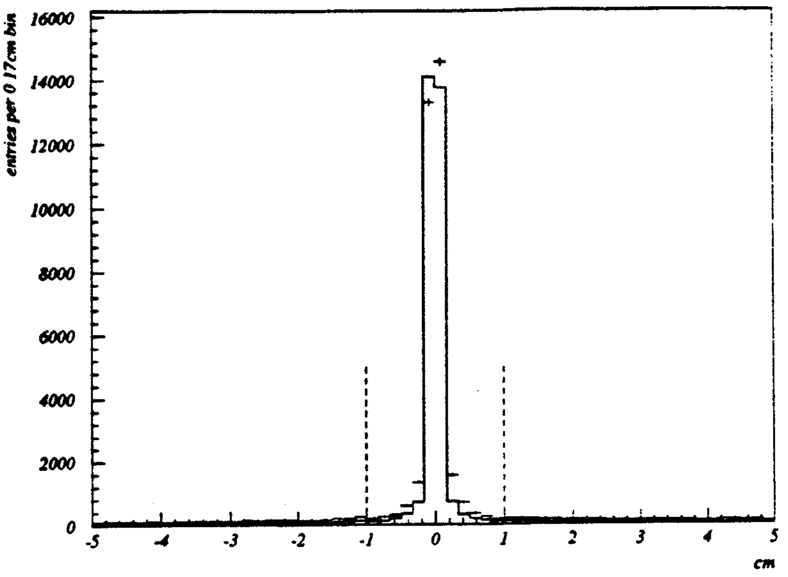

Fig 5.4a; Distribution of track impact parameters for real data (points) and for $\tau^+\tau^-$ event simulation (solid line).

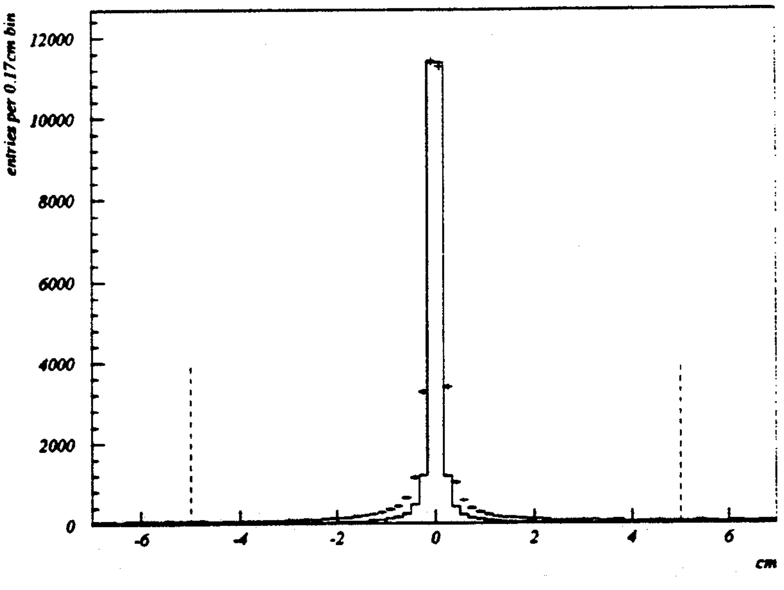

Fig 5.4b; Distribution of track z coordinates at point of closest approach in rϕ, for real data (points) and for $\tau^+\tau^-$ event simulation (solid line).

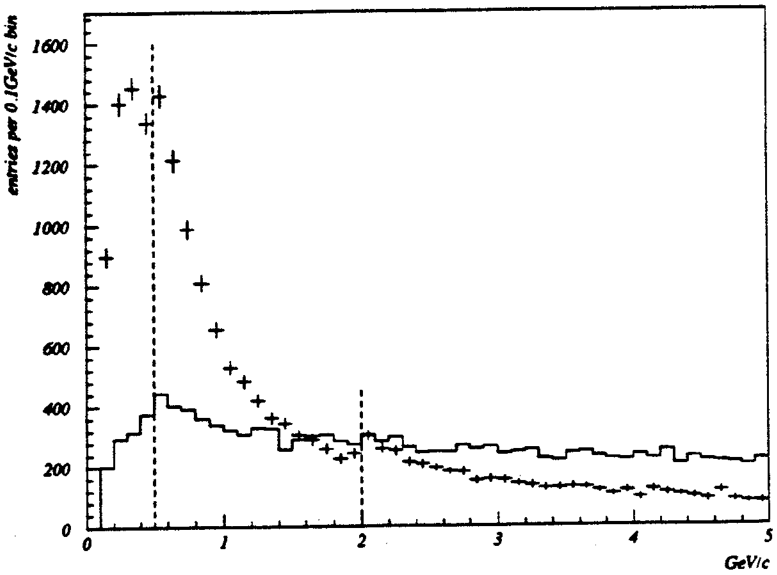

Fig 5.5; Momentum distribution for tracks after cuts (5.4), for real data (points) and for $\tau^+\tau^-$ event simulation (solid line).

to reject low multiplicity $q\bar{q}$ events.

It is also useful to consider tracks other than good tracks in the event. For instance, it is unlikely that more than one π^0 or γ from τ decay would convert in the material of the detector in any one event, and so to have more than NGDTR + 2 tracks in total should similarly be unlikely. The total number of tracks NTOT is therefore evaluated at this stage, with the momentum cut and θ cuts removed, and the vertex cuts relaxed;

$$\begin{aligned} d_0 &< 8\ \text{cm} \\ |z_0| &< 10\ \text{cm} \end{aligned} \tag{5.7}$$

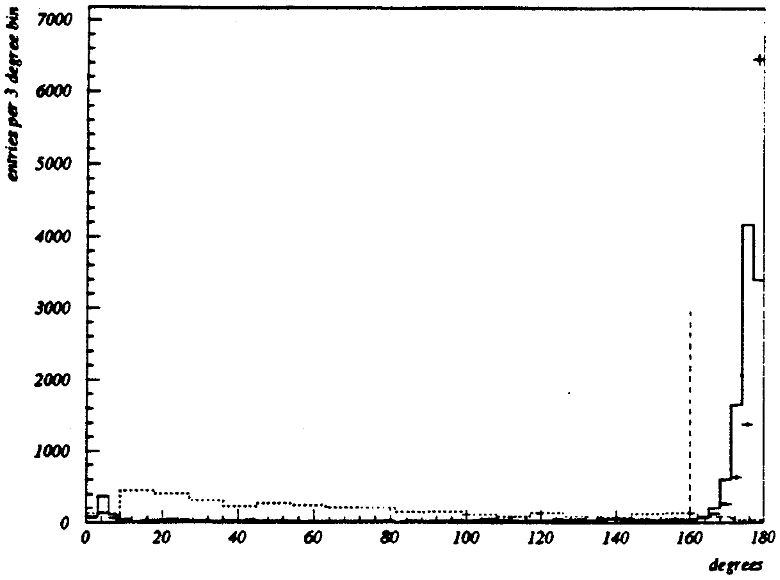

Fig 5.6; Distribution of isolation angle ISOL, in events from real data (points), $\tau^+\tau^-$ events (solid line), and $q\bar{q}$ events (dashed line).

5.3 Rejection of dilepton background

5.3.1 Dielectron events

Electrons are characterised in DELPHI by large energy deposits in the HPC. A simple summation of all energy deposits within a suitably chosen angle around the point where a given track intersects the HPC gives a quantity useful in identifying electron tracks.

Fig 5.7a shows the difference in ϕ coordinate between a given track and all HPC deposits in an event, for all good tracks in the event, for real events which have passed the topological cuts of section 5.2. Each entry in the histogram has been weighted by the energy of the HPC energy deposit concerned. In this way electron deposits dominate in the plot over the small minimum ionising deposits of muon and pion tracks. Figs 5.7b and 5.7c show the equivalent plots for τ event simulation and for dielectron simulation, while Figs 5.8 show the related θ coordinate information. From the plots, it is apparent that 45 GeV electrons tend to deposit their energy very near to their

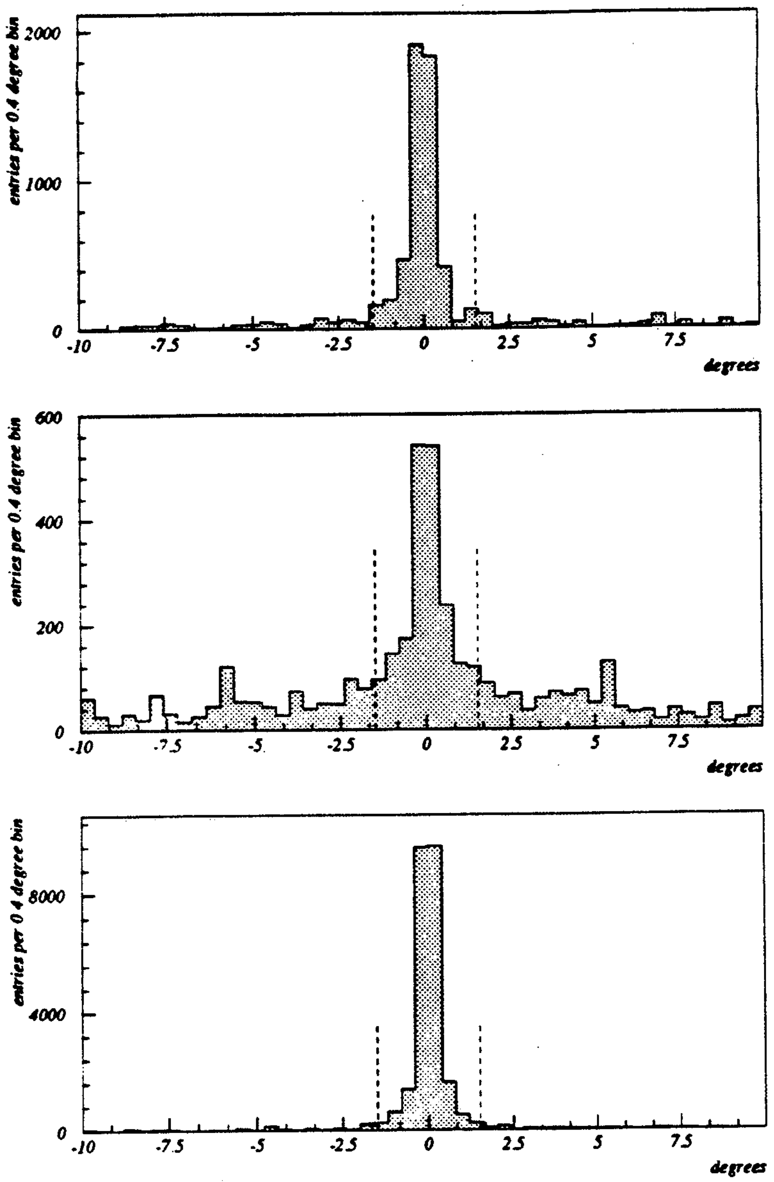

Fig 5.7; Association of HPC energy deposits to tracks in φ. Difference in φ coordinate between the two for **5.7a (top)** real data, **5.7b (middle)** $\tau^+\tau^-$ simulation and **5.7c (bottom)** e^+e^- simulation.

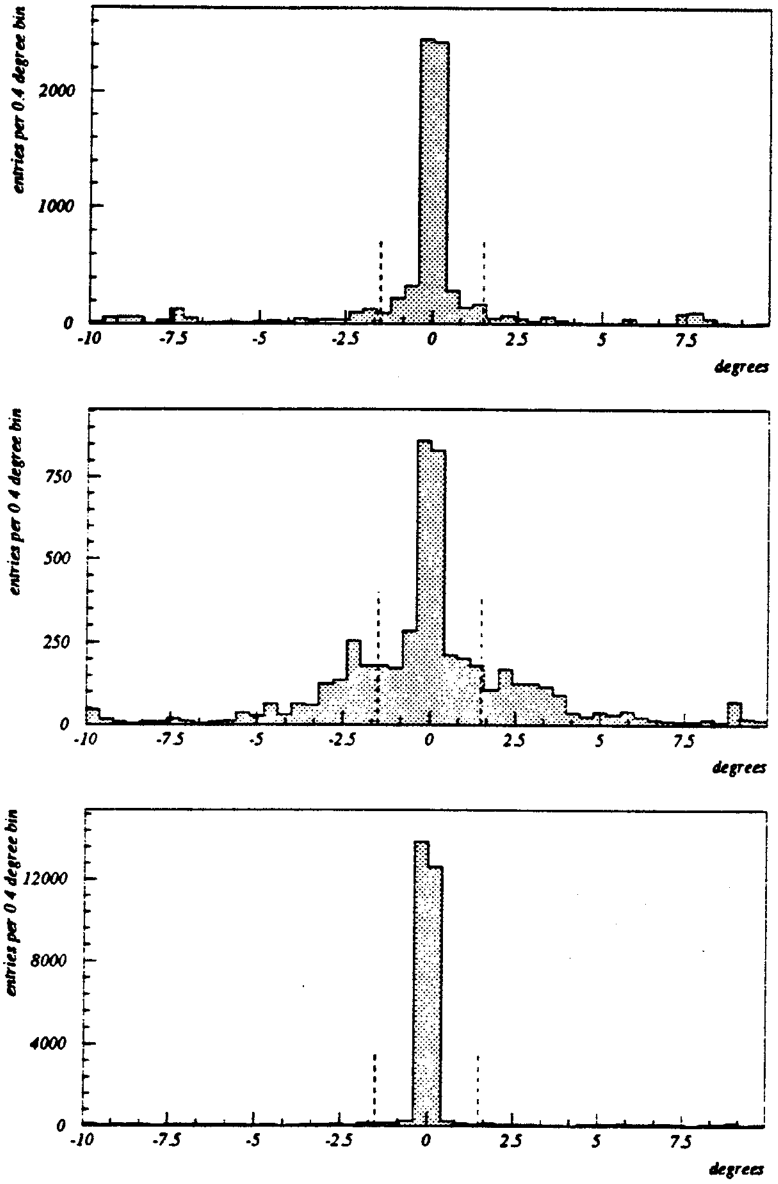

Fig 5.8; **Association of HPC energy deposits to tracks in θ.** Difference in θ coordinate between the two for **5.8a (top)** real data, **5.8b (middle)** $\tau^+\tau^-$ simulation and **5.8c (bottom)** e^+e^- simulation.

own path, where lower momentum tracks from τ decay may appear to leave deposits further away. However, the premise for dielectron identification is that electrons leave large amounts of energy in the HPC. It is therefore no disadvantage to sum energy within a tight angle cone around any track, as only tracks from τ decay may have their energy underestimated.

The energy deposition of all good tracks in the HPC is summed within an angle cut of 1.5° in ϕ about the track extrapolation to the HPC. A cut in θ of 1.5° is similarly chosen, within which to associate HPC energy to a track. The greater of the two associated HPC energies in a 1v1 event is denoted $\mathrm{EHPC}_{\mathrm{max}}$, and the lesser $\mathrm{EHPC}_{\mathrm{min}}$. In the calculation of $\mathrm{EHPC}_{\mathrm{max}}$ and $\mathrm{EHPC}_{\mathrm{min}}$, account must be taken of the fact that electrons frequently radiate a hard photon as they move through the detector. Hence, in an event of 1v2 topology, where for instance a fourth track has been lost, energy on the side of the two prong is summed from both tracks.

Fig 5.9 shows distributions of the HPC energies $\mathrm{EHPC}_{\mathrm{max}}$ and $\mathrm{EHPC}_{\mathrm{min}}$ for good tracks from real data events, $\tau^+\tau^-$ simulation events and e^+e^- simulation events. Events are initially rejected from the real data $\tau^+\tau^-$ sample as dielectron candidates if

$$\mathrm{EHPC}_{\mathrm{max}} > 25\ \mathrm{GeV}\ \text{and}\ \mathrm{EHPC}_{\mathrm{min}} > 10\ \mathrm{GeV} \tag{5.8}$$

Care must be taken, however, to cater for tracks which have passed through inefficient regions of the HPC. The HPC is of modular construction (section 2.3.1), and a considerable fraction of tracks (≈15%) will travel along or close to a module boundary (Fig 5.10). The number of good tracks which have passed within 1° of a module boundary in either θ or ϕ NCRTR is counted, and if NCRTR = NGDTR the event is rejected from consideration for the $\tau^+\tau^-$ event sample as having insufficient HPC information. If $0 < \mathrm{NCRTR} < \mathrm{NGDTR}$, the condition on $\mathrm{EHPC}_{\mathrm{min}}$ is relaxed and the event is taken to be a dielectron if both $\mathrm{EHPC}_{\mathrm{max}} > 25\mathrm{GeV}$ and there are NCRTR tracks in cracks on the side of $\mathrm{EHPC}_{\mathrm{min}}$.

5.3.2 Dimuon events

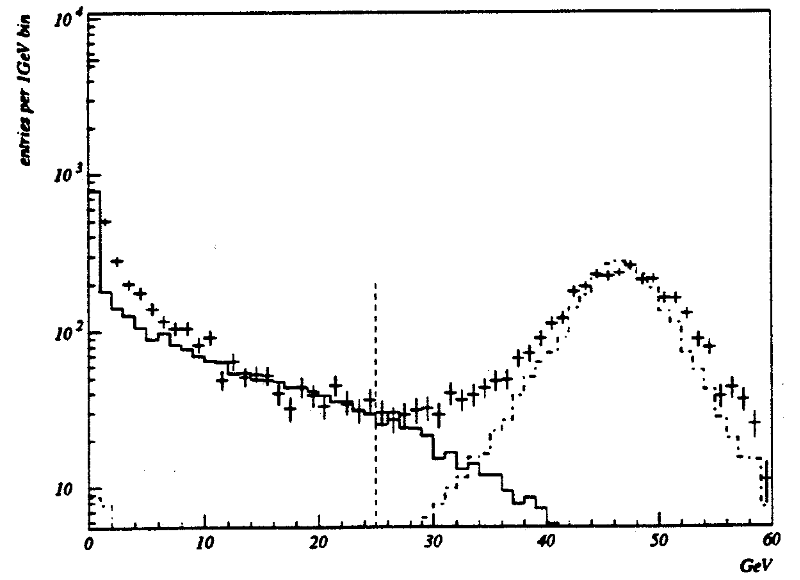

Fig 5.9a; Distribution of energy E_{max}, for events in real data (points), $\tau^+\tau^-$ simulation (solid line) and e^+e^- simulation (dashed line).

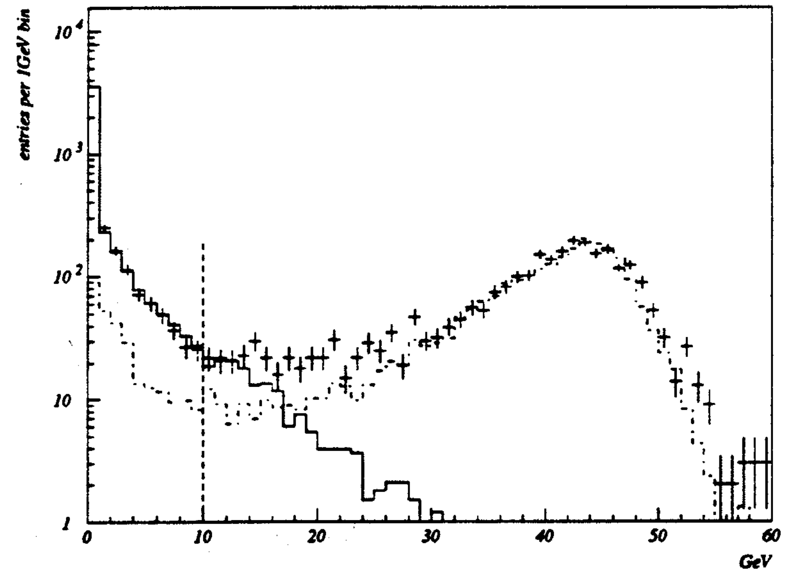

Fig 5.9b; Distribution of energy E_{min}, for events in real data (points), $\tau^+\tau^-$ simulation (solid line) and e^+e^- simulation (dashed line).

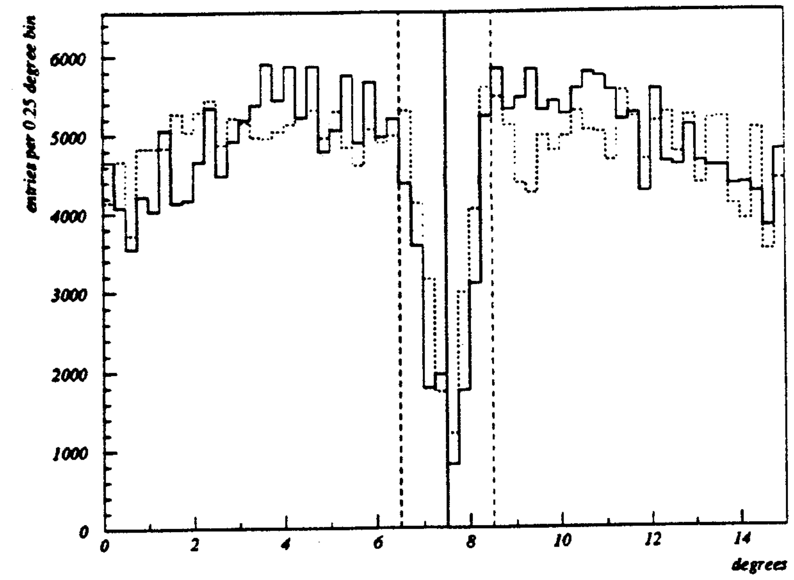

5.10a; ϕ coordinate within a module weighted by energy deposition.

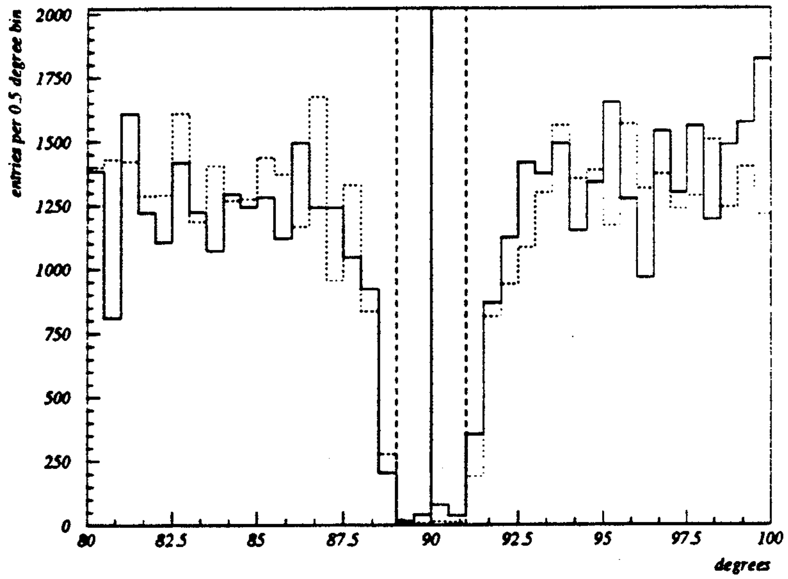

5.10b; θ coordinate within a module weighted by energy deposition.

Fig 5.10; Energy deposition as a function of position within an HPC module, for real data (solid line) and e^+e^- simulation (dashed line). The troughs show inefficient detector regions.

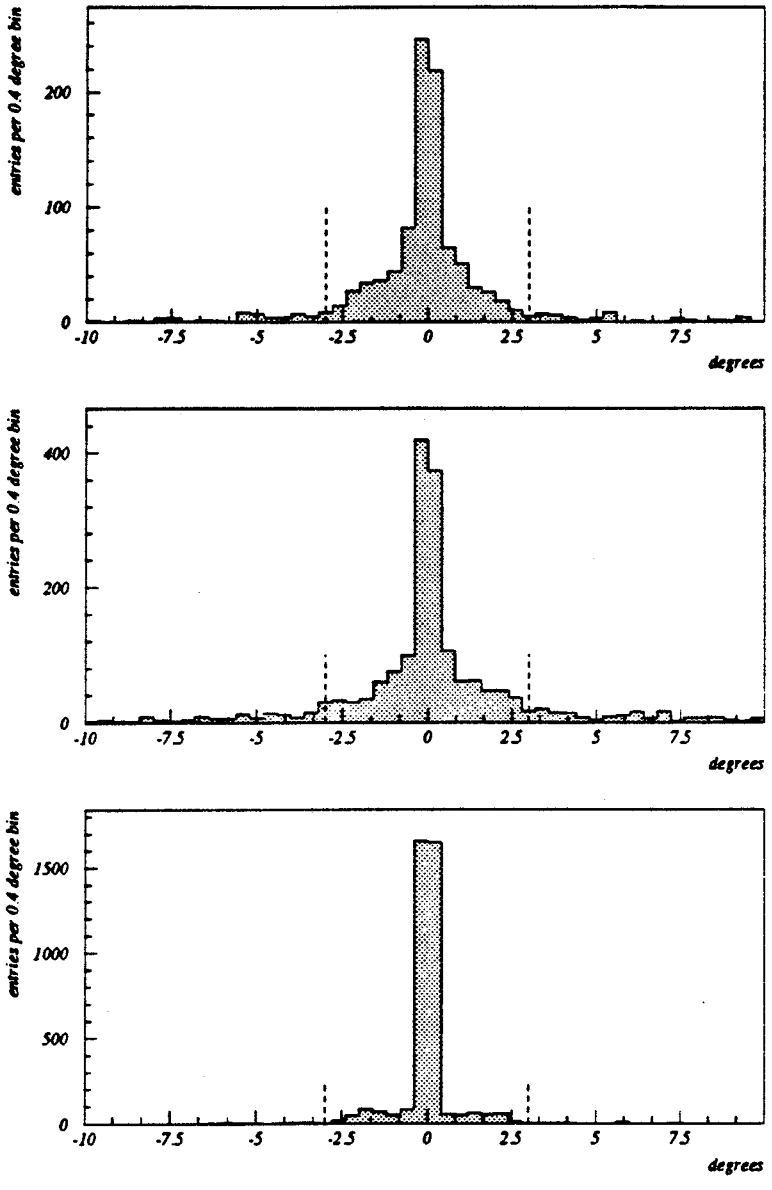

Fig 5.11; Association of MUB hits to tracks in ϕ. Difference in ϕ coordinate between the two for **5.11a (top)** real data, **5.11b (middle)** $\tau^+\tau^-$ simulation and **5.11c (bottom)** $\mu^+\mu^-$ simulation.

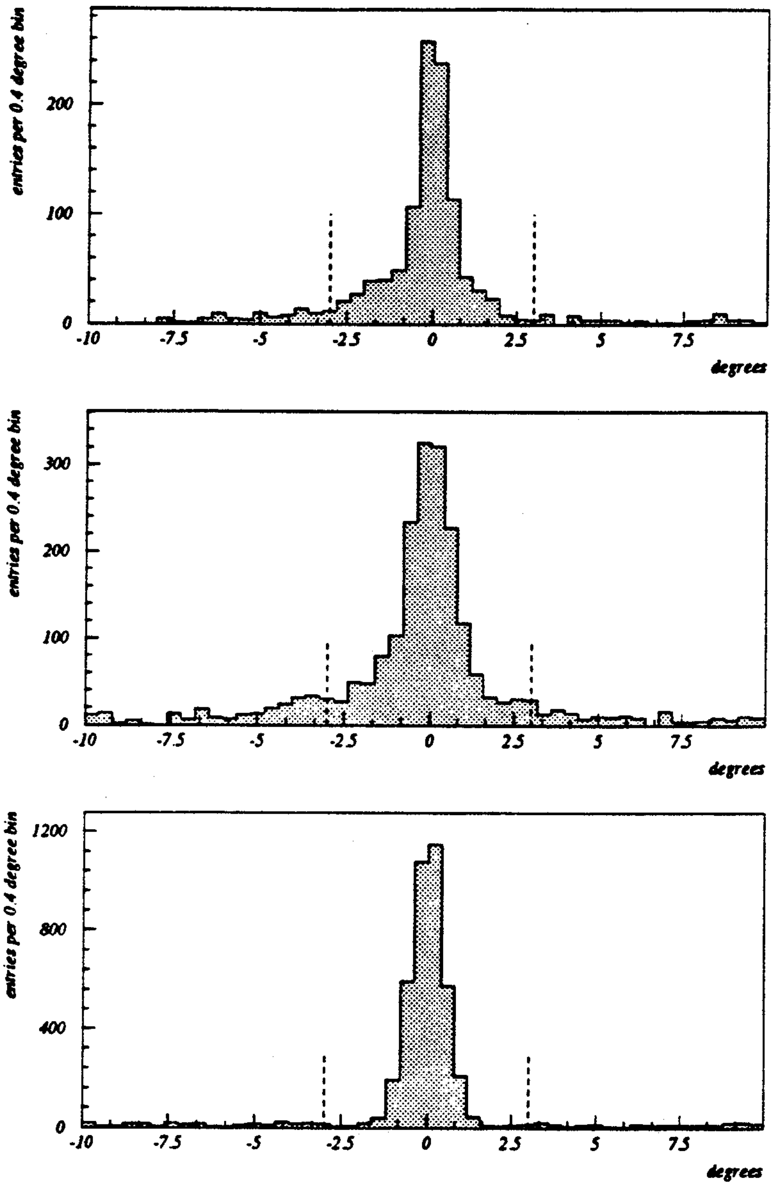

Fig 5.12; Association of MUB hits to tracks in θ. Difference in θ coordinate between the two for **5.12a (top)** real data, **5.12b (middle)** $\tau^+\tau^-$ simulation and **5.12c (bottom)** $\mu^+\mu^-$ simulation.

Peripheral to DELPHI there are three overlapping layers of purpose built wire chambers for detecting muons (the MUB - see section 2.4.1). Hits in the muon chambers can be associated to good tracks by a simple angle cut about the track extrapolation to the MUB, just as HPC energy deposits are associated with tracks (section 5.3.1). Figs 5.11 and 5.12 show the ϕ and θ differences between track coordinates at the MUB and every MUB hit in the event, for good tracks from real, $\tau^+\tau^-$ and $\mu^+\mu^-$ simulation event data. It is appropriate to count muon chamber hits within angular cuts of 3° in both θ and ϕ of the track extrapolation, in order to judge whether or not the track might be due to the passage of a muon[3].

Muons in $\mu^+\mu^-$ events rarely radiate photons as they travel through the detector, and only very occasionally result in any topology other than 1v1. For good tracks coming from events with a 1v1 topology, the relative occurrences of ≥ 1 MUB hit being associated with each track, and that condition not being met, can be seen in Fig 5.13. Clearly, simply making the requirement that both good tracks in a 1v1 event are associated to hits in the MUB will select a large proportion of dimuon events, and only falsely reject a few τ events from the sample. Those tracks in 1v1 $\tau^+\tau^-$ events which do result in MUB hits are likely to be due either to pions which have passed through the detector material along their path without interacting or decaying, or to muons from τ decay. In either instance the momentum of the τ decay product is likely to be less than that of a muon from Z^0 decay. Fig 5.14 shows the distribution of minimum good track momentum in the event, for 1v1 events which result in MUB hits on both sides, for real data, and for $\mu^+\mu^-$ and $\tau^+\tau^-$ simulated data. In order to eliminate as many muon events as possible from the τ sample, and at the expense of losing a few τ events, events are tagged as possible dimuons if both good tracks give MUB hits and have momentum greater than 15 GeV.

---

[3] In fact, hits in the forward muon chambers MUF are also included in the sum if they are within 3° of the MUF track extrapolation. The MUF chambers extend up to 43° in θ and hence are here useful where low momentum tracks are concerned.

Data sample	**Percentage of events with MUB hits**	
	both sides	not both sides
real data	27	73
tau event simulation	5	95
dimuon event simulation	82	18

Fig 5.13. Showing likelihoods that 1v1 events from various classes will produce MUB hits in both event hemispheres.

5.4 Rejection of other backgrounds

After the application of the cuts outlined in the preceding sections, a data sample containing largely τ events remains. However, final comparisons between expected and observed topological distributions at this stage suggest the presence of low-level backgrounds which can easily be cut out.

Figs 5.15 show the final distributions of total number of tracks NTOT in events from real, τ simulation and $q\bar{q}$ simulation data. A cut is imposed to eliminate $q\bar{q}$ background from 1vN topology events when NGDTR>2;

$$\mathrm{NTOT} \leq 6 \qquad (5.9)$$

Additional conditions are imposed on momentum and event acollinearity ACOL that if NGDTR=2 (i.e. for 1v1 topology only),

$$\begin{array}{c} \mathrm{ACOL} > 1^\circ \\ \text{at least 1 good track with momentum} < 30\ \mathrm{GeV} \end{array} \qquad (5.10)$$

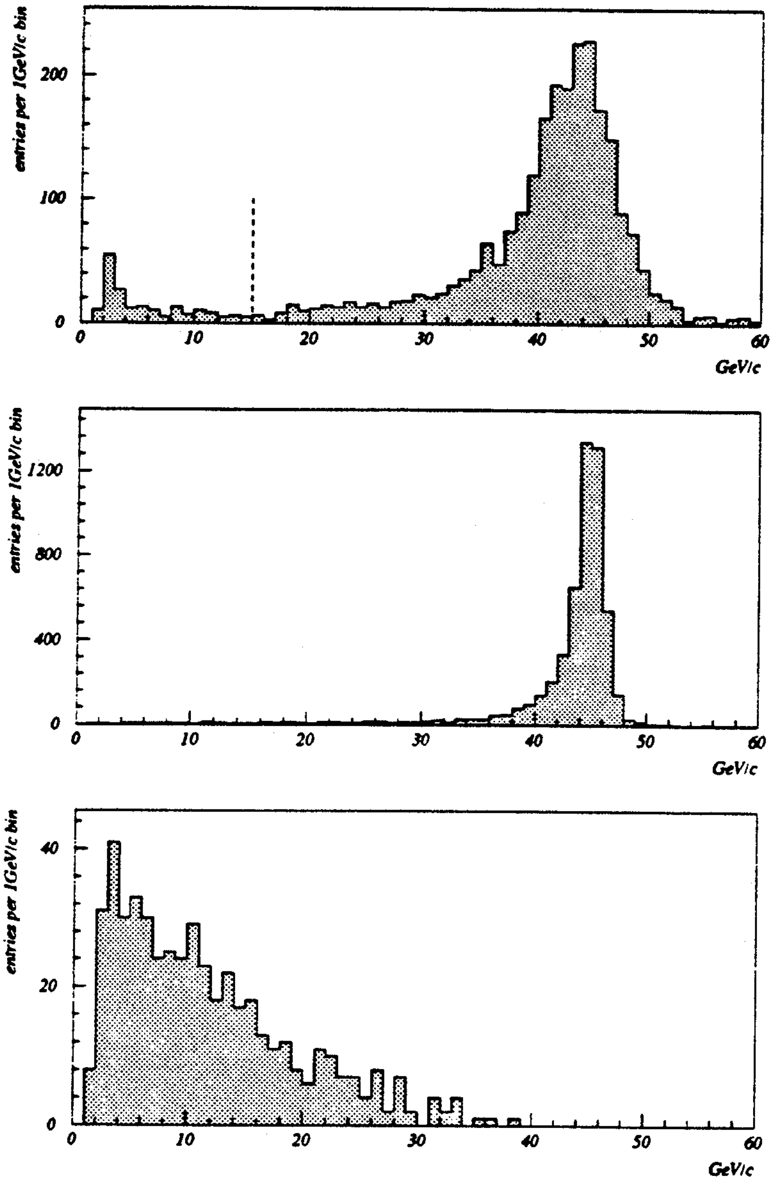

Fig 5.14; Minimum good track momentum in 1v1 events with MUB hits in both event hemispheres, for **5.14a (top)** real data, **5.14b (middle)** $\mu^+\mu^-$ simulation and **5.14c (bottom)** $\tau^+\tau^-$ simulation.

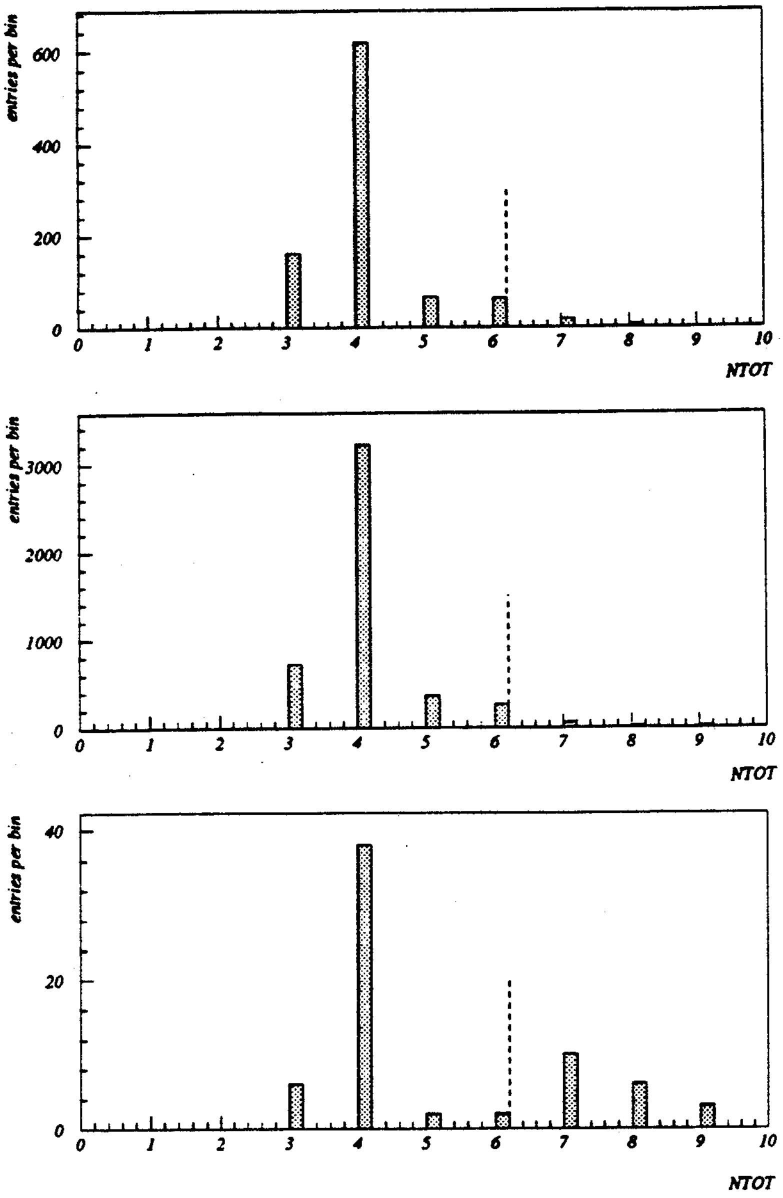

Fig 5.15; **Distributions of number of tracks NTOT, for 5.15a (top) real data, 5.15b (middle) $\tau^+\tau^-$ simulation and 5.15c (bottom) $q\bar{q}$ simulation.**

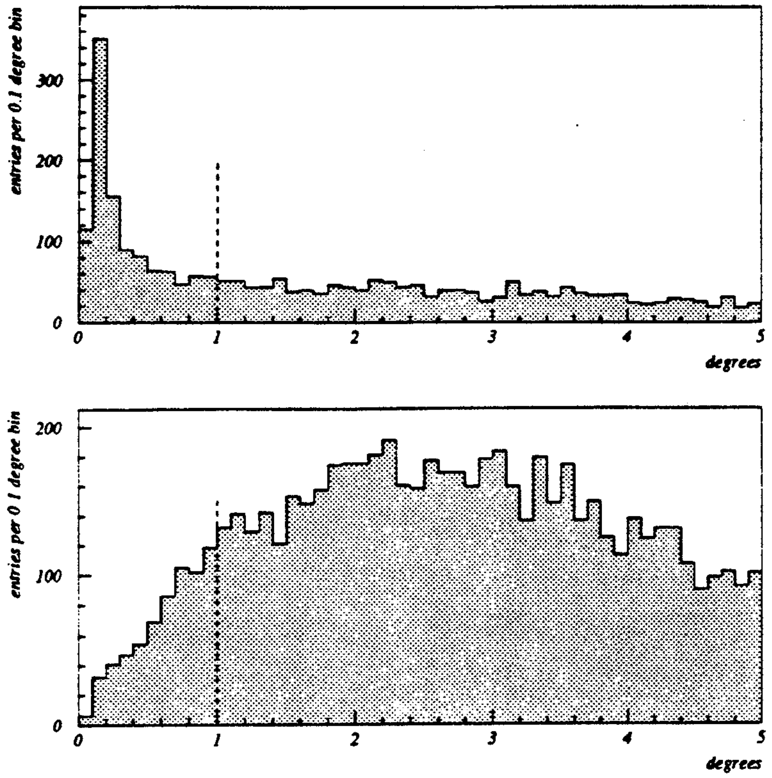

Fig 5.16; Final distribution of event acollinearity, for 5.16a (top) real data and **5.16b (bottom)** $\tau^+\tau^-$ simulation.

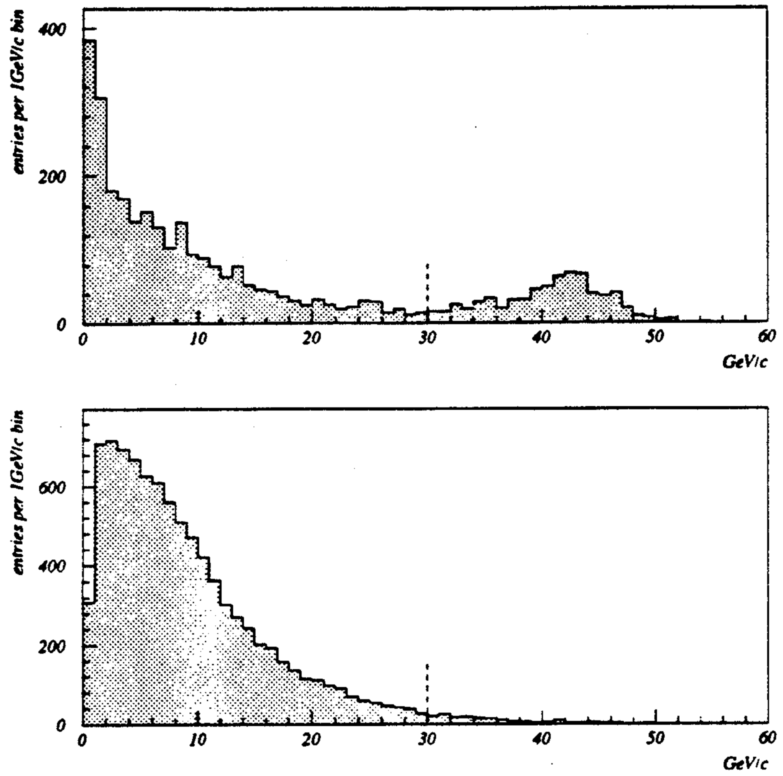

Fig 5.17; **Final distribution of minimum track momentum in 5.17a (top) real data and 5.17b (bottom) $\tau^+\tau^-$ simulation events.**

Cuts (5.10) reject any remaining dimuon events or cosmic ray tracks in the data, and are borne out by the distributions shown in Figs 5.16 and 5.17.

5.5 A τ event sample

A data sample of τ events has been selected for the lifetime measurement of Chapter 6. 1933 selected events had topology 1v1, and 643 events had topology 1v3. Only events of topology 1v1 will be used in the lifetime measurement.

Levels of contamination of non-$\tau^+\tau^-$ events in the data sample have been evaluated by applying the cuts of this Chapter to simulated data of various event classes[36]. Contamination into topology 1v3 is estimated to be 2.5±1%. Contamination into topology 1v1 (after certain data quality cuts for the τ lifetime measurement - see section 6.6) is estimated to be 7±1.5%.

Chapter 6. A measurement of the τ lifetime

Two methods for measuring the τ lifetime, were introduced in Chapter 1. This Chapter now presents in detail an analysis of data taken at DELPHI during 1990, in a measurement of the τ lifetime by the impact parameter method. A complimentary lifetime measurement on a sample of three prong τ decays by the secondary vertex reconstruction method is included in ref [1]. In order that the results from the two analyses be as uncorrelated as possible, the impact parameter method has been used here only on tracks from 1v1 τ decay (thus on only 75% of the total $\tau^+\tau^-$ event sample).

6.1 Impact parameter conventions

In what follows, there will be considerable emphasis on the difference between the so-called geometrically signed impact parameter and the lifetime signed impact parameter. The moduli of these two quantities are identical for a given track, and are equal to the absolute distance of closest approach of the track to the assumed point of production (the beam centre) in the $r\phi$ plane. For primary particles, the existence of non-zero impact parameters is due to detector resolution effects and the finite size of the beam about its centre. For decay products from short-lived particle decay, there is a contribution to impact parameter from the distance of flight of the primary parent particle. The signs allocated according to the two conventions may be the same or may differ, but bear no analytic relation to one another.

The sign of the geometric impact parameter is dependent purely on which sense of rotation about the production point is assumed by the track in question[4]. Hence in Fig 6.1 tracks 1 and 3 have positive, and tracks 2 and 4 negative, geometric impact parameter.

---

[4] There exist many possible geometric sign conventions for impact parameter, all based upon some similar principle of symmetry. It is in general unimportant which convention is employed.

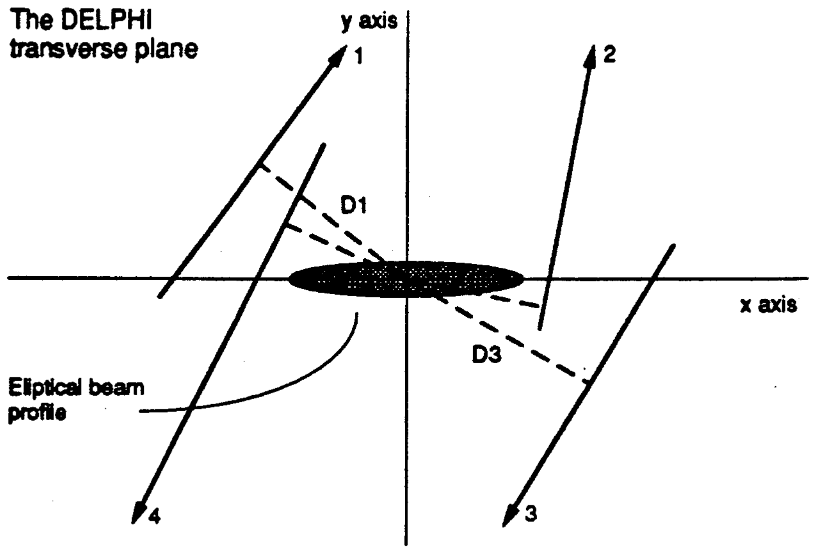

Fig 6.1; Definition of geometric impact parameter (see text). Note that the 'miss distance' between two tracks is defined as the sum of two geometrically signed impact parameters, e.g. here D1+D3. To a good approximation, the sum is equal to the perpendicular distance between the tracks, which are essentially parallel.

Where lifetime signed impact parameters are concerned, the case is more complex. It was stated above that the magnitude of an impact parameter is related to the distance of flight of any shortlived primary particle as well as to resolution and beamsize effects. Consider the case where a perfect detector records information on tracks emanating from a point beam (Fig 6.2a). The magnitude of the impact parameter d_0 is now linearly proportional to the distance of flight, and hence to the lifetime, of the primary particle;

$$|d_0| = \beta ct \times \sin(\theta)\sin(\Delta\phi) \tag{6.1}$$

where βct is the distance travelled by the shortlived primary particle, θ is the polar angle of the measured charged track and $\Delta\phi$ is the difference in azimuthal angle between the measured track and the primary particle (see Fig). It is clear that in a perfect detector, the reconstructed track, coincident with the true track, must intersect the projected primary particle direction at the point of the

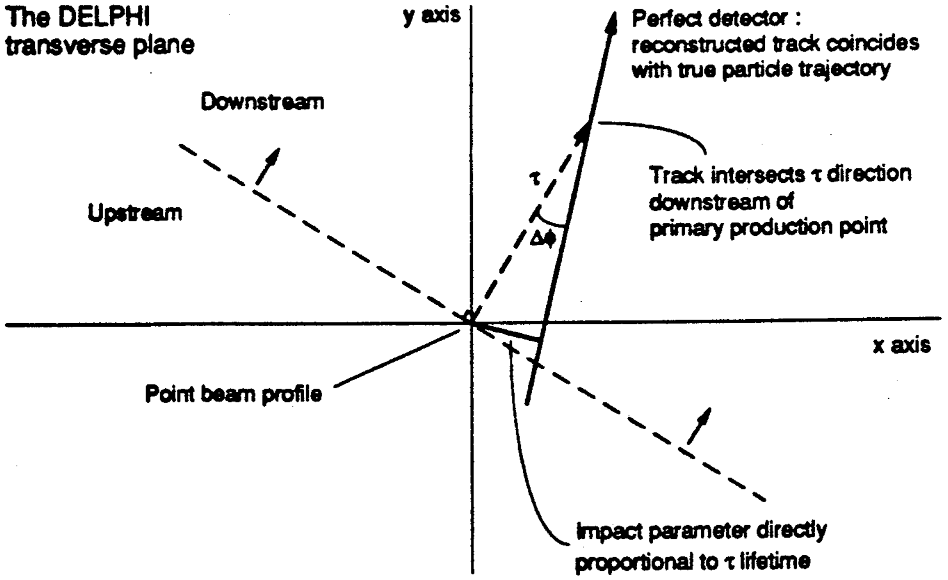

6.2a For a perfect detector, if the true direction of flight of the τ were known.

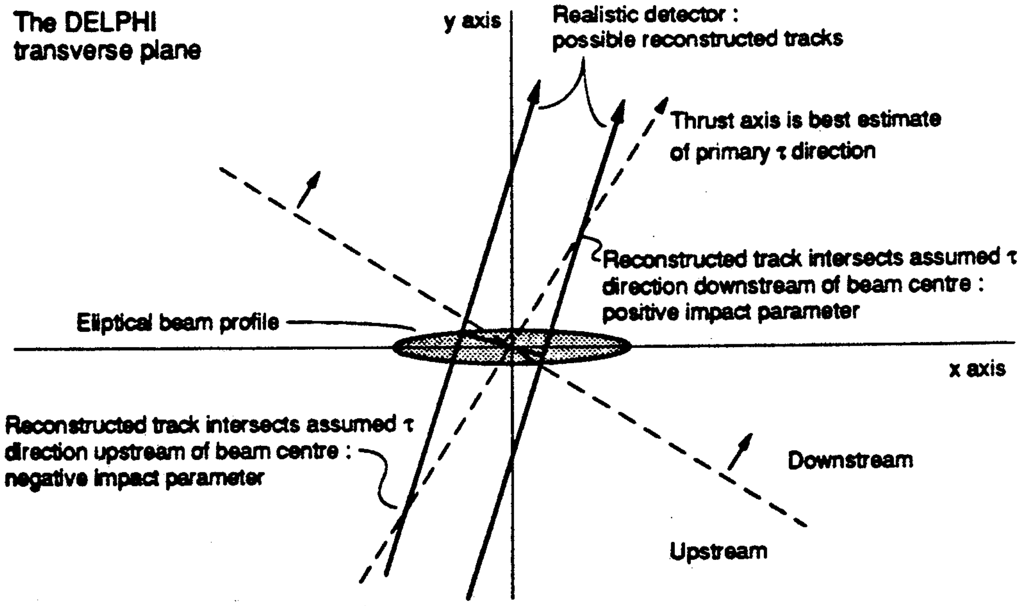

6.2b In the realistic case where detector resolution and uncertainties in the τ direction can lead to negative impact parameter signs.

Fig 6.2; Definition of lifetime signed impact parameter.

secondary decay. It is therefore possible to define lifetime signed impact parameters positive when the secondary track intersects the projected primary direction 'downstream', as defined by the primary particle momentum, of the production point. Furthermore, the linear relation of equation (6.1) is now between primary particle lifetime and lifetime signed impact parameter, rather than its magnitude.

Fig 6.3a shows the distribution of lifetime signed impact parameters one might expect to observe in the unrealistic case that the detector resolution is perfect and the primary particle direction is correctly known. Its form reflects the exponential distribution of distances travelled by shortlived particles in three dimensions. Impact parameters are measured in two dimensional $r\phi$ projection, and entries in the distribution are of the form $R_e / \sin(\theta)$, where R_e is a random number taken from an exponential distribution and θ is the polar angle of travel of the parent τ in the DELPHI coordinate system. No attempt is made to correct for the travel of the τ out of the transverse plane. All impact parameter distributions shown as part of this analysis will be of similar form to Fig 6.3a in this respect.

Where data from a real detector are concerned, the azimuthal direction of flight of the primary particle is not known, but can only be estimated. The major thrust axis of the event in $r\phi$ projection generally provides a good approximation to the projected primary direction. Fig 6.4 shows in simulation how the calculated ϕ coordinate of the thrust axis relates to the primary τ direction, for 1v1 τ events from the KORALZ event generating program ([37], see section 6.3). The two ϕ directions are usually coincident to better than 1°.

If the event thrust axis is used to mimic the primary particle direction, it can happen that a track intersects the assumed direction 'upstream', on the unrealistic side, of the production point (Fig 6.2b). In such instances, the lifetime signed impact parameter is defined to be negative. Fig 6.3b shows the distribution of lifetime signed impact parameters one might obtain with a perfect detector, but using the thrust axis to mimic the τ direction. It is of interest to note that the distribution does not represent Fig 6.3a convoluted with some smearing function. Either the sign given to an impact parameter is right or it is wrong, and so a proportion of the ideal distribution shown in

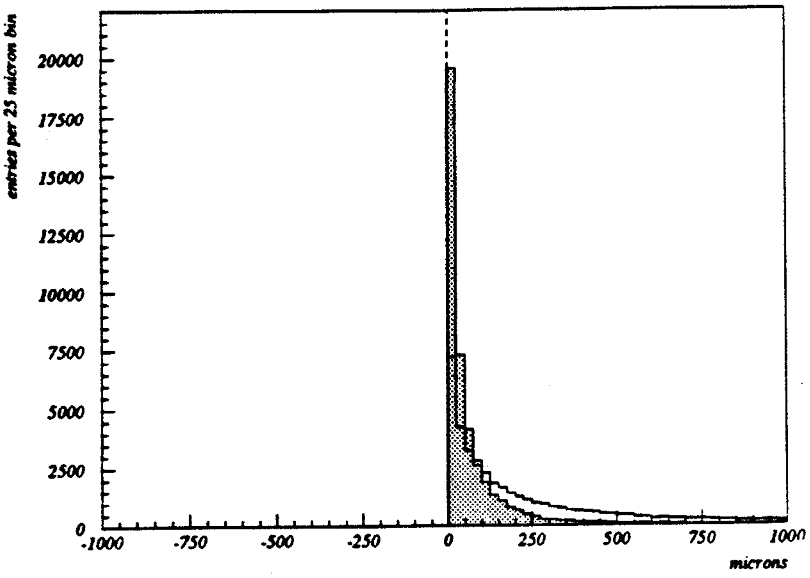

6.3a The case when detector resolution is perfect and the τ's direction of flight and point of production are known.

6.3b Perfect detector resolution, using the event thrust axis to mimic the τ direction.

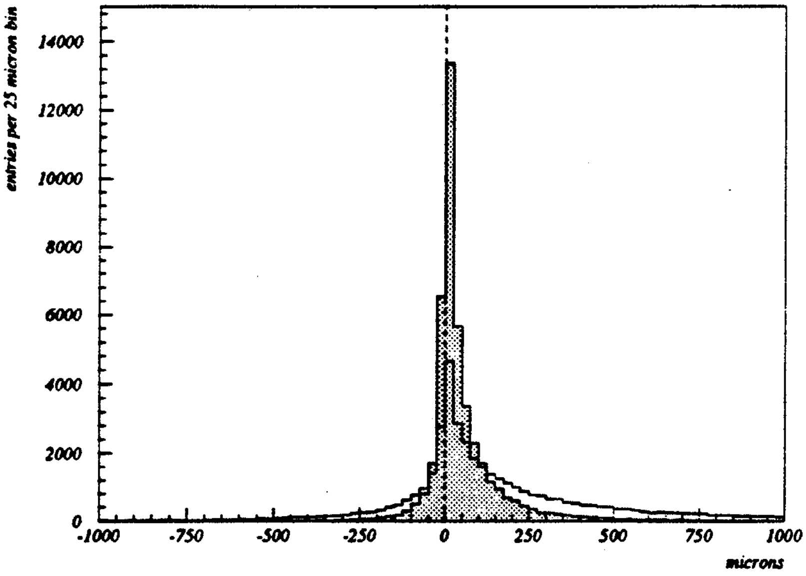

Fig 6.3; Lifetime signed impact parameter distributions (cont. overleaf). Hatched (unhatched) for τs of lifetime 1 (5) × the current world average.

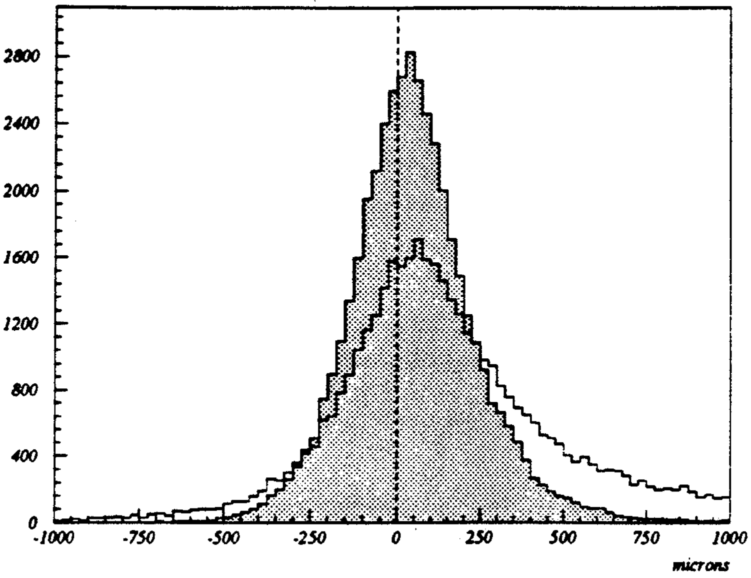

6.3c The realistic case when resolution effects and a finite Z^0 decay profile have been taken into account.

Fig 6.3 (cont.).

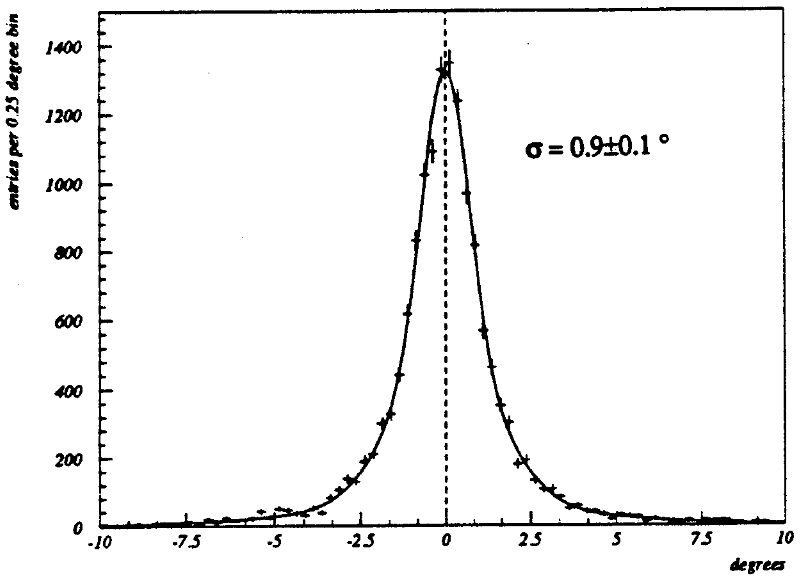

Fig 6.4; Difference in φ angle between τ direction and thrust axis (simulation).

Fig 6.3a is reflected in the vertical axis. Fig 6.3b simply represents two decaying functions back to back.

Detector resolution effects also result in some reconstructed tracks intersecting the primary direction upstream, giving negative lifetime signed impact parameters (also Fig 6.2b). In such realistic cases, the direct linear relation between the primary lifetime and the lifetime signed impact parameter is lost at the track by track level (it is obvious that no τ exists for a negative amount of time). However, it is easy to show that when an asymmetric function is convoluted with a symmetric function the means of the initial asymmetric function and the resulting function are identical. It follows that in a realistic detector, and indeed where beam sizes are finite, the mean of the lifetime signed impact parameter distribution will be directly proportional to the lifetime of the primary particle concerned. Fig 6.3c shows the shape of the distribution expected for real data, where all realistic effects resulting in negative impact parameters have been taken into account. The mean of this distribution is the same as that of Fig 6.3b, and is close to 50μm.

It is worth noting at this stage that while track by track there is no direct proportionality between lifetime signed impact parameter and primary particle lifetime for realistic data, information on the lifetime of the primary particle is carried by every measured lifetime signed impact parameter as probabilistic information. This must of course be the case for the mean of the distribution to carry information, and will become increasingly important in section 6.8.

6.2 Uncertainties on impact parameter measurements

The impact parameter of a reconstructed track is the distance of closest approach of the track to the position of the Z^0 decay in the event in $r\phi$ projection. The exact position of a Z^0 decay can never be known, and so here Z^0s are always assumed to have decayed at the beam centre. Some random errors are consequently introduced into impact parameter measurements. A geometric impact parameter distribution is shown for charged tracks from the dimuon decay channel of the Z^0 in Fig 6.5. The fact that the distribution has finite width, rather than resembling a δ-function at zero impact parameter, is due firstly to the tracking resolution of DELPHI, and secondly to the size and uncertainty in the position of the beam.

Fig 6.6 shows schematically various quantities which are of interest when considering impact parameter errors. The error σ_{IP} on the measurement of any impact parameter can be understood in terms of two dominant components, the tracking error σ_T in the direction perpendicular to the track at the point of closest approach, and the projected width σ_P of the beam as seen from the ϕ direction of the track itself (see Fig). Formally,

$$\sigma_{IP}^2 = \sigma_T^2 + \sigma_P^2 \tag{6.2}$$

where all errors have been assumed to be Gaussian in nature at this stage, and where

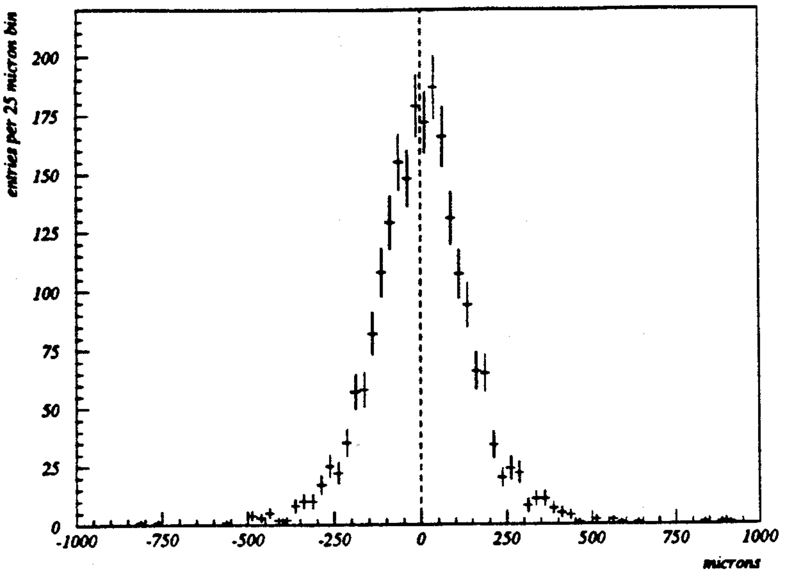

Fig 6.5; Geometric impact parameter for tracks from dimuon Z^0 decay.

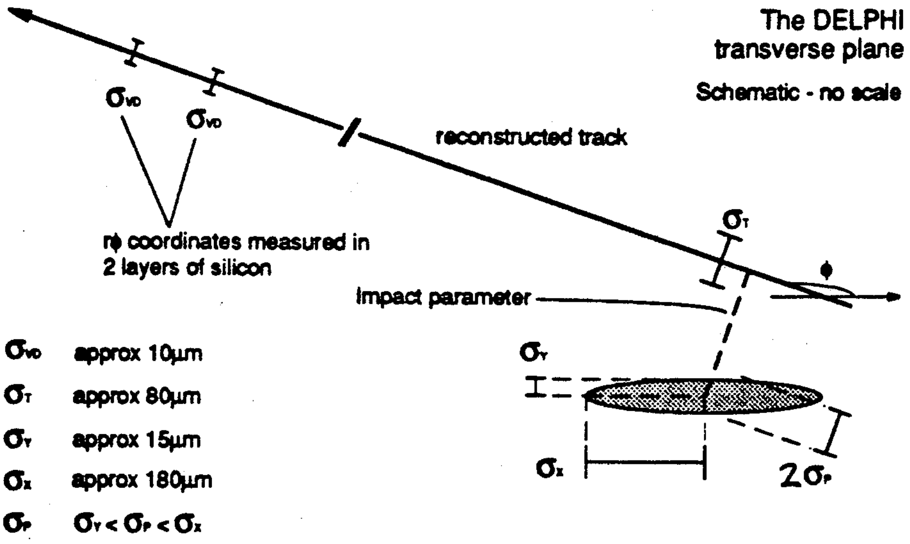

Fig 6.6; **Definition of symbols.** Note that σ_T is calculated from σ_{VD}, and σ_P from the size of the elliptical beam and the track direction ϕ. The error σ_{IP} on any impact parameter measurement is the quadratic sum of σ_T and σ_P (equation 6.1).

$$\sigma_P^2 = \frac{\dfrac{\cos^2\phi}{\sigma_X^2} + \dfrac{\sin^2\phi}{\sigma_Y^2}}{\left[\dfrac{\cos^2\phi}{\sigma_X^2} + \dfrac{\sin^2\phi}{\sigma_Y^2}\right]\left[\dfrac{\cos^2\phi}{\sigma_Y^2} + \dfrac{\sin^2\phi}{\sigma_X^2}\right] - \cos^2\phi\,\sin^2\phi\left[\dfrac{1}{\sigma_X^2} - \dfrac{1}{\sigma_Y^2}\right]^2} \tag{6.3}$$

relates σ_P to the Gaussian widths σ_X and σ_Y of the beam interaction profile in two dimensions (section 6.3.2). It follows from equations (6.2) and (6.3) that σ_{IP} is dependent on ϕ. The error on any measurement of impact parameter is dependent on the azimuthal angle of the track, because of the elliptical nature of the interaction profile. The impact parameter data of Fig 6.5 are not binned in ϕ, and so the distribution is not Gaussian but represents the integral over ϕ of equation (6.3) in equation (6.2).

6.3 Simulation of data

At the time of this analysis, the official DELPHI simulation package (DELSIM) could not accurately simulate the performance of the vertex detector. In order that the data could be thoroughly understood, a private simulation program was written, in which vertex detector behaviour was imitated in a simple but accurate manner. Some description of this private simulation (known as KWIKSIM) is included here, as it has proved central to this measurement of the τ lifetime.

Clearly if DELPHI were an ideal detector, then any track passing through it could be perfectly reconstructed in later analysis. The need for simulation comes about because the detector is not ideal, and there are finite constraints of resolution on any measurement. The simulation package must accurately estimate the causes of resolution effects, and smear the required 'measured' distributions accordingly.

KWIKSIM takes into account four significant contributions which limit track extrapolation resolution near the primary vertex. The respective effects on impact parameter measurements of

- the finite rϕ resolution of the vertex detector layers

- the finite beam size
- the transverse momentum resolution of DELPHI
- multiple scattering in the beam pipe and VD inner layer

may be activated or deactivated at will, and are discussed in detail in the following four sections of this chapter. KWIKSIM reads events from LUND blocks, previously generated using either the KORALZ program[37] (for $\tau^+\tau^-$ events) or the DYMU3 program[38] (for $\mu^+\mu^-$ events). The positions of realistic hits produced in the VD by a track are calculated, and the track is refit so that realistic impact parameters may be calculated. A track fitting procedure is adopted where a circle, of radius appropriate to the smeared momentum of the track concerned, is forced through hits in both layers of the vertex detector. If data simulation is to be representative of the real detector, clearly a similar track refit must be applied when impact parameters are to be measured in the real data (see section 6.5). The following sections present results to compare simulated KWIKSIM data with experimental data.

6.3.1 VD resolution effects

A convenient and simple way to inspect the resolution of the vertex detector is by considering a muon miss distance plot. Such a plot consists of entries which represent the distance measured at the origin between two muon tracks from Z^0 decay. The distance can be very closely approximated as the sum of two geometrically signed impact parameters to the production point (Fig 6.1). Assuming Gaussian errors, the width of the muon miss distance plot σ_{MD} is simply related to the tracking resolution σ_T in the direction of impact parameter measurements D1 and D3;

$$\begin{aligned} \sigma_{MD}^2 &= 2 \times \sigma_T^2 \\ \sigma_T &= \frac{\sigma_{MD}}{\sqrt{2}} \end{aligned} \tag{6.4}$$

After simple geometric considerations and standard error propagation, a relation between σ_T and the resolution σ_{VD} in $r\phi$ in the silicon of the VD can be derived for the simplistic track fit used here;

$$\sigma_T^2 = \left[\frac{r_1^2 + r_2^2}{(r_2 - r_1)^2} \right] \sigma_{VD}^2 \qquad (6.5)$$

where r_1 and r_2 are the mean radii of the silicon layers of the VD and the resolution σ_{VD} is assumed to be the same in both layers. From equations (6.4) and (6.5) it follows that

$$\sigma_{VD} = \left[\frac{(r_2 - r_1)}{\sqrt{2(r_1^2 + r_2^2)}} \right] \sigma_{MD} \qquad (6.6)$$

$$\text{i.e.} \quad \sigma_{VD} = 0.10 \times \sigma_{MD}$$

Because a muon miss distance is calculated as the difference between two impact parameters, the point of production of the dimuon pair within the beam profile is immaterial, and beam size does not affect σ_{MD}. For dimuon tracks, multiple scattering will be unimportant, and momentum resolution good (sections 6.3.4 and 6.3.3) and so equation (6.6) represents an effective way of relating directly vertex detector resolution and the muon miss distance standard deviation.

Fig 6.7 shows the muon miss distance plot for real dimuon events from DELPHI (where in the calculation of impact parameter a circle fit has been forced through hits in the inner and outer VD layers) and a three parameter Gaussian fit to the data. The width of the Gaussian fit infers a real VD resolution of 11μm per rϕ coordinate in each layer of silicon. Also shown are high statistics simulated data, where VD hits in KWIKSIM have been smeared according to a Gaussian of width 11μm and the simulated distribution has been normalised to the area under the real data distribution. Agreement between simulated data and real data is good : the conclusion can be drawn that VD resolution is well estimated by a Gaussian of the width specified above.

It is of interest to examine the effect that realistic vertex detector resolution has on the lifetime signed impact parameter distribution. The underlying ideal distribution one might observe with a perfect detector and knowledge of the primary τ direction was shown in Fig 6.3. Fig 6.8 now shows KWIKSIM lifetime signed impact parameter data for tracks from 1v1 τ decays, where the true τ direction has been used for the primary direction, and the only realistic resolution effect taken into account has been the Gaussian smearing of rϕ coordinates in the silicon of the VD. A point

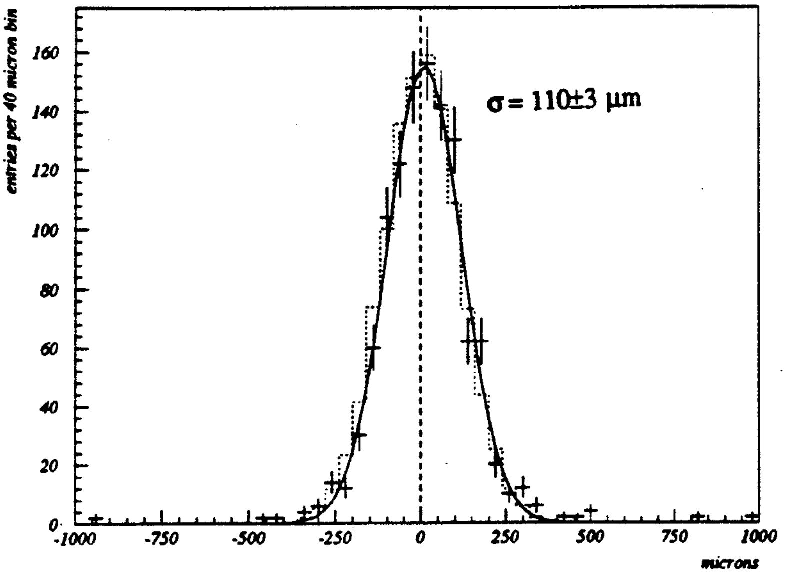

Fig 6.7; **Miss distance for tracks from dimuon Z^0 decay with Gaussian fit.** The dashed line shows simulated data from KWIKSIM, where a VD resolution of 11μm per silicon layer has been assumed.

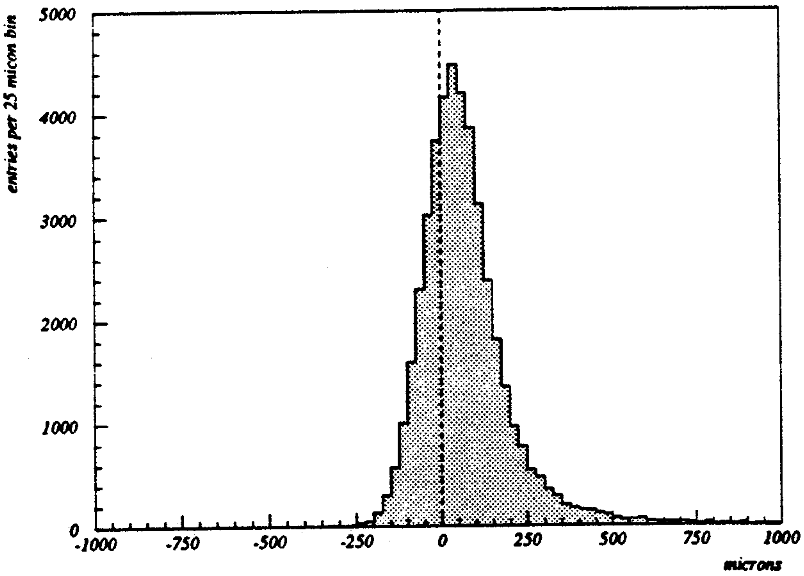

Fig 6.8. Showing the smearing effect of VD resolution on the distribution of lifetime signed impact parameters for tracks from τ decay in simulation.

beam profile has been assumed, no multiple scattering has been allowed, and momentum resolution is taken to be perfect. Note that a considerable proportion of the simulated tracks are assigned negative lifetime impact parameters purely due to the finite resolution of the VD. The better the nominal resolution of the detector, the fewer the number of tracks which are assigned negative sign. Note also that because a circle fit through 2 VD hits is used here, the VD hit resolution is directly proportional to the angle error in ϕ in the refit track. It is equally valid to consider that the number of negative impact parameters is a function of tracking angle error.

6.3.2 Beam size effects

Within DELPHI, bunches of electrons and positrons collide in some small spatial volume close to the origin of the DELPHI coordinate system. The interaction profile of two particle beams of Gaussian profile is a factor of $\sqrt{2}$ smaller in x and in y than the physical size of either of the individual circulating beams themselves. It is the interaction profile which is of interest, and beam dimensions discussed in this thesis refer always to the profile of Z^0 decays.

In $r\phi$ projection, the interaction profile is usually approximated as a 2 dimensional Gaussian, of widths $\approx 200\mu m$ in x and $\approx 20\mu m$ in y. The best way of examining the beam profile is to plot geometric impact parameter distributions for horizontal and vertical fast muon tracks from Z^0 decay separately. The widths of these distributions then represent a convolution of the tracking error in the impact parameter direction and the required information on the size of the beam.

Figs 6.9a and 6.9b show geometric impact parameter distributions, for tracks from the dimuon decay of the Z^0, and for equivalent data from KWIKSIM. The values used for the Gaussian widths in x and y of the beam profile in simulation have been optimised to $180\mu m$ and $15\mu m$ respectively. Agreement is fair, and while understanding of the beam position and size is not perfect, the Gaussian widths used in KWIKSIM are in excellent agreement with other beamsize studies undertaken with hadronic data. Beam position and size in real data are discussed in section 6.4.

Fig 6.10 shows the effect of beamsize alone on an ideal lifetime signed impact parameter distribution. The number of negative impact parameters is substantial, and it will be seen that the size in

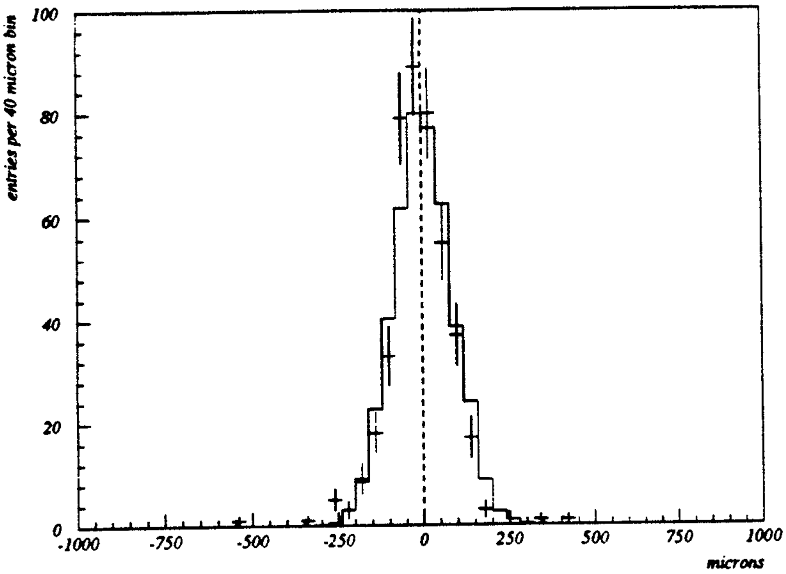

6.9a For tracks within 15° of the horizontal in ϕ coordinate.

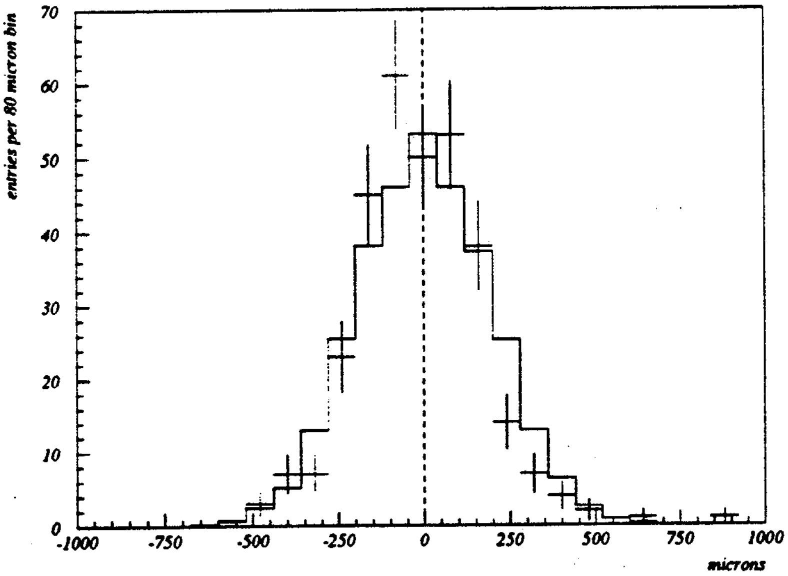

6.9b For tracks within 15° of the vertical in ϕ coordinate.

Fig 6.9; Geometrically signed impact parameter distributions for tracks from dimuon Z^0 decay.

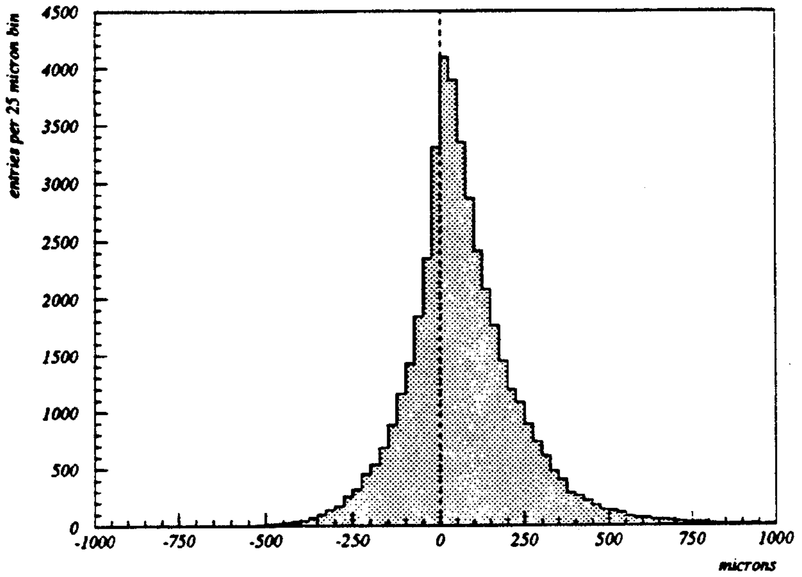

Fig 6.10. Showing the smearing effect of a finite beam interaction profile on the distribution of lifetime signed impact parameters for tracks from τ decay in simulation.

x of the LEP beam, together with the effect of finite VD resolution discussed above in 6.3.1, dominate the precision of the τ lifetime measurement. Clearly, the broader the beam, the greater the number of negative impact parameters, and the less precise that measurement will be.

6.3.3 Momentum resolution effects

The momentum resolution of the DELPHI tracking detectors was discussed in section 2.2. In KWIKSIM, this resolution is simulated by appropriate smearing of the transverse momenta used in the calculation of the radii of the circles forced through VD hits in the simple track fit (equation (2.1)). From Fig 2.5, a suitable value for σ_{1/P_t} to use in simulation is taken to be 0.002(GeV/c)$^{-1}$.

Fig 6.11 shows the effect of transverse momentum resolution alone on the ideal lifetime signed impact parameter distribution for tracks from τ decay.

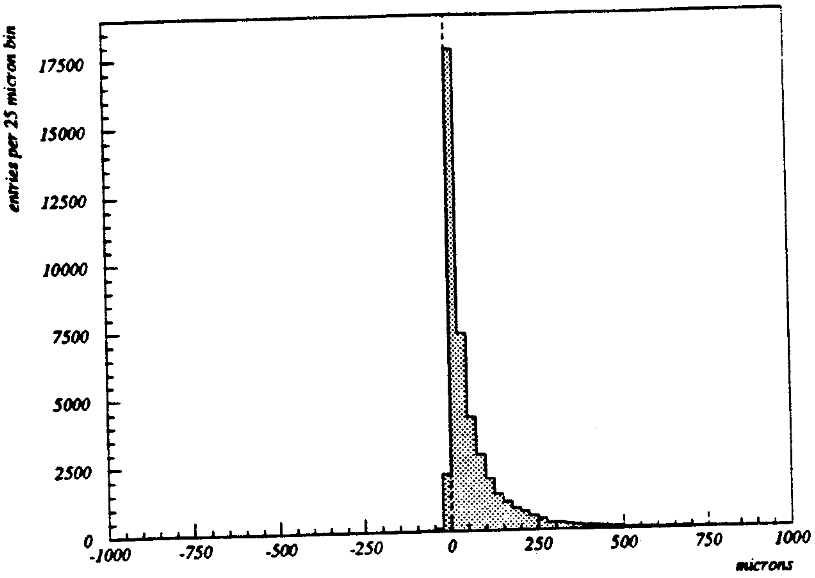

Fig 6.11. Showing the smearing effect of DELPHI momentum resolution on the distribution of lifetime signed impact parameters for tracks from τ decay in simulation.

6.3.4 Multiple scattering effects

As a particle passes through a detector, it scatters in the material from which the detector is made. The longer the track length through the detector material, the more scattering the particle will undergo. The path deviation in plane projection of an incident particle of unit charge can be approximately described[39, 40] by defining a reference angle θ_0 in radians:

$$\theta_0 = \frac{14.1\ \mathrm{MeV}}{p\beta}\sqrt{\frac{L}{L_r}}\left(1 + \frac{\log_{10}(L/L_r)}{9}\right) \qquad (6.7)$$

where L is the length of material through which the incident particle travels and L_r is the radiation length for the material. The overall angular scatter in the plane θ and translation Y perpendicular to

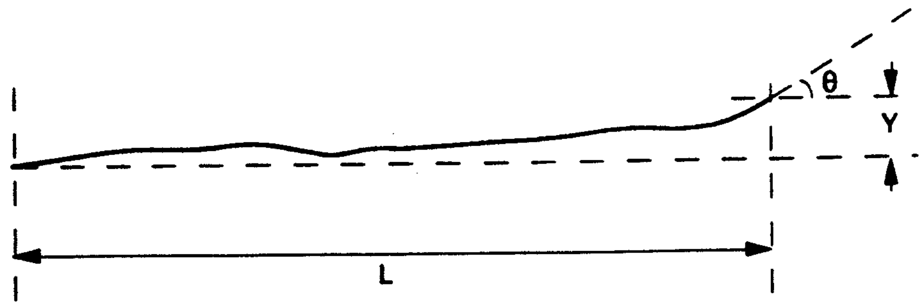

Fig 6.12; Definition of parameters of multiple scattering.

the incident particle direction (Fig 6.12) are then distributed according to two Gaussian random numbers R_1 and R_2 of mean zero and variance θ_0 ; [5]

$$\begin{aligned} \theta &= R_1 \\ Y &= \frac{R_1 L}{2} + \frac{R_2 L}{\sqrt{12}} \end{aligned} \tag{6.8}$$

(where the first term for Y represents the displacement that would have occurred had deflection θ all occurred at the single point L/2 [7]).

Fig 6.13 shows the resolution effect of multiple scattering alone on an ideal lifetime signed impact parameter distribution. Clearly the effect is a small one compared to those of VD resolution and the size of the beam. It is however significant enough not to be neglected, and care must be taken to allow for the momentum dependence of the effect when considering the choice of resolution function (section 6.6.3).

---

[5] This approximation is good to about 5%.

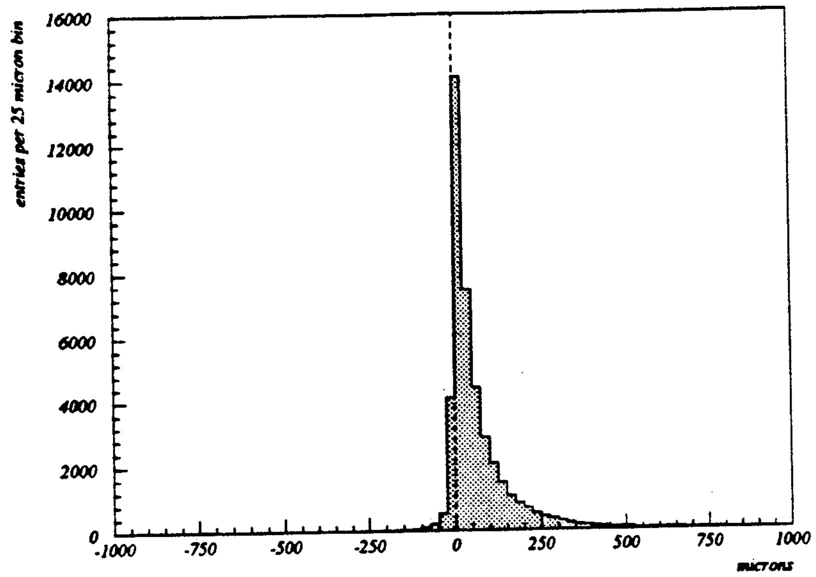

Fig 6.13. Showing the smearing effect of multiple scattering on the distribution of lifetime signed impact parameters for tracks from τ decay in simulation.

6.4 Determination of beamspot

It is expected from the design of the LEP machine that the beam position may move within DELPHI over distances comparable with the (approximately) Gaussian widths of the beam profile. While it would be possible to make a τ lifetime measurement with only very approximate knowledge of the beam position, uncertainties and movements with time would contribute to a broadening of impact parameter distributions, and a consequent loss of precision on the measurement. For all fills of the LEP ring throughout the 1990 DELPHI data taking period, the position of the beam centre, and the width of the beam in x, have been measured by the reconstruction of primary vertices from hadronic events[41]. Fig 6.14 shows the movement of the beam centre from fill to fill as determined by this analysis.

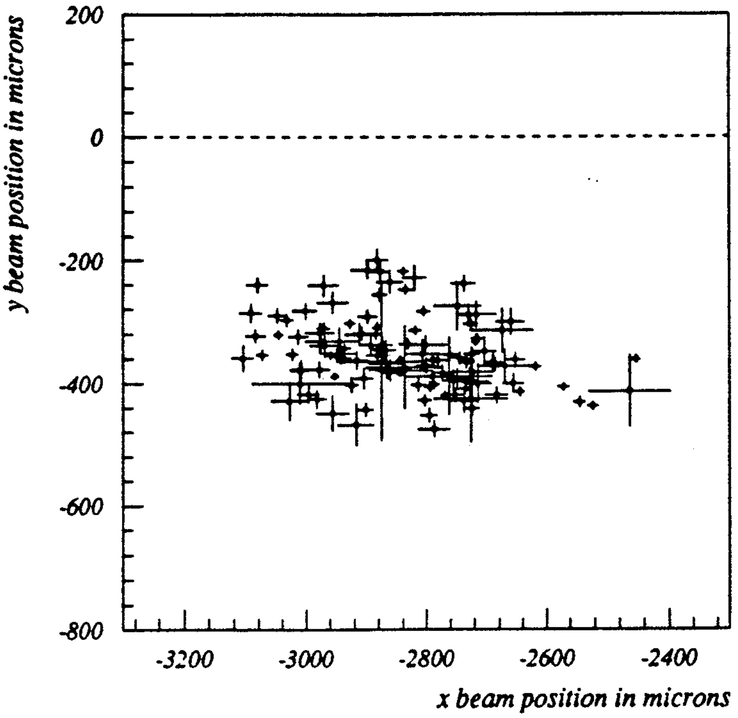

Fig 6.14; LEP beam position fill by fill through the 1990 running period. Note that the size of the beam is large compared to uncertainties on the position of the beam centre.

It is assumed that within a fill the beam does not move, and that the beam size in y is negligible compared to the error on the beamspot centre position determination. The quadratic difference in the widths of the primary vertex distributions in x and in y then gives an measure of the spread of the beam in x. The observed quadratic difference, ≈ 200±20 μm, agrees well with the approximate beamsize in x deduced in section 6.3.2 (180μm).

6.5 Impact parameters in real data

A sample of 1v1 $\tau^+\tau^-$ EVENTS was isolated in Chapter 5. The vertex detector played no part in the τ sample isolation. In order that impact parameters be precisely calculable, it is now necessary to associate hits in the microvertex detector with tracks in the τ sample.

In order to achieve the best possible impact parameter resolution, only tracks have been used in this analysis where hits have been generated in both layers of the VD. The VD was approximately 90% efficient throughout 1990 and so this quality criterion reduces the statistics available a priori to $(90\%)^2$ (i.e. 80%) the possible maximum. Vertex detector hits are associated to tracks by simple matching of ϕ coordinates. Fig 6.15 shows the difference in ϕ coordinate between the track extrapolation from the DELPHI tracking chambers to the microvertex detector and a VD hit, for VD hits in the 1v1 τ event data sample. It is required for a track to be used here that there be in ~~either~~ EACH layer exactly one VD hit within 0.4° in ϕ of the track extrapolation from the tracking chambers, and further that there be no VD hits in the same event within an exclusion region extending from 0.4° to 2.0° from the track extrapolation. These severe association requirements are intended to reduce the possibility of confusion between noise hits and genuine hits to a minimum. Of the available 3866 tracks from 1v1 τ decay, 1256 meet VD hit association criteria.

A secondary effect of the tight VD hit association requirements is that tracks with badly reconstructed momenta in the tracking chambers are excluded from the lifetime measurement data sample. Such tracks extrapolate to points on the vertex detector relatively far removed from their true VD hits, and so produce entries in the tails of Fig 6.15. As shown in Fig 6.16, the transverse momentum distribution of tracks which have passed VD hit association criteria (and the data quality

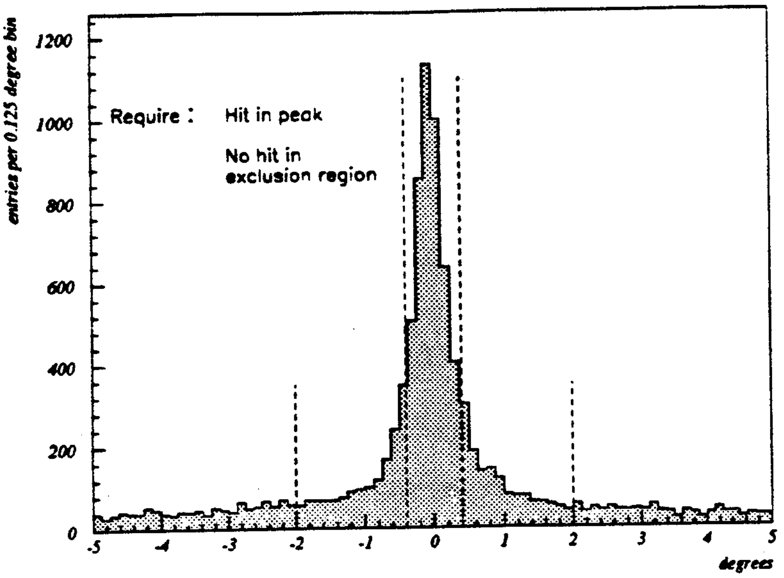

Fig 6.15; Association of VD hits to track extrapolations by simple angular cuts.

cuts of section 6.6) agrees well with that expected for tracks from τ decay. The efficiency of VD hit association is the same over the whole momentum spectrum, and so no systematic biases are introduced into impact parameter measurements here.

It has been stated above that in order to permit the use of the KWIKSIM simulation program in estimating vertex detector behaviour in this analysis, it has been necessary throughout to refit tracks by forcing a circle through VD hits in the inner and outer layers of silicon. An advantage associated with this practical requirement is that the relative alignment between the VD and the other subdetectors in DELPHI has no systematic effect on impact parameter precision. Momentum measurements giving circle radii are independent of external alignment because they do not use VD information. External alignment need only be good enough to allow the VD hit association detailed above.

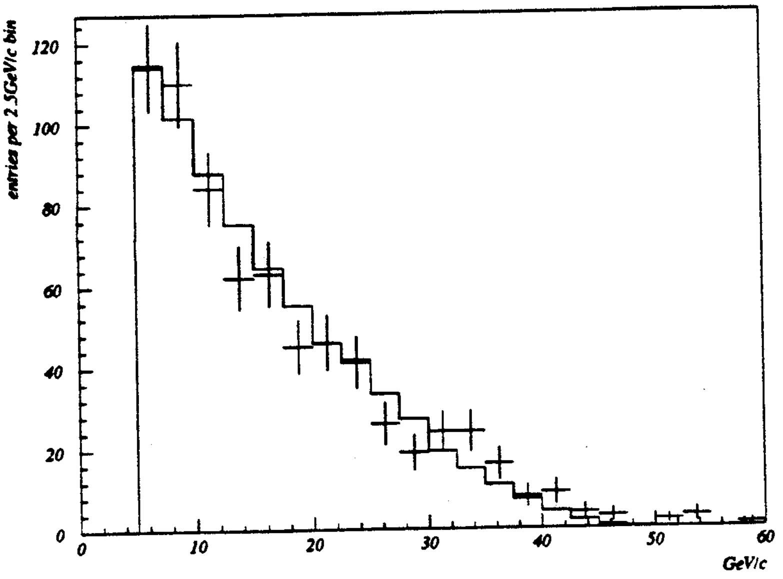

Fig 6.16; Transverse momentum for tracks from τ decay. Real data points and solid line simulation.

It is important to note that the simple track fit only marginally reduces the impact parameter resolution potential which might be achieved refitting over all DELPHI tracking points. This is because of the relative contributions to the impact parameter resolution σ_{IP} of the tracking error σ_T and the beamsize projection σ_P in the impact parameter direction. From equation (6.4), $\sigma_T \approx 80\mu m$ with the simple track fit used here. The average of σ_P over all ϕ is $128\mu m$ (equation (6.3)). The quadratic sum of the two, roughly the width of a dimuon geometric impact parameter plot such as Fig 6.5 is $150\mu m$ (equation (6.2)). Using all the tracking information of DELPHI would currently reduce the tracking error σ_T to $40\mu m$, and the consequent reduction in the width of the dimuon plot (value of σ_{IP}) would be to $134\mu m$. A small (10%) loss in impact parameter precision results from using two VD hits and an externally measured momentum.

It should be also be noted that equation (6.3) represents the relation between σ_X, σ_Y and σ_P in the ideal case that detector acceptance in ϕ is uniform. Fig 6.17 shows the distribution of tracks in ϕ for the τ data sample which will be used for the lifetime analysis of this Chapter. Its nonuniform

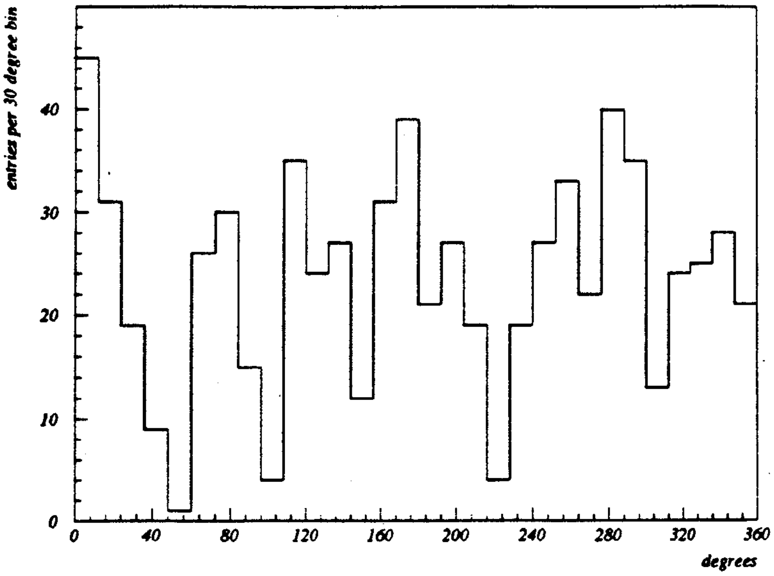

Fig 6.17a; Distribution of tracks from 1 prong τ decay in ϕ.

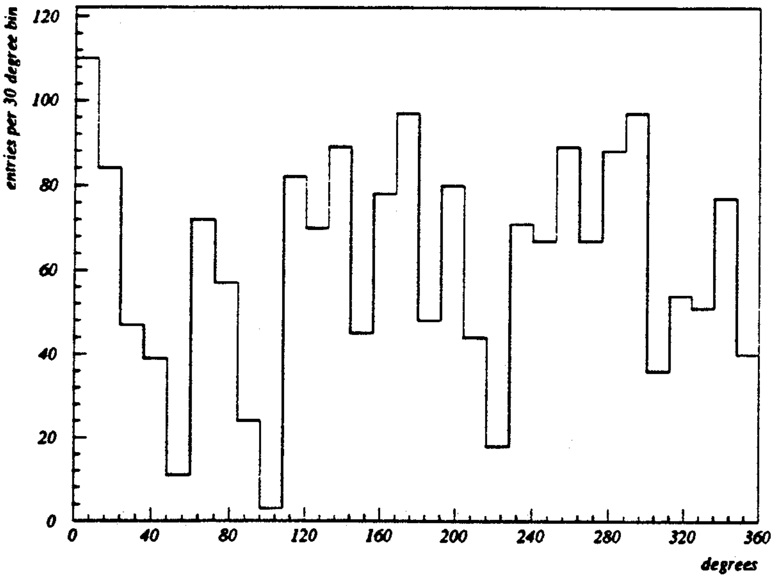

Fig 6.17b; Distribution of tracks from dimuon Z^0 decay in ϕ.

nature is due to the requirement that each track in the sample have a hit in both VD layers, and the fact that some VD modules were damaged on installation within DELPHI. Also shown is the equivalent distribution for the tracks from dimuon Z^0 decay used in the parametrisation of a resolution function (section 6.8.1). The two distributions agree well : deviations from the ideal behaviour predicted by equation (6.3) are accounted for in the lifetime analysis by the use of a resolution function.

6.6 Quality cuts on the τ data

In order to obtain consistency in the data of this lifetime analysis, it was necessary to introduce certain stringent data quality requirements on events from which tracks were taken. The requirements are outlined in the following sections of this Chapter. The level of contamination in the 1v1 $\tau^+\tau^-$ event sample after the quality cuts have been applied is estimated to be 6.0±1.5%[36].

6.6.1 Number of vertex detector hits

Fig 6.18 shows the distribution of total number of vertex detector hits recorded in τ events of 1v1 topology. Ideally, each track in the event should record 2 hits (4 in module overlap regions), giving a total of 4 (8) hits in a 1v1 event. Some vertex detector channels are inevitably noisy, and so the distribution of Fig 6.18 is peaked at rather higher numbers of hits. A cut on the maximum permitted number of hits in an event NVDHIT is imposed;

$$\text{NVDHIT} \leq 15 \qquad (6.9)$$

to reduce the chances of vertex detector hit misassociation, and eliminate events where the stability of the detector may be affected by the amount of data present. The cut reduces the number of suitable data tracks from 1256 to 1020

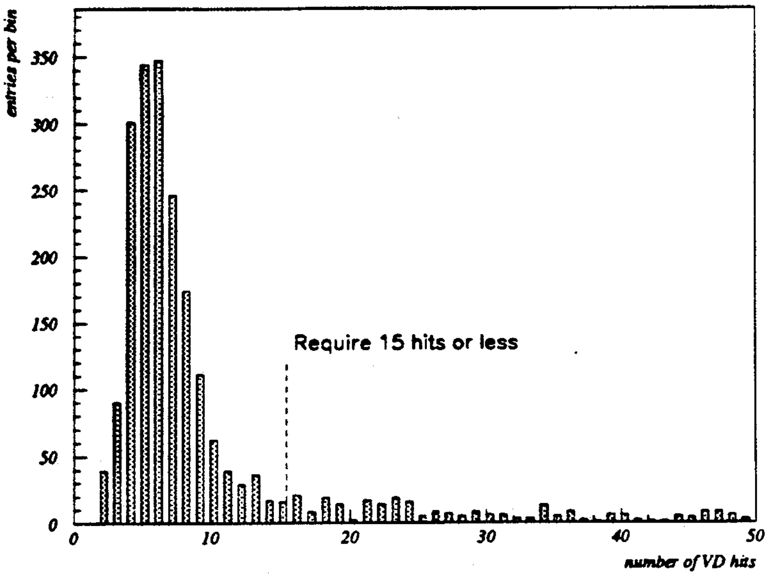

Fig 6.18; Number of VD hits recorded per $\tau^+\tau^-$ event.

6.6.2 Projected acollinearity

A further quality cut employed here concerns the acollinearity in the event as seen in rϕ projection. Consider the ideal case when two colinear tracks from τ decay are perfectly reconstructed in a detector with infinite resolution. The assumed τ direction, the thrust axis, is coincident with the tracks, and it is impossible to chose either negative or positive signs for the lifetime signed impact parameter. In this ideal limit, impact parameters are identically zero and there is no inconsistency, but as soon as some detector resolution is introduced, and a track angle error is allowed, positive impact parameters dominate purely as a result of the geometry involved (Fig 6.19). The effect is observed not only in tracks from τ decay. Fig 6.20 shows the lifetime signed impact parameter distribution for dimuon tracks from Z^0 decay. The dimuon tracks are themselves primary, so that there has been no shortlived particle to offset their production point from the position of the Z^0 decay. However, a positive offset is seen in the plot due to the highly colinear nature of dimuon

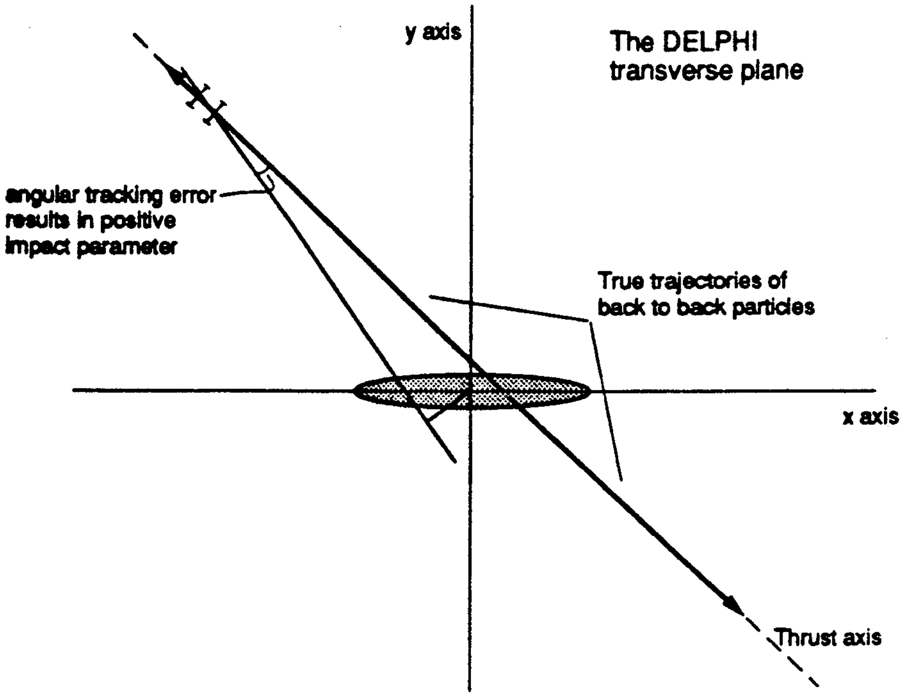

Fig 6.19; Fake lifetime signal due to collinear tracks in projection. Collinear tracks in projection coincide with the thrust axis, and tracking angle error leads to a bias towards high lifetimes.

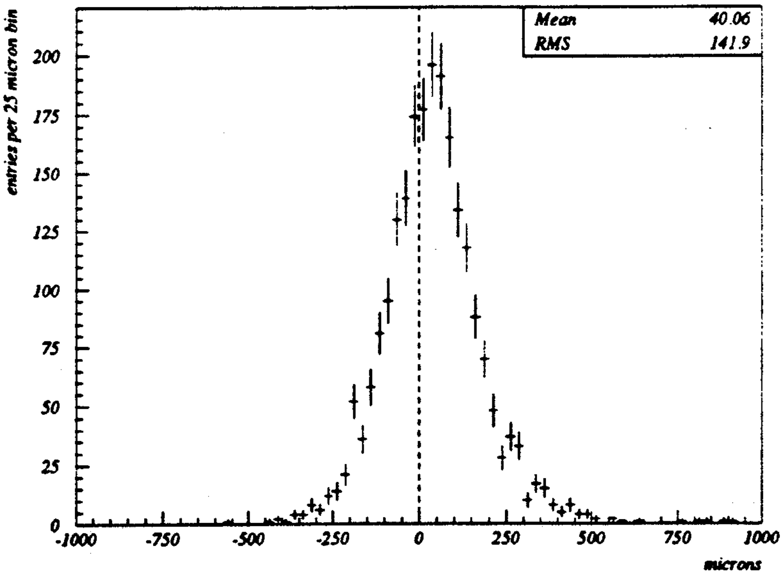

Fig 6.20; Lifetime signed impact parameter data for tracks from dimuon Z^0 decay.

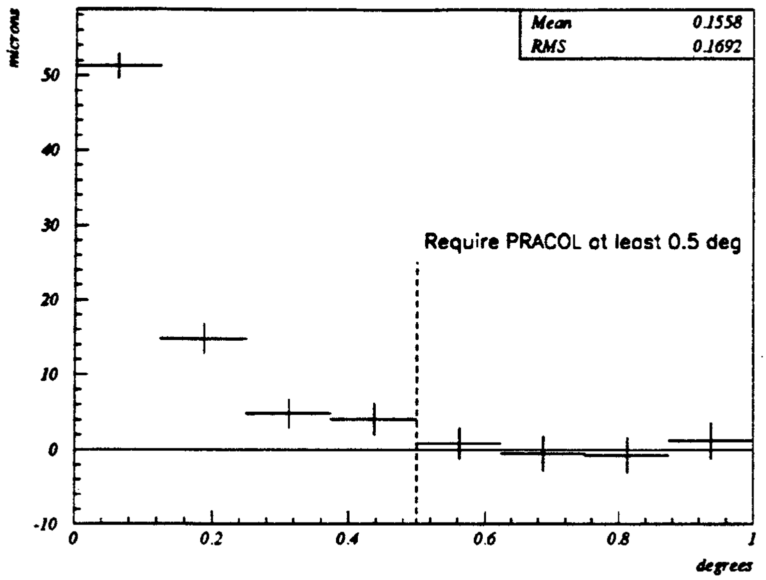

Fig 6.21; Mean measured lifetime signed impact parameter against projected acollinearity, for dimuon tracks in simulation.

events in $r\phi$ projection. A fake shortlived particle lifetime is inferred where no shortlived particle ever existed.

Fig 6.21 shows observed mean lifetime signed impact parameter scattered against projected acollinearity for KWIKSIM data, where an artificial projected acollinearity has been introduced into dimuon events with a Gaussian probability distribution to allow the effect to be investigated outside the normal range of dimuon projected acollinearity. In order to remove tracks carrying inherently biased lifetime information, a minimum cut in event projected acollinearity PRACOL is imposed;

$$\text{PRACOL} > 0.5^\circ \tag{6.10}$$

The cut reduces the data sample to 909 tracks.

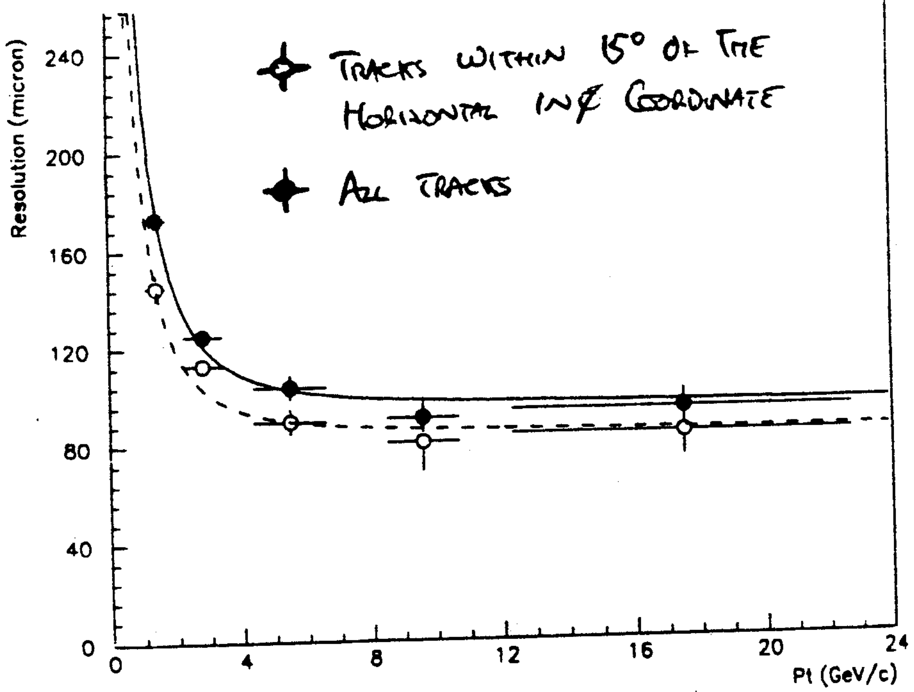

(FROM REF. [41])

Fig 6.22; Impact parameter resolution against transverse momentum.

6.6.3 Transverse momentum

From equation (6.7) it is clear that low momentum tracks undergo more scattering as they pass through the material of DELPHI than do high momentum tracks. In order to enable accurate determination of resolution effects on the τ lifetime measurement, it is desirable to exclude tracks which might have scattered through large angles from the data sample.

Fig 6.22 shows a plot of impact parameter resolution against transverse momentum P_t for tracks in hadronic Z^0 decay events in DELPHI. The plot has been obtained by measuring the impact parameters of hadronic tracks to the nominal beam centre, and allowing for the broadening of the distribution due to the fraction of tracks coming from b quark events. The effects of multiple scattering are clearly visible, and the empirical inverse power law may be derived from a fit to the data;

$$\sigma_{IP}^2 = a^2 + \left(\frac{b}{P_t}\right)^2 \qquad (6.11)$$

A cut on minimum allowed transverse momentum is imposed;

$$P_t > 5\ \mathrm{GeV/c} \tag{6.12}$$

reducing the final data sample to be considered to 724 tracks from 1-prong τ decay. The transverse momentum cut will be important when considering the resolution function in section 6.8.1.

6.7 τ lifetime from average impact parameter

The idea of proportionality between the average value of a lifetime signed impact parameter distribution and the lifetime of a shortlived particle was introduced in section 6.1. In this section, this proportionality is exploited, and a first estimate of the τ lifetime is derived from a sample of tracks from τ decay by inspecting the mean value of their lifetime signed impact parameters.

Fig 6.23 shows the distribution of impact parameters observed for the 724 tracks from 1 prong τ decay passing the selection cuts of section 6.6. The mean and RMS of the distribution are 40.2μm and 175μm respectively. In order to interpret these numbers as a lifetime measurement, calibration of the μm scale for impact parameter mean value in terms of corresponding τ lifetime has been carried out in simulation, as follows.

A large number of τ events were generated using the KORALZ program, and run through the official DELPHI simulation package DELSIM and the normal DELPHI data processing chain. The τ event selection criteria (section Chapter 5) and the data quality cuts (section 6.6) used on the real data were then applied, and the 21575 events which passed all cuts were flagged for use in the mean impact parameter calibration. The microvertex simulation program KWIKSIM was run on the KORALZ output of the flagged events five times, where in each of the five runs a different τ lifetime was simulated. The mean values of the impact parameter distributions for each of the five simulated τ lifetimes were calculated, and are plotted against the lifetimes used in Fig 6.24.

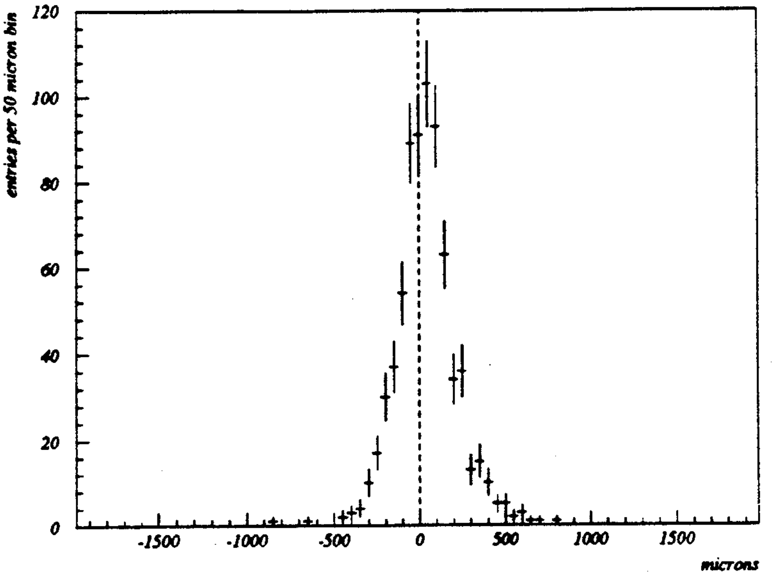

Fig 6.23; **Lifetime signed impact parameter distribution for tracks from 1 prong τ decay.**

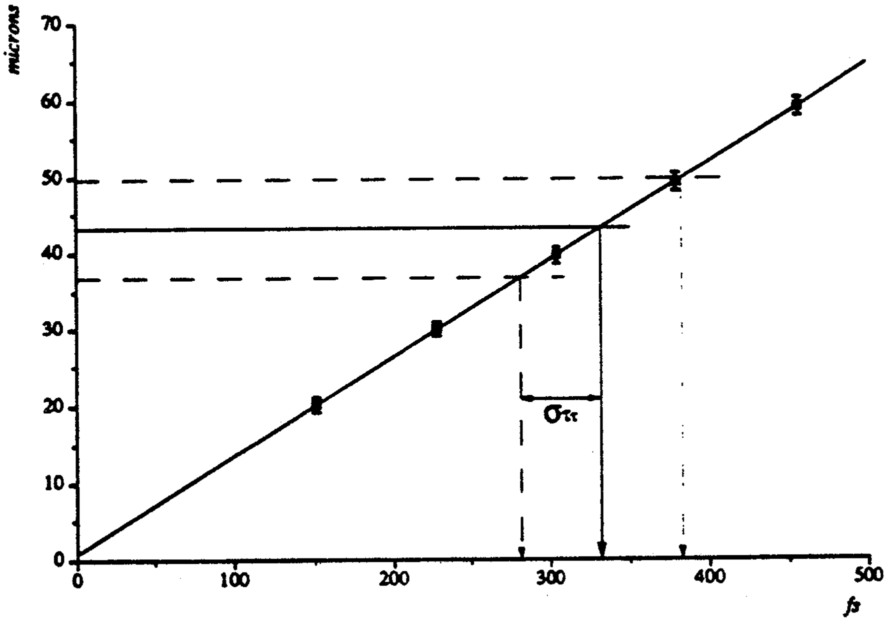

Fig 6.24; **Calibration of mean measured impact parameter in terms of τ lifetime.** Errors on the gradient of the fit are small, and $\sigma_{T\tau}$ is obtained by projection of statistical errors of impact parameter measurement onto the lifetime axis.

A simple straight line fit to the data of Fig 6.24 gives the empirical relation between mean impact parameter μ_{IP} in μm and τ lifetime T_τ in fs;

$$\mu_{IP} = 0.12724\, T_\tau + 0.98 \tag{6.13}$$

However, it is important to note that such a fit assumes statistical independence between the data points involved. In the plot, the approximate error bars shown in μ_{IP} are calculated as RMS/$\sqrt{n}$ (where n is the number of tracks in the simulated data sample), on the basis that when a measured quantity is small compared to detector resolution, Gaussian statistics approximately determine how well the mean of the distribution is known. However, because the five data points represent the same events, with only assumed τ lifetime varying from point to point, the random errors of measurement introduced by the statistics of the data sample are the same in every case, and the fit passes exactly through the data points as shown. The statistical errors are not drastically overestimated, but rather, are highly correlated.

It follows from the basic premise on which the average impact parameter method is based that a τ lifetime of 0fs should result in a mean measured impact parameter statistically coincident with 0μm. A direct consequence of the statistical correlation of the measurements made on the simulated data at various τ lifetimes, is that the straight line fit of equation (6.13) does not pass exactly through the origin, but only within some statistical tolerance of it. The constant term of equation (6.13) (0.98μm) is comparable in magnitude to the approximate error bars on the data points of Fig 6.24 (1.0±0.1μm, see [6]), and is due solely to the finite size of the simulated data sample used in the calibration. Therefore, a modified empirical relation is used here to extract the true τ lifetime value from the real data, where the straight line fit is translated by a shift of -0.98μm in μ_{IP} to compensate for the statistical error of the simulated data measurements;

---

[6] The approximate errors on impact parameter vary from point to point because the higher the τ lifetime, the less Gaussian the impact parameter distribution becomes, and the greater the RMS of the data about the mean. The variation is small, and for the purposes of this argument can be ignored.

$$\mu_{IP} = 0.12724\, T_\tau \tag{6.14}$$

Random errors on the gradient parameter are small, arising only from the randomness of the number generators used to generate the decay distances of flight and the angular distributions of the τs in simulation. Errors associated with equation (6.14) are assumed to be negligible when compared to the statistical uncertainty introduced by the size of the real data sample.

From equation (6.14) the τ lifetime as measured by the average value technique from the 724 chosen real data tracks is given;

$$\begin{aligned} T_\tau &= \frac{1}{0.12724} \times \frac{40.2}{0.93}\ \text{fs} \\ T_\tau &= 340\text{fs} \end{aligned} \tag{6.15}$$

where division by 0.93 allows for a 7% contamination in the data sample by tracks from non-τ events[42]⊛. Were the impact parameter distribution Gaussian, the statistical error on this measurement σ_{T_τ} would be given by its RMS value;

THIS IS BECAUSE OF THE FACT THAT THE PROJECTED ACCOLINEARITY CUT OF SECTION 6.6.2 ELIMINATES BACKGROUND WITH EFFECTIVE LIFETIME ≠ 0.

$$\begin{aligned} &\frac{175\mu\text{m}}{\sqrt{724}} \approx 6.5\mu\text{m} \\ &\text{so that} \quad \sigma_{T_\tau} \approx 7.859 \times \frac{6.5}{0.93}\ \text{fs} \\ &\qquad = 55\ \text{fs} \end{aligned} \tag{6.16}$$

In order to obtain a better estimate of the true errors here, 100 independent simulated data sets of 724 tracks were generated in the barrel region of DELPHI using KORALZ, and were run through KWIKSIM assuming a τ lifetime of 304 fs. Each data set yielded a 'measured' τ lifetime : these are histogrammed in Fig 6.25, where a Gaussian fit to the resultant distribution is also shown. The standard deviation of the fit, 70fs, gives the statistical error associated with this technique for the τ lifetime. The combined mean value of the 100 'measured' τ lifetime results, (303±7)fs, is in good agreement with the input lifetime value, and confirms self-consistency in the method.

The average value method for treating lifetime signed impact parameter data is largely insensitive to systematic error. It is, however, not especially precise : a sample of 724 tracks yields a final figure

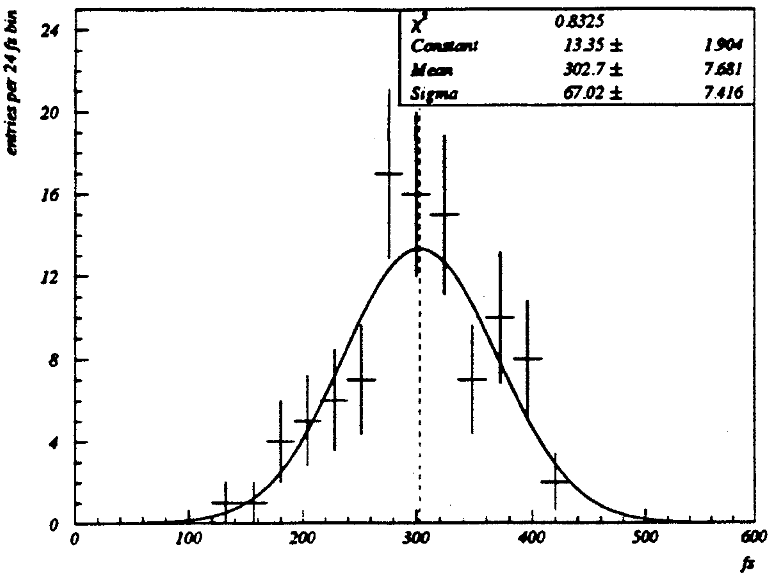

Fig 6.25; Statistical error of the average value technique. Each entry represents a simulated measurement on 724 tracks from τ decay.

good to only ≈20%. In the following section, a method will be outlined which deals rather more efficiently with the information in the lifetime signed impact parameter distribution, and accordingly gives a more precise result.

6.8 τ lifetime by maximum likelihood technique

Section 6.7 introduced a first method for extracting the τ lifetime from a lifetime signed impact parameter distribution. In this section an alternative is described, where the technique of maximum likelihood is used to fit the overall shape of the distribution. No simulation is required to calibrate this lifetime measurement.

In general, a maximum likelihood method involves the inspection of some representative probability that the measured data arise when the variables in the mathematical model under study hold particular values. The values are varied iteratively until the combination giving the highest probability is found. This combination by definition gives the best correspondence between the theoretical model and the measured data sample.

Here, the τ lifetime alone is varied in the context of the standard model to maximise the agreement between model and data. Assuming the data to be well understood, the maximum likelihood method is inherently more precise than the average value method. In effectively varying the average value and the variance of predicted impact parameters at the same time, it places greater emphasis on the values of individual real data rather than relying solely on their central value. Improbable outliers in distributions become of considerable significance : for this reason, the vertex hit to track association of section 6.5 and the data quality cuts of section 6.6 were harsh, at the apparent expense of some statistical information.

The values of the parameters at the most likely match between the model and the data give the central 'measured' numbers for the data. Statistical error bars are found by looking at the behaviour of the probability function around its maximum with respect to the parameters in the model. The natural log of the probability drops by 0.5 at the desired 67% statistical confidence level. It is therefore usual to deal only with log-likelihoods, the maximum of a log-function being identical with that of the function itself.

The following sections contain the detail on how probabilistic information has been used track by track to extract the τ lifetime from the real data.

6.8.1 Calculation of likelihood function

It is required to evaluate the probability that a data sample of 724 impact parameters is taken from an underlying model distribution due to a tau lepton of a certain known mean lifetime. The model distribution is itself the required probability distribution. Track by track, the probability P_i of a measured impact parameter coming from the distribution may simply be read from the plot as shown in Fig 6.26. The distances of flight travelled by individual τs are uncorrelated, and, it

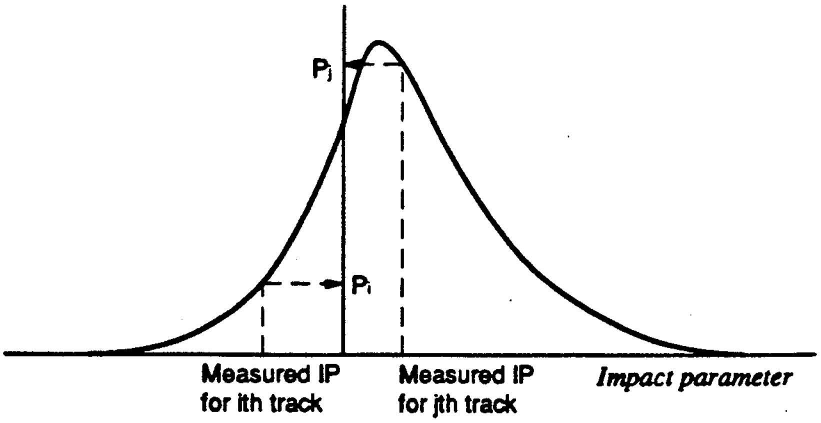

Fig 6.26. The probability of measuring a given impact parameter is read off an impact parameter distribution.

follows, so are the impact parameters due to those distances of flight : the probability P that many impact parameters are drawn from the distribution is then simply;

$$P = \prod_{\text{tracks } i} P_i \tag{6.17}$$

Where calculation of statistical errors is concerned, it will be more convenient to deal with log-likelihoods;

$$\ln (P) = \sum_{\text{tracks } i} \ln (P_i) \tag{6.18}$$

The model probability distribution was generated for this analysis as follows. A large number of τ events generated using the KORALZ program were run through the official DELPHI simulation package, and were flagged if they passed the τ selection cuts of Chapter 5. The KORALZ output for the flagged events was then input into the KWIKSIM microvertex simulation program, and a lifetime signed impact parameter distribution was generated. No detector resolution effects were simulated. The only way that negative impact parameters could arise in this distribution was if the thrust axis of the event badly reconstructed the direction of the simulated τ. Fig 6.3b showed the distribution of impact parameter data typically expected at this stage.

In order to allow for detector resolution effects, the impact parameter distribution obtained from the KWIKSIM program was convoluted numerically with a parametrised resolution function obtained from real data. Impact parameter resolution for high momentum particles can be estimated by examining plots of geometric impact parameter for tracks from the dimuon decay of the Z^0. No shortlived primary particle has offset their production point from that of the Z^0 decay, so that only vertex detector resolution and beamsize contribute in the impact parameter distributions. For lower momentum particles, multiple scattering resolution effects must be considered. It was shown in Fig 6.22 that for tracks of transverse momentum greater than 5 GeV/c, multiple scattering effects were negligible. The transverse momentum cut of 5 GeV/c discussed in section 6.6 therefore takes account of this phenomenon.

why not the lifetime signed?

2000 tracks from dimuon Z^0 decay were used in a parametrisation of geometric impact parameter data with a (maximum likelihood) fit to two Gaussians and a flat line background (Fig 6.27). The parameters in the fit were;

- the width of the first Gaussian
- the width of the second Gaussian
- the relative normalisation of the area under the first Gaussian to the area under the second
- the relative normalisation of the area under the flat line background to the area under the double Gaussian shape

and their optimised values are shown in Fig 6.28. A dominant double Gaussian form was chosen because of the nature of the expected contributions to the distribution. Vertex detector resolution is known to be closely Gaussian (equation (6.6), Fig 6.7) and similarly the beam profile can be approximated as a Gaussian in x and in y. The optimised resolution function widths of 95μm and 188μm are in excellent agreement with the convolution of a tracking error contribution σ_T of 80μm

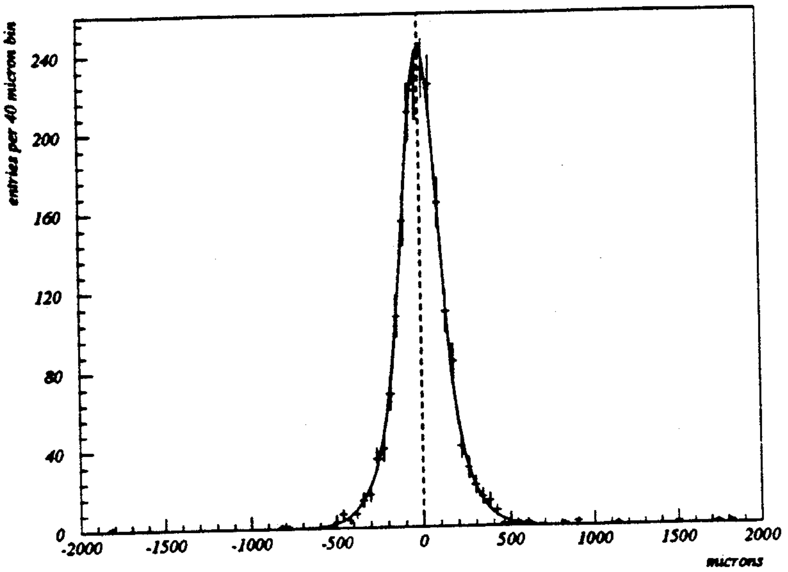

Fig 6.27; The parametrised resolution function.

Parameter	Optimised value	Covariance matrix			
σ_N	95μm	53.5			
σ_B	188μm	20.7	20.5		
R	2.5	3.61	1.80	0.301	
F	0.008	-15.9E-4	-3.68E-4	-0.783E-4	0.0321E-4

Parameter definitions :

σ_N	width of narrow Gaussian
σ_B	width of broad Gaussian
R	ratio of area under narrower Gaussian to area under broader Gaussian
F	ratio of area under flat line background to total area under 2 Gaussians

Fig 6.28; Resolution function parameters.

(section 6.3.1) with beam breadths in x and y of $\sigma_X \approx 180\mu m$ and $\sigma_Y \approx 15\mu m$ (section 6.3.2). A flat line was included to stabilise the fit with respect to outliers, and represented event sample contamination and any remaining tracks with misassociated vertex detector hits. It is noted in passing that if the mean values of the two Gaussian components of the fitted function are also allowed to vary in a six parameter fit, the optimised values for the new parameters are consistent with zero.

To the convoluted probability distribution must be added a component to allow for tracks in the data sample which are not from τ decay, but from contaminating events. The percentage of such events in the sample is estimated to be 7% (section 5.5), and is estimated to comprise wholly other Z^0 dilepton decay events and two photon events. After the projected acollinearity cut of section 6.6, there can be no lifetime information carried by tracks from such events. Their impact parameter probability distribution is therefore estimated as a suitably normalised resolution function, and included in the convoluted probability distribution as generated above.

Fig 6.29 shows the final model distribution of impact parameters generated as above, for a τ lifetime equal to the current world average of (303±8)fs. Linear extrapolations between bin centres are shown graphically, and used in the calculation of impact parameter probabilities. Formally, the distribution can be described in terms of the ideal function $F(d_0)$ from KWIKSIM and the resolution function $R(d_0)$;

$$P(d_0) = (1-\lambda)[F(d_0) \otimes R(d_0)] + \lambda R(d_0) \qquad (6.19)$$

where $P(d_0)$ is the resulting probability distribution and λ=0.07 is the fraction of contaminating events in the sample.

The probability distribution of Fig 6.29 would be used in the calculation of the likelihood that the data are represented by the standard model when the world average lifetime value is assumed. The adoption of this distribution in the instance that other τ lifetimes be required, and the iterative procedure used to maximise the summed log-likelihoods that individual measured impact parameters come from a distribution of this form, are now discussed in section 6.8.2.

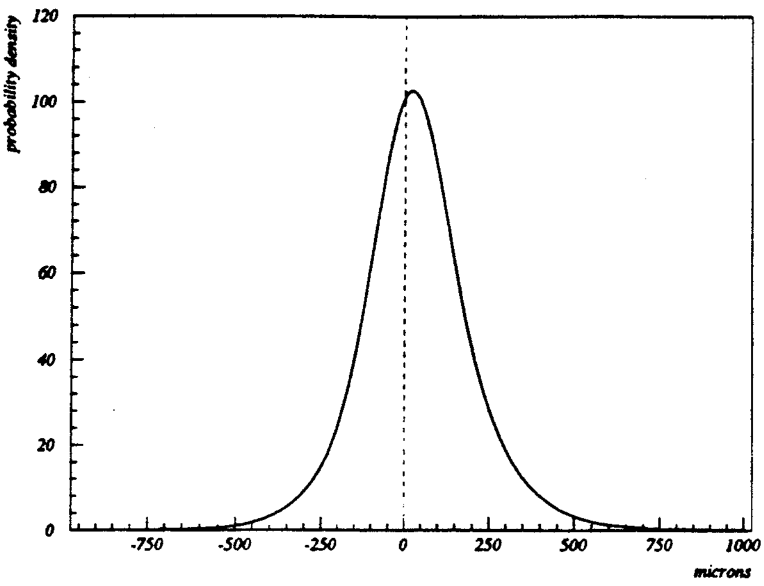

Fig 6.29; Generated probability distribution for impact parameter.

6.8.2 The maximum likelihood fit

MINUIT[43] is a package for the minimisation of a function (variable) with respect to a parameter or list of parameters. Starting from some user defined parameter estimates, MINUIT determines the parameter values at the function turning point, or at specified confidence levels away from the turning point. In this analysis, MINUIT has been used to minimise the negative of the probability (maximise the likelihood) that data and model agree, with respect to the τ lifetime.

In each iteration of the MINUIT program, the function value, here the representative probability for a data-model match, is calculated by a call to a user subroutine. In the subroutine, the global probability is calculated from the appropriate probability distribution in the manner described above (section 6.8.1). Clearly, to regenerate the probability distribution from KORALZ information for each model τ lifetime required by MINUIT would be very time consuming and inconvenient. To overcome the problem, use is made of the fact that impact parameter is directly proportional to τ lifetime, in the ideal case when detector resolution is perfect. For each required MINUIT lifetime T_M, the data of Fig 6.3b, generated with a lifetime T_0, are scaled by a factor of T_M/T_0, and rebinned. The rebinned distribution is convoluted with the parametrised resolution function to form the new probability distribution.

The maximum likelihood fitting procedure outlined above has been used on the sample of 724 impact parameters selected from the 1990 1-prong τ decay data from DELPHI. The data are shown in Fig 6.30 together with the normalised probability distribution as optimised by the maximum likelihood fit. The value of the τ lifetime used in the generation of the optimised probability distribution was

$$T_\tau = 321\text{fs} \tag{6.20}$$

Fig 6.31 shows the variation of the likelihood function with the model τ lifetime used. Probability distributions such that the summed log-likelihoods of a model-data match were 0.5 lower than in the optimised case correspond to τ lifetime values of 357fs and 285fs. The likelihood function is therefore symmetric about the most probable τ lifetime value, and the statistical error bar on the measurement is

$$\sigma_{T_\tau} = 36\text{fs} \tag{6.21}$$

The contribution to the probability distribution due to the estimated event contamination is also shown in Fig 6.30.

6.8.3 Consistency of method in simulation

In order to check the maximum likelihood method for τ lifetime for self-consistency, the lifetime analysis has been performed on a number of simulated KWIKSIM data samples, generated using different τ lifetime values. No inconsistencies were found, and measured lifetime values agreed

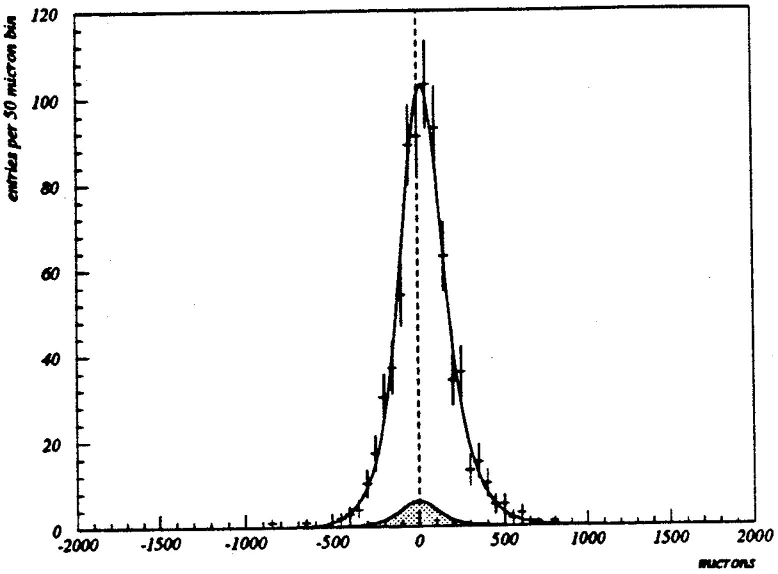

Fig 6.30; **Lifetime signed impact parameter data for tracks from 1 prong τ decay together with the most probable generated model distribution.** Also shown (hatched) is the expected contribution to the sample from tracks from non-τ events.

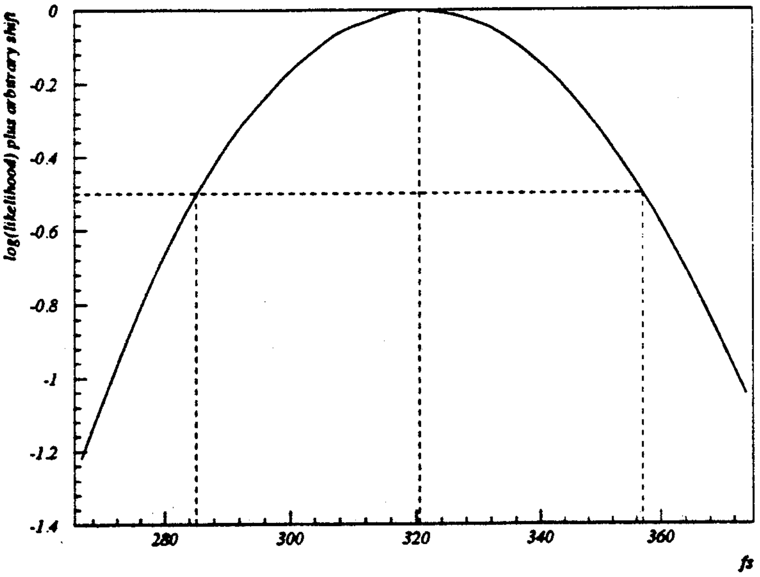

Fig 6.31; **Maximisation of the likelihood function.** Showing the variation of the summed log-likelihood that data and model agree with the model τ lifetime assumed. The statistical 67% confidence level around the most likely τ lifetime is given when the log-likelihood function drops by 0.5.

with input values within expected statistical errors. Detail of one of the consistency checks is now included below.

As described in section 6.7, 100 statistically independent samples of 724 tracks from 1-prong τ decay were generated in the DELPHI barrel region using a model τ lifetime of 304fs. The tracks were run through the KWIKSIM microvertex detector simulation program, and a lifetime signed impact parameter distribution was made for each of the 100 data samples. The probability distribution of Fig 6.3b was convoluted with a parametrised resolution function from 2000 KWIKSIM muon tracks from the DYMU3 generator, and 100 maximum likelihood fits were performed on the simulated τ data. Fig 6.32 shows the distribution of measured τ lifetimes from the 100 simulated measurements. A Gaussian fit to the data is also shown. The width of the fit, 32fs, is in good agreement with the observed experimental statistical error of 36fs (section 6.8.2). The error on the central value of the fit is clearly $36\text{fs}/\sqrt{100}$, and so combining the 100 mock experiments gives a 'measured' τ lifetime of (305±4)fs. Input and output τ lifetimes agree well.

6.8.4 Evaluation of systematics

The number of causes of potential systematic error associated with the maximum likelihood method for the τ lifetime is low. Individual contributions are however significant. Fig 6.33 summarises the various systematic errors associated with the current measurement. Detail of their assessment is given below.

In general, systematic error is introduced where a numerical assumption is made during the course of a method. On any assumed number N there will be some error ΔN, and the change in the final measured value observed on varying N by ΔN is the systematic error associated with that numerical assumption. It is implicit however in this simple approach that the quantity enumerated by N is statistically independent from other quantities which may cause systematic error. If two quantities are visibly correlated, then more care must be taken.

Systematic error arises firstly and foremostly in this analysis from the parametrisation of the resolution function used to convolute with the probability distribution of Fig 6.3b. Dimuon statistics

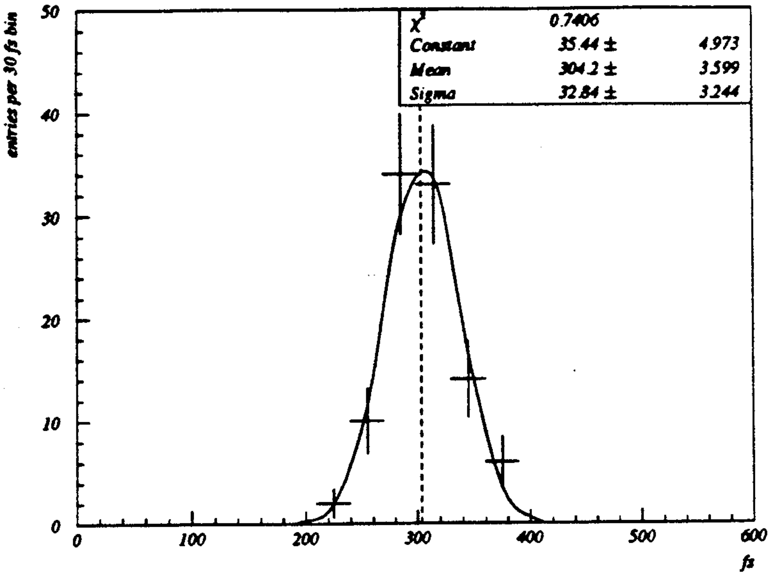

Fig 6.32; **Statistical error of the maximum likelihood technique.** Each entry represents a simulated measurement on 724 tracks from τ decay.

Cause	**Error in fs**
Resolution function parametrisation	±14
Range of data in fit	±9
Level of sample contamination	±7
Energy of LEP beam	negligable
Total systematic error	±18

Fig 6.33; Sources of systematic error.

limit the precision with which the parameters can be determined, and in doing so dominate the systematic precision of the τ lifetime measurement. The covariance matrix for the optimised resolution function parameters is shown in Fig 6.28. Clearly the amount of flat line background included in the fit to the dimuon data is not critical, while the widths of the two Gaussians and their relative normalisation are rather more so. Furthermore, the values taken by these last three parameters are highly correlated to one another.

The method employed here for dealing with correlated errors is taken from ref[44] . The value of the τ lifetime obtained from the maximum likelihood procedure can be expressed for the present purpose as a function of the parameters $\underline{p}=\{p_1, p_2, p_3, p_4\}\equiv\{\sigma_N, \sigma_B, R, F\}$ used in the resolution function fit;

$$T_\tau(\underline{p}) = T_\tau(\underline{\mu}) + \sum_{k=1}^{4}(p_k - \mu_k)\left(\frac{\partial T_\tau}{\partial p_k}\right)_{\underline{p}=\underline{\mu}} \tag{6.22}$$

where the vectorial quantity $\underline{\mu}$ represents the optimised values of the parameters $\underline{p}$ about which a Taylor expansion has been taken. By definition, the variance of $T_\tau(\underline{p})$ is given by;

$$\begin{aligned} V[T_\tau(\underline{p})] &= E[(T_\tau(\underline{p}) - T_\tau(\underline{\mu}))^2] \\ &= E\left[\left(\sum_{k=1}^{4}(p_k - \mu_k)\left(\frac{\partial T_\tau}{\partial p_k}\right)_{\underline{p}=\underline{\mu}}\right)^2\right] \end{aligned} \tag{6.23}$$

where $E[x]$ denotes the expectation value of x and the second line follows from equation (6.22). The variance of T_τ is just $\sigma^2_{T_\tau}$, so that evaluating 6.23;

$$\begin{aligned} \sigma^2_{T_\tau} = V[T_\tau(\underline{p})] &= \sum_{i=1}^{4}\sum_{j=1}^{4}\left(\frac{\partial T_\tau}{\partial p_i}\right)_{\underline{p}=\underline{\mu}}\left(\frac{\partial T_\tau}{\partial p_j}\right)_{\underline{p}=\underline{\mu}} E[(p_i - \mu_i)(p_j - \mu_j)] \\ &= \sum_{i=1}^{4}\sum_{j=1}^{4}\left(\frac{\partial T_\tau}{\partial p_i}\right)_{\underline{p}=\underline{\mu}}\left(\frac{\partial T_\tau}{\partial p_j}\right)_{\underline{p}=\underline{\mu}} V_{ij}[\underline{p}] \end{aligned} \tag{6.24}$$

where $V_{ij}[\underline{p}]$ is the covariance matrix for the parameters $\underline{p}$, output by the fitting program. Numerical estimation of the partial derivatives in equation (6.24) then permits calculation of the systematic error on the τ lifetime resulting from uncertainty in the resolution function parameters.

The systematic effect on the τ lifetime of varying the resolution function parameters in such a way as to reach the 67% confidence level of parametrisation is found to be ±14fs. That the resolution function fit to the dimuon geometric impact parameter data is good infers that any further systematic effects on τ lifetime associated with the fit are small compared to the 14fs resulting from limited dimuon track sample size.

A second source of possible systematic error lies in the estimation of the amount of event contamination on the τ sample. This source of error is not visibly correlated with any other, and as such may be regarded as being statistically independent. Varying the amount of contamination assumed by one standard deviation changes the value of the τ lifetime measured by ±7fs.

It was considered important to investigate the systematic effects of fitting different ranges of the impact parameter distribution. Fig 6.34 shows the value of τ lifetime extracted from a maximum likelihood fit against the range of data taken in the fit. Also shown are the numbers of tracks included in the various fits. Clearly, statistical errors on the measured values in the plot are highly correlated, and any visible discrepancies between the measured values are of systematic significance. As an estimate of remaining features not well understood in the data, the RMS spread of ±9fs ~~seconds~~ of the values shown in the plot about their mean is included as a systematic error of the method. The mean of the measured values corresponds exactly to the value of the fit over the whole range of data quoted in section 6.8.2, 321fs.

As a check for remaining systematic errors, τ lifetime measurements were made on subsamples of the data corresponding to physically independent parts of the detector and to tracks of positive and negative charge. The measured values are presented in Fig 6.35, and show no evidence of systematic bias.

It should be noted that the beam energy at which LEP was running for the fill in which a particular τ event was recorded does not significantly influence the measured τ lifetime. Fig 6.36 shows the

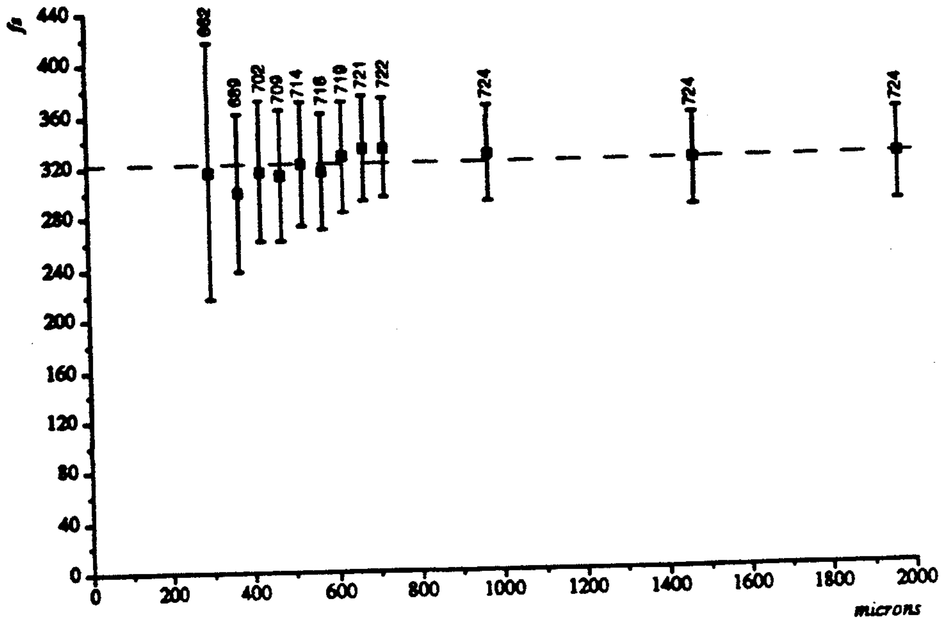

Fig 6.34; Measured τ lifetime against range of impact parameter data included in the fit.

Range of data	Measured lifetime in fs, with statistical error
(All data	321±36)
Negatively charged tracks	343±50
Positively charged tracks	294±50
θ < 90°	292±50
θ > 90°	361±50
ϕ < 90° or ϕ > 270° (mechanically a VD half-shell)	321±50
90° < ϕ < 270° (other VD half-shell)	317±50

Fig 6.35; Measured τ lifetimes for various subsamples of the data set.

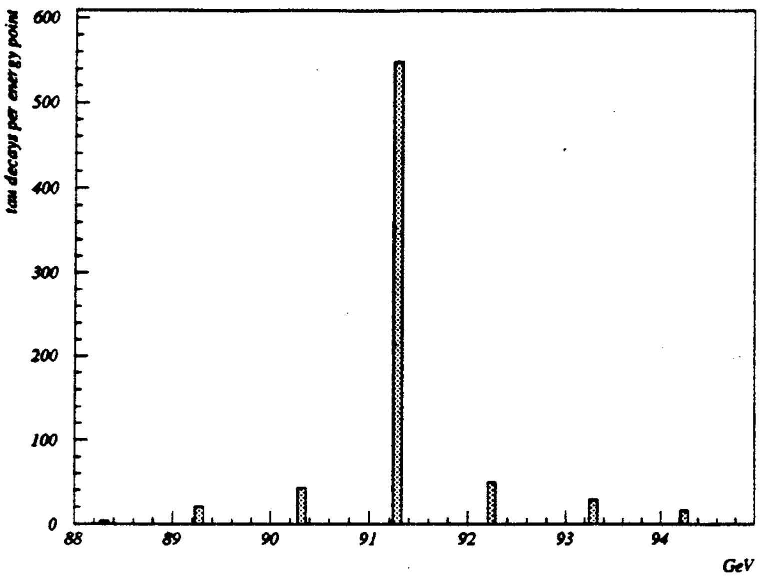

Fig 6.36; Variation of the LEP beam energy for the lifetime measurement data sample.

distribution of beam energies for the 724 tracks used in the lifetime analysis. The Lorentz γ factors corresponding to the most and least energetic fills differ by only ≈3%. If a weighted mean γ is calculated for the distribution as shown, the obtained value is within 1% of the value assumed in the KORALZ program for the generation of the ideal impact parameter probability distribution (section 6.8.1). The KORALZ program takes into account the effects of radiative corrections to centre of mass energy.

Added in quadrature, the individual contributions to systematic error detailed here combine to give 18fs. This compares favourably with the estimated statistical error on the measurement, 36fs.

6.9 Summary

Two methods for the τ lifetime from lifetime signed impact parameter data have been described in this Chapter. An average impact parameter method gives a measured lifetime of 340±55fs. Maximum likelihood techniques give a lifetime of 321±40fs (where statistical and systematic errors
(±36fs) (±18fs)
have been added in quadrature).

Clearly the two measurements are highly correlated. The result from the maximum likelihood fit is the more precise of the two, and so is taken as the final result of this analysis.

Chapter 7. Conclusions

In this thesis, a new measurement of the τ lifetime T_τ has been described. The value obtained;

$$T_\tau = \underset{\pm 36\text{fs (STAT)} \quad \pm 18\text{fs (SYS)}}{321 \pm 40\text{fs}} \tag{7.1}$$

is consistent with previously measured values (Fig 7.1).

Equation (1.15) gave an expression for the ratio g_τ/g_μ in terms of the measurable quantities M_μ, M_τ, T_μ, T_τ and B_e. World average values for these quantities, taken from ref [7], are shown in Fig 7.2. Taking T_τ from equation (7.1) and applying equation (1.15), the ratio is calculated to be;

$$\frac{g_\tau}{g_\mu} = 0.94 \pm 0.06 \tag{7.2}$$

where the contributions to the error are shown in Fig (7.3).

Clearly the result is consistent with lepton universality : equally, however, it is consistent with values of g_τ/g_μ other than unity. A more precise value for the ratio can be obtained by combining the new τ lifetime measurement with the previous world average value, to give;

$$T'_\tau = 304 \pm 8\text{fs} \tag{7.3}$$

The new ratio is;

$$\frac{g_\tau}{g_\mu} = 0.965 \pm 0.017 \tag{7.2}$$

where the error contribution from T'_τ has now been reduced to 0.013. [redacted] THE VALUE IS TWO STANDARD DEVIATIONS FROM UNITY, AND AS SUCH THIS RESULT [redacted] CAN NOT RULE OUT LEPTON UNIVERSALITY.

Year	Experiment	Value for τ lifetime (fs)
1987	ARGUS	295 ± 18
1987	CLEO	325 ± 33
1987	HRS	302 ± 17
1987	MAC	309 ± 19
1988	MARK II	288 ± 23
1988	TASSO	306 ± 24
1989	JADE	301 ± 29
1991	DELPHI (b)	310 ± 33

Fig 7.1; Previous measurements of the τ lifetime, INCLUDING THE MEASUREMENT OF THREE PRONG $\tau^+\tau^-$-EVENT DATA TAKEN AT DELPHI (DELPHI(b) - SEE [1]).

Quantity	World average value
M_μ	105.658387 ± 0.000034 MeV/c²
T_μ	2.19703 ± 0.00004 μs
M_τ	1784.1 + 2.7 - 3.6 MeV/c²
T_τ	303 ± 8 fs (DATA OF FIG 7.1; NOT INCLUDING DELPHI (b))
B_e	0.177 ± 0.004

Fig 7.2; World average values for various quantities.

With $f(x) = g_\tau / g_\mu$;

Quantity	Value of $(\partial f/\partial q_i)^2 dq_i^2$ for quantities q_i	Contribution to error
M_μ	0.206×10^{-12}	0.45×10^{6}
T_μ	0.731×10^{-10}	0.86×10^{5}
M_τ	0.126×10^{4}	0.0036
T_τ	0.345×10^{2}	0.059
B_e	0.113×10^{3}	0.011
Total error	0.0036	0.06

Fig 7.3; Contributions to the error on g_τ/g_μ.

The future for the τ lifetime measurement at DELPHI looks promising. Early in 1991, a third silicon layer was installed inside the existing two of the microvertex detector, at a radius of only 6cm from the beamline. Three layers of silicon give potentially an impact parameter precision of $\approx$20μm. In addition, capacitative beam orbit monitors will shortly be instrumented to give definitive beam positions in y good to $\approx$10μm. The final 1991 τ lifetime measurement data sample should be at least twice the size of the sample used in this analysis, and the error on T_τ from DELPHI should be considerably less in the future than the current 12%.

Nevertheless, a precise value for g_τ/g_μ may not yet be obtained for some time to come. Contributions to the error on the ratio shown in equation (7.4) from T_τ and B_e are comparable, and an improvement by a factor of two in the precision of the world average value for T_τ would reduce the error on g_τ/g_μ by only 25%. It will require more than just precise T_τ measurements before this method ultimately can resolve the question of lepton universality.

High Energy Physics Research

A priest asked : What is Fate, Master ?

And He answered :

It is that which gives a beast of burden its reason for existence.

It is that which men in former times had to bear upon their backs.

It is that which has caused nations to build byways from City to City upon which carts and coaches pass, and alongside which inns have come to be built to stave off Hunger, Thirst and Weariness.

And is that Fate ? asked again the priest.

Fate...? Sorry, I thought you said Freight, responded the Master.

That's all right, said the priest. I wanted to know what Freight was too.

"The Profit", Kehlog Albran

References

[1] DELPHI Collaboration, *Submitted to Phys Lett, CERN preprint* **CERN-PPE/91-115** (1991)

[2] SL Glashow, *Nucl Phys* **B22** (1961) 579

[3] S Weinberg, *Phys Rev Lett* **19** (1967) 1264

[4] A Salam, in: *Proc of the 18th Nobel Symp*, ed. N Svartholm (Almqvist and Wiskell,Stockholm,1968) 367

[5] F Halzen and AD Martin, *Quarks and Leptons* (Wiley,New York,1984)

[6] G Altarelli et al., *Z Physics at LEP1 (volume 1)* (CERN yellow report 89-08,1989)

[7] Particle Data Group, *Phys Lett* **B239** (1990) 1

[8] CERN Publications, *Large Electron Positron storage ring* (technical notebook,1989)

[9] DELPHI Collaboration, *Nucl Instr and Meth* **A303** (1991) 233

[10] DELPHI Collaboration, *CERN preprint* **CERN-LEPC/83-3** (1983)

[11] SC Gawne, *Study of the dimuon decay mode of the Z boson at LEP* (PhD Thesis,University of Liverpool,1990)

[12] A Amery et al., *Nucl Instr and Meth* **A283** (1989) 502

[13] HG Fischer et al., *IEEE Trans Nucl Sci* **NS-27** (1980) 38

[14] B Nijjhar and DW Reid, *DELPHI note* **DELPHI 91-21 PHYS 92** (1991)

[15] HR Band et al., *Phys Rev Lett* **59/4** (1987) 415

[16] C Bebek et al., *Phys Rev D* **36/3** (1987) 690

[17] JA Jaros et al., *Phys Rev Lett* **51/11** (1983) 955

[18] C Damerell, *Nucl Instr and Meth* **226** (1984) 26

[19] WRT ten Kate, *The Silicon Microstrip Detector* (Delft,1988)

[20] G Batignani et al., *Nucl Instr and Meth* **A227** (1989) 147

[21] G Jaffe, *Phys Z* **33** (1932) 393

[22] PJ van Heerden, *The Crystal Counter* (North-Holland,Amsterdam,1945)

[23] KG McKay, *Phys Rev* **84** (1951) 829

[24] JBA England et al., *Nucl Instr and Meth* **185** (1981) 43

[25] E Belau et al., *Nucl Instr and Meth* **214** (1983) 253

[26] JBA England et al., *Nucl Instr and Meth* **196** (1982) 149

[27] A Peisert, CERN (Private Communication)

[28] G Anzivino et al., *Nucl Instr and Meth* **A263** (1988) 215

[29] P Weilhammer, *CERN preprint* **CERN-EP/86-54** (1986) 1

[30] R Alberganti et al., *Nucl Instr and Meth* **A248** (1986) 337

[31] M Caccia et al., *Nucl Instr and Meth* **A260** (1987) 124

[32] J Kemmer, *Nucl Instr and Meth* **226** (1984) 89

[33] JT Walker et al., *Nucl Instr and Meth* **226** (1984) 200

[34] AR Campion, *The DELPHI Silicon Microvertex Detector* in: *Proc of the 1991 Lake Louise Winter Institute*, ed. University of Alberta (Canada) in publication

[35] M Tyndel, CERN/RAL (Private Communication)

[36] ML McCubbin, Univeristy of Liverpool (Private Communication)

[37] S Jadach et al., *CERN writeup* (draft version 1989)

[38] JE Campagne and R Zitoun, *CERN writeup* in preparation

[39] VL Highland, *Nucl Instr and Meth* **129** (1975) 497

[40] VL Highland, *Nucl Instr and Meth* **161** (1979) 171

[41] D Liko, CERN (Private Communication)

[42] S Behrends, *Measurement of the Tau Lifetime at root s = 10.5GeV* (PhD Thesis,University of Rochester, USA,1987)

[43] F James and M Roos, *CERN writeup* **DD-D506** (1989)

[44] WT Eadie et al., *Statistical Methods in Experimental Physics* (1971)

[45] NORTHERN SEMICONDUCTOR REFERENCE DATABOOK 3 (1988)

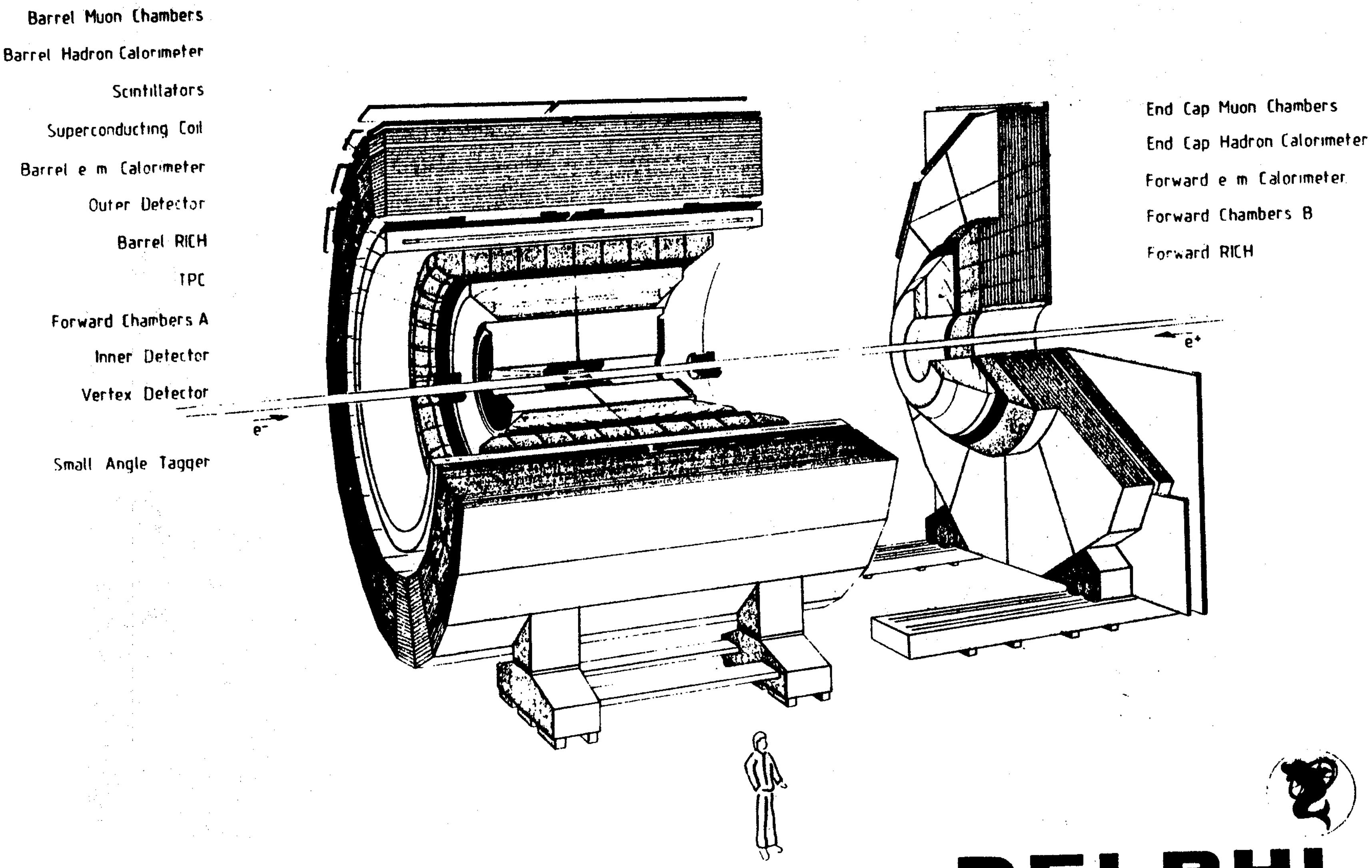
Barrel Muon Chambers
Barrel Hadron Calorimeter
Scintillators
Superconducting Coil
Barrel e m Calorimeter
Outer Detector
Barrel RICH
TPC
Forward Chambers A
Inner Detector
Vertex Detector
Small Angle Tagger
e⁻
e⁺
End Cap Muon Chambers
End Cap Hadron Calorimeter
Forward e m Calorimeter
Forward Chambers B
Forward RICH

DELPHI

Aerial view of CERN, with Geneva and the Alps behind